EVALUATING THUNDERSTORM OUTFLOW BOUNDARIES IN COMPLEX TERRAIN

by

NICHOLAS THOMAS LUCHETTI

B.S., Virginia Polytechnic Institute and State University, 2014

M.S., East Carolina University, 2016

A thesis submitted to the

Faculty of the Graduate School of the

University of Colorado in partial fulfillment

of the requirement for the degree of

Doctor of Philosophy

Department of Atmospheric and Oceanic Sciences

2021

Committee Members:

Dr. Katja Friedrich

Dr. Julie Lundquist

Dr. Branko Kosovic

Dr. Jenifer Balch

Dr. Rochelle Worsnop

Luchetti, Nicholas Thomas (Ph.D., Department of Atmospheric and Oceanic Sciences)
Evaluating Thunderstorm Outflow Boundaries in Complex Terrain
Thesis directed by Associate Professor Katja Friedrich

Abstract

Rapid changes in wind and turbulence generated by thunderstorm gust fronts (GFs) can threaten the safety of wildland firefighters. Firefighters are particularly vulnerable to GFs in areas of complex terrain, where local terrain influence on GF winds can add complexity and tactical challenges faced by emergency management teams. Despite this, our traditional understanding of GF structure and behavior has focused primarily on GFs that develop from organized thunderstorms in flatter regions. In this dissertation, the investigation of GFs is broadened to those that occur in areas of complex terrain. First, Chapter 2 focuses on quantifying changes in vertical profiles of atmospheric variables during 24 GFs that occurred in the Colorado Front Range using in-situ and remote-sensing instruments. Second, in Chapter 3, GFs that were pushed uphill atop the crest of the Mogollon Rim in Arizona are statistically compared to those that propagated down into or along the Rio Grande Valley in New Mexico using *in situ* and radar observations. Lastly, in Chapter 4, idealized microburst and outflow boundaries are simulated using the Weather Research and Forecasting (WRF) model to quantify canyon-enhancement of winds and turbulence generated by microbursts.

In Chapter 2, it was found that the magnitude change in GF characteristics were on average weaker in the Colorado Front Range GFs compared to what is typically observed along GFs from organized, severe storms in flatter regions. Most events from this study experienced an increase in wind speed from 1 to 8 m s^{-1}, relative humidity from 1 to 8 %, and weak vertical motion from 0.3 to 3.6 m s^{-1} during GF passage, while temperature dropped by 0.2 to 3° C and

turbulent kinetic energy (*TKE)* peaked at > 4 m^2 s^{-2}. Vertical profiles reveal that these changes vary little with height in the lowest 300 m.

In Chapter 3, GFs that propagated down into and along the Rio Grande Valley in NM were associated with faster propagation speeds ($\overline{pspd}$ = 8.6 m s^{-1}), slightly larger decreases in temperature ($\Delta\bar{T}$ = -2.2°C), larger increases in horizontal wind speeds ($\Delta\overline{wsp}$ = 7.5 m s^{-1}) and changes in wind direction ($\Delta\overline{wdir}$ = 76.5°) compared to GFs that reached the crest of the Mogollon Rim in Arizona ($\overline{pspd}$ = 5.2 m s^{-1}; $\Delta\bar{T}$ = -1.5°C; $\Delta\overline{wsp}$ = 3.5 m s^{-1}; $\Delta\overline{wdir}$ = 53.1°). GFs atop the Mogollon Rim in Arizona behaved less in accordance with density current theory compared to those in the Rio Grande Valley in New Mexico.

In Chapter 4, short-distance microbursts produced stronger canyon-induced enhancements in horizontal wind, upward vertical velocity, and *TKE* in the canyons and along the canyon walls compared to long-distance microbursts, which were located ~2 km farther away. For canyons located closer to the microburst, the increase in horizontal winds, vertical velocity, and *TKE* was generally stronger in the canyon and along the walls of the steeper 30° sloped canyons compared to the 10° sloped canyons. Lastly, the maximum increase in horizontal wind is mostly observed near the canyon floors and towards the exit region of the canyons regardless of the proximity to the microburst. Conversely, the maximum increase in upward vertical velocity and *TKE* is mostly observed at higher elevations on the walls and along the canyon crests in both short- and long-distance canyons.

Dedication

This dissertation is dedicated to childhood cancer patients and their parents. As I reflect upon my own experience with childhood cancer, the only sadness stems from thinking about my parents and the pain they must have felt hearing that I had cancer, watching me struggle with chemotherapy, and experiencing the fear of losing me. If only for a little, I want this work to inspire parents who have children struggling through cancer. I'd love to share with them some hope that their child can also grow up and still do big things! Much love, and remember, when all else fails, just take another step.

Acknowledgements

I'd like to first acknowledge and give thanks to my family for all of their love, support, and encouragement throughout all of my academic experiences. To my parents, thank you for providing me with an environment that supported and emphasized the importance of learning and gaining knowledge through academic avenues. Thanks especially to my father, John Luchetti, for teaching me the benefits that come from working hard and pursuing each professional endeavor with the utmost integrity and passion. To my mom, Mary Ellen Luchetti, thank you for always being there for me especially during moments when what I needed most was simply an ear to vent to. To my brothers, Tim and Jeff, thank you for inspiring me to pursue academic excellence at the highest level possible. Your mutual love for science and helping others has helped me tremendously over the past decade. I'm extremely proud of your own accomplishments, and I look forward to many more years of discussing technological advancements and the future of the human species. I'd also like to acknowledge and dedicate this work to the memory of my grandparents Carl and Joan Luchetti, and George and Rita Yanik. Your dedication to family, hard work, and incredible displays of courage and strength through difficult times set the bar high for your descendants. I hope that we've made you proud with our own accomplishments and dedication to the values you've instilled in us. To the many other family members and friends who've had a positive impact on the trajectory of my life, thank you for everything.

I want to thank Dave Carroll and Dr. Drew Ellis at Virginia Tech for first introducing me to the wonderful and challenging field of meteorology. Walking into Dave's office in 2012 and discovering that Virginia Tech had started a meteorology program completely altered my life's trajectory. Thank you for giving that to me. I'd also like to thank Dr. Rosanna Ferreira and Dr.

Tom Rickenbach at East Carolina University for first introducing me to atmospheric research. It was during my time working with you that I developed a passion for pursuing questions to problems I found to be curious. Thank you for your friendship as well.

I'd also like to thank my fellow graduate students in the ATOC department at CU Boulder for helping me succeed. Specifically, I'd like to thank Matt Cann, Bobby Wallace, Chris Rodell, Ren Smith, Brian Rainwater, Connor Nelson, and Ryan Harp for their help and for allowing me to bounce ideas off of them many times over the past few years. Most importantly, thank you for the great friendships we've developed along the way.

I'd like to thank Dr. Katja Friedrich for guiding and advising me over the past few years. I'd especially like to thank her for encouraging me to pursue my own research questions and ideas, and for developing me into a better scientist. But most importantly, thank you for allowing me to pursue my dream job with the National Weather Service, while simultaneously helping me to finish this dissertation remotely. I'd also like to thank Dr. Julie Lundquist, Dr. Branko Kosovic, Dr. Rochelle Worsnop, and Dr. Jennifer Balch for providing ideas and guidance that helped enhance the work presented in this dissertation.

Finally, I'd like to thank and acknowledge the love of my life, my beautiful wife Donnie. Thank you for always showing me love and support especially during moments when I was feeling discouraged. Your kindness and encouragement carried me through this pursuit, and without which, I can confidently say I never would have finished. I am in awe of and inspired by your incredible strength and courage, and all that you have accomplished. I'm excited to see where our journey takes us and as always, I'll love you forever.

Table of Contents

List of Tables

List of Figures

1 Introduction

Rapid changes in wind and turbulence generated by thunderstorm outflow boundaries or gust fronts (GFs) can threaten the safety of wildland firefighters. GFs develop through evaporation, melting, and sublimation of precipitation below thunderstorms producing strong and turbulent ground-level winds that propagate horizontally and cause rapid changes in atmospheric parameters along their leading edge (Fig. 1.1). Wildfires in complex terrain are especially vulnerable as winds from GFs can be channeled and enhanced by local topography, and where the tracking of thunderstorms is often more difficult due to limited and sparse weather observations (Wakimoto et al. 1994; Goens and Andrews 1998; Sharples et al. 2017; Luchetti et al. 2020). Furthermore, local terrain influence on GF winds can add complexity and tactical challenges faced by emergency management teams (Goens and Andrews 1998; Hardy and Comfort 2015; Sharples et al. 2017). During the 2013 Yarnell Hill Fire in Arizona, for example, 19 firefighters were killed because of rapid and severe changes to the fire's behavior, induced by a passing GF (Karels and Dudley 2013; Hardy and Comfort 2015; Paez et al. 2015) (Fig. 1.2). Another deadly example of a GF interaction with a wildfire occurred on June 26, 1990, as hundreds of firefighters fought the Arizona Dude Fire in the Tonto National Forest. Enhanced winds from a passing thunderstorm GF spread the fire in all directions, but the strongest flow was to the south where the terrain channeled the flow into a canyon killing six firefighters (Goens and Andrews 1998). The combination of small localized thunderstorm downdrafts, complex terrain, and strong surface GFs are also common in several other fatality fires including the 1949 Mann Gulch Fire (Rothermel, 1993), the 1976 Battlement Fire (USDI, 1976), the 1994 South Canyon Fire (USDI/USDA, 1994), the 2012 Waldo Canyon Fire (Johnson et al. 2014), and the 2015 California Frog Fire (Draeger, 2016). Tragic events such as these incentivize the

wildland fire community to better understand GF behavior in areas of complex terrain (Joint Fire Science Program 2017). Despite increased interest, few observations exist of GF properties and behavior in complex terrain regions. Most observational GF studies focus on orographically-flat regions such as the United States Great Plains, analyzing GFs primarily from organized thunderstorms such as supercell thunderstorms, squall lines, or mesoscale convective systems (MCSs) (e.g., Charba 1974; Goff 1976; Engerer et al. 2008; Bryan and Parker 2010). In and near complex terrain, however, thunderstorms are usually less organized as single cell and multicell thunderstorms (Bunkers et al. 2006; Keighton et al. 2007; Parker and Ahijevych 2007; Schneider 2009; Ashley et al. 2019). Despite this, single and multicell mountain thunderstorms can still produce gusty outflow boundaries with surface winds strong enough to significantly alter fire behavior (Goens and Andrews 1998; Luchetti et al. 2020), and, therefore, need to be further evaluated. Motivated by the need for analysis of GF characteristics and evolution in complex terrain regions, this dissertation utilizes observations and model data to: i) enhance observations of GF characteristics in and near complex terrain, ii) link GF propagation and atmospheric characteristics to variability in the underlying terrain, and iii) investigate GF interactions with canyons under a numerical modeling framework.

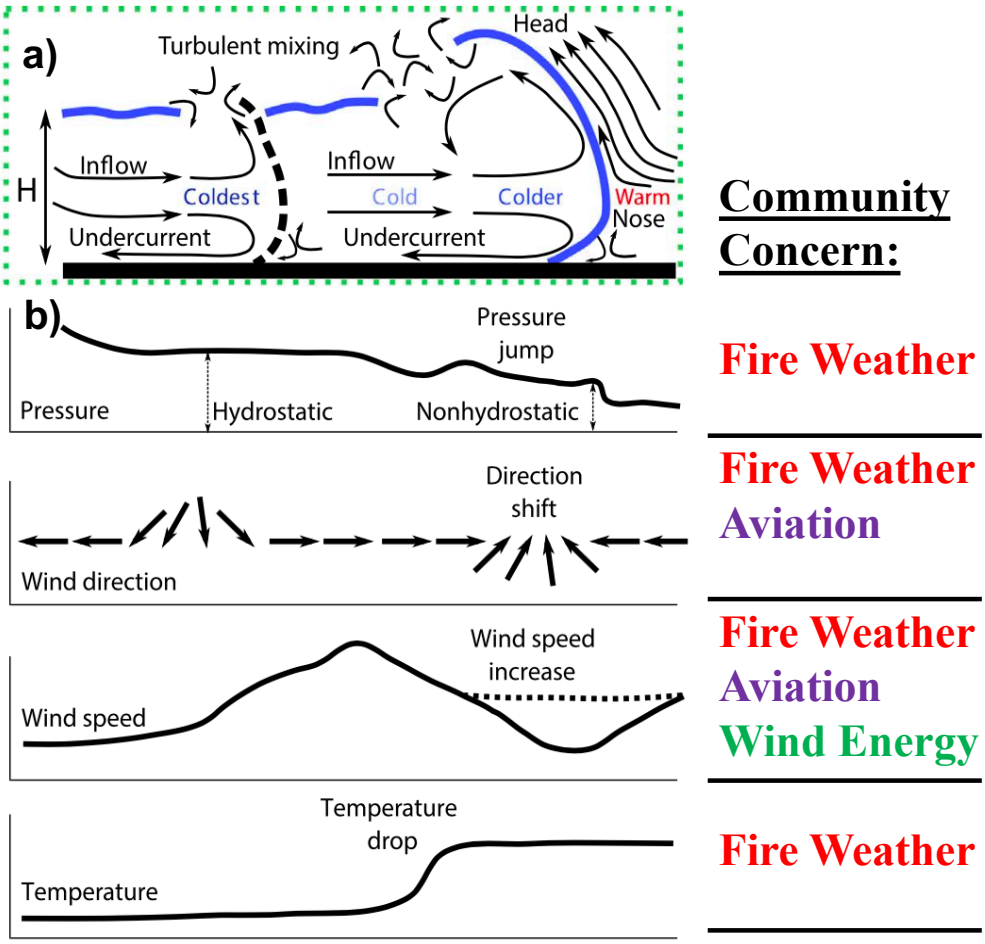

Fig. 1.1. Schematic of the leading edge of a gust front a) and the changes in surface atmospheric parameters associated with a gust front passage b). Specific community concerns for rapid changes in atmospheric parameters during gust front passage are also listed. Adapted and modified from Lompar et al. 2018.

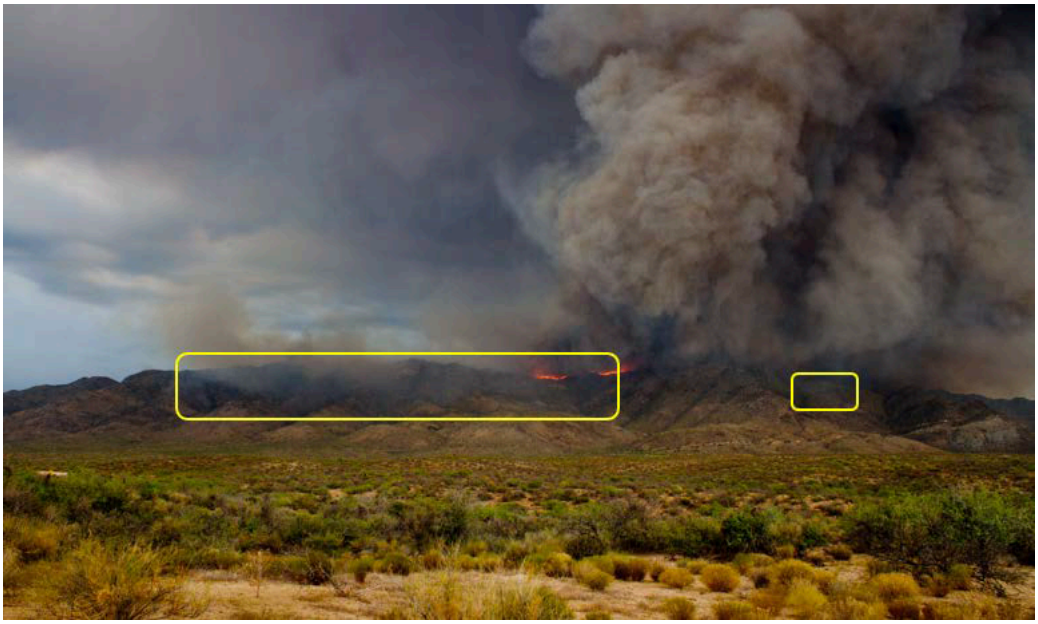

Fig. 1.2. An outflow boundary (yellow boxes) spills over a ridgeline and interacts with a wildfire during the 2013 Yarnell Hill Fire accident. Photo courtesy of Matt Oss Photography. From Karels and Dudley 2013.

Chapter 2 focuses on quantifying the changes in atmospheric variables (temperature, humidity, wind, turbulence) during 24 GFs that occurred near the complex terrain of the Colorado Rocky Mountains using in-situ and remote-sensing instruments. The objectives of this study were to: i) determine how changes in GF properties vary with height in the lowest 300 m above ground level (AGL), ii) relate GF propagation characteristics to the variability in the underlying terrain, and iii) compare changes in atmospheric characteristics associated with Colorado Front Range GFs to those that spawn from organized convection in flatter terrain regions. To fulfill these objectives, Level II radar data from the Next-Generation Radar (NEXRAD) radar located at Denver, Colorado (KFTG) was used to identify GFs and analyze their propagation characteristics to assess the influence of terrain elevation and slope on GF propagation speed. Additionally, data from in-situ instruments mounted on three meteorological towers, a remote-sensing microwave radiometer, and two wind profiling lidars, were used to

quantify changes in horizontal wind speed and direction, vertical wind speed, temperature, relative humidity, turbulence intensity (*TI*), and turbulence kinetic energy (*TKE*) evaluated across all 24 GF events to assess how these characteristics vary with height in the lowest 300 m AGL. Results from this analysis were compared to studies of GFs from organized thunderstorms in flat terrain regions to assess any differences. The work in chapter 2 was published in Monthly Weather Review (Luchetti et al. 2020, "Characterizing Thunderstorm Gust Fronts Near Complex Terrain").

Chapter 3 discusses statistical comparisons of 122 GFs that occurred in the complex terrain regions of New Mexico (NM) and Arizona (AZ). Using operational WSR-88D radars and in-situ data from Automated Surface Observing System (ASOS) stations, GFs that propagated down into and along the Rio Grande Valley in NM were compared to those that were pushed uphill and propagated atop the Mogollon Rim in AZ. The objectives of this study were to answer the following questions: 1) Are there statistical differences in GF propagation and atmospheric characteristics between those that propagate atop a major ridgeline vs. those that propagate down into a major river valley?, and 2) can variability in GF propagation and atmospheric characteristics be linked to the underlying terrain? To answer these questions, this study statistically compares the mean propagation speed and changes in atmospheric characteristics (horizontal wind speed, temperature, relative humidity) between the two study regions, and then explores if any differences can be attributed to variability in terrain slope and elevation. Results are also compared to other observational studies and discussed within the context of density current theory. The work in chapter 3 was published in Monthly Weather Review (Luchetti et al. 2020, "Evaluating Thunderstorm Gust Fronts in New Mexico and Arizona").

Chapter 4 focuses on quantifying canyon-enhancement of microburst outflow winds and turbulence. Microbursts develop from evaporation, melting, and sublimation of precipitation causing strong and turbulent ground level winds which are extremely dangerous to firefighters (Fujita and Wakimoto 1983; Wilson et al. 1984; Fujita 1985; Haines 1988; Wakimoto et al. 1994) (Fig. 1.3). Firefighter vulnerability to microburst outflow winds increases when they occur within canyons, where terrain channeling can rapidly enhance fire intensity and migration (Goens and Andrews 1998; Brown 2002; Esperanza Investigation Team 2006; Coen and Riggan 2010; Sharples et al. 2010) (Fig. 1.4). While some numerical studies have investigated microburst outflow interactions with bell-shaped 2-D hills or mountains, and escarpment-like features (e.g. Letchford and Illidge 1999; Wood et al. 2001; Mason et al. 2007, 2010), none have focused solely on canyons. Thus, the objectives of this study were to 1) quantify canyon-enhancement of wind and turbulence generated by microbursts, 2) determine the influence of canyon slope on microburst outflow winds and turbulence, and 3) explore the influence of canyon location with respect to the downdraft on microburst winds. To fulfill these objectives, idealized microburst and outflow boundaries are simulated using the community numerical Weather Research and Forecasting (WRF) model for both short and long distance canyons with a range of upwind and downwind slopes. The work in chapter 4 is expected to be submitted for publication in Monthly Weather Review.

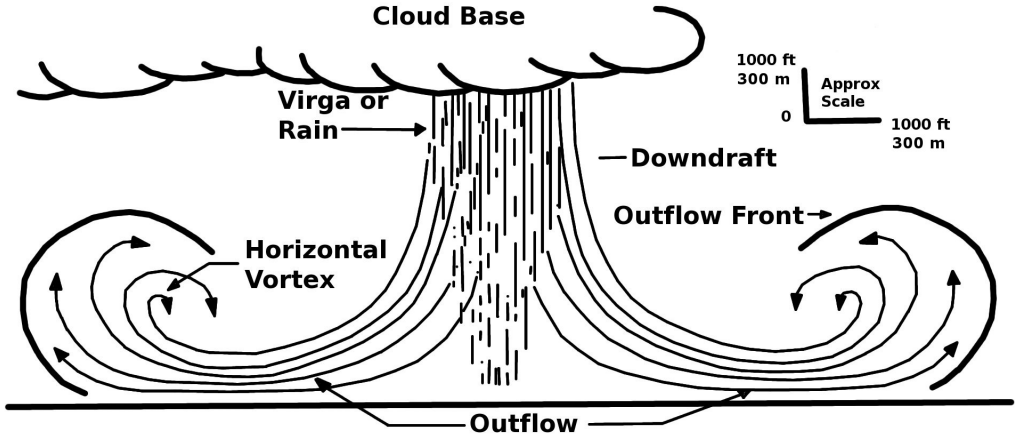

Fig. 1.3. Schematic of a symmetric microburst downdraft and horizontal outflow boundaries. From Federal Aviation Administration, 1988.

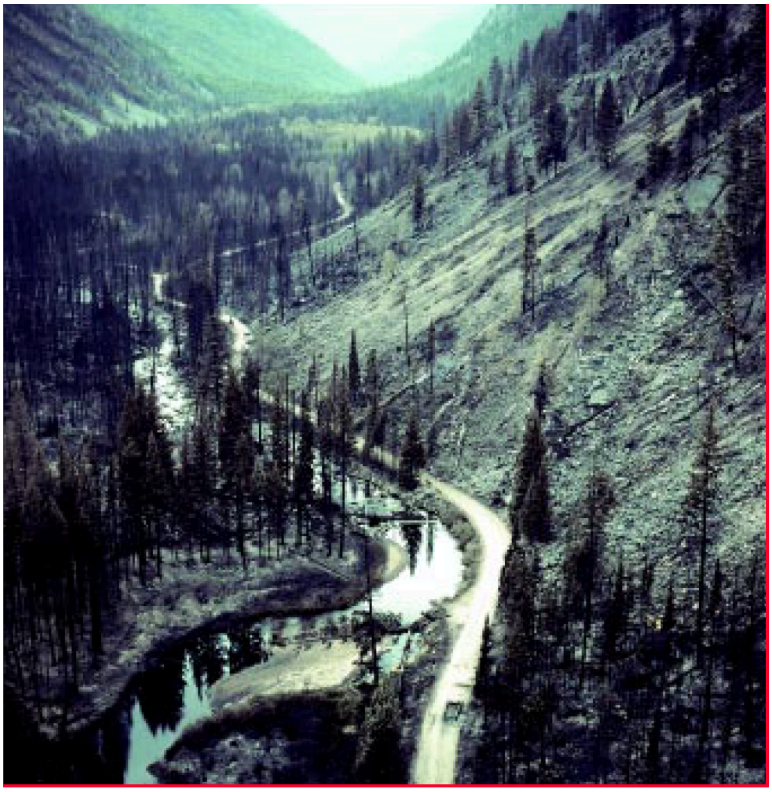

Fig. 1.4. Aerial photo of the 2001 Thirtymile Fire accident location in the Chewuch Canyon, Washington. Fire-induced winds were channeled up the canyon wall killing four firefighters who had deployed fire shelters 30 m up above the road (center right). Photo: Ben Croft, USDA

Forest Service, Missoula Technology Development Center, Missoula, MT, 2001. From Brown 2002.

The overall significance of this work is that it enhances observations and knowledge of GF characteristics and behavior in areas of complex terrain, which have traditionally been neglected throughout the literature. The knowledge gained from the following research provides: 1) forecasters and emergency responders with an extensive quantification of GF properties in and near areas of complex terrain (Chapter 2 and 3), 2) knowledge of the influence of common terrain features on GF characteristics (Chapter 3 and 4), and 3) the quantification of canyon-enhancement of microburst outflow winds and turbulence (Chapter 4).

2 Characterizing Thunderstorm Gust Fronts Near Complex Terrain

This chapter is adapted and reformatted from:

Luchetti, N.T., K. Friedrich, C.E. Rodell, and J.K. Lundquist, 2020: Characterizing Thunderstorm Gust Fronts Near Complex Terrain. *Mon. Wea. Rev.*, **0**, https://doi.org/10.1175/MWR-D-19-0316.1

2.1 Abstract

Fire safety, aviation, wind energy, and structural engineering operations are impacted by thunderstorm outflow boundaries or GFs (GFs) particularly when they occur in mountainous terrain. For example, during the 2013 Arizona Yarnell Hill Fire, 19 firefighters were killed due to sudden changes in fire behavior triggered by a passing GF. Knowledge of GF behavior in complex terrain also determines departure and landing operations at nearby airports, and GFs can induce exceptional structural loads on wind turbines. While most examinations of GF characteristics focus on well-organized convection in areas such as the Great Plains, here the investigation is broadened to explore GF characteristics that evolve near the complex terrain of the Colorado Rocky Mountains. Using in-situ observations from meteorological towers, as well as data from wind-profiling lidars and a microwave radiometer, 24 GF events are assessed to quantify changes in wind, temperature, humidity, and turbulence in the lowest 300 m AGL as these GFs passed over the instruments. The changes in magnitude for all variables are on average weaker in the Colorado Front Range than that typically observed from organized, severe storms in flatter regions. Most events from this study experience an increase in wind speed from 1 to 8 m s^{-1}, relative humidity from 1 to 8 %, and weak vertical motion from 0.3 to 3.6 m s^{-1} during GF passage, while temperature drops by 0.2 to 3° C and turbulent kinetic energy peaks at > 4 m^2 s^{-2}. Vertical profiles reveal that these changes vary little with height in the lowest 300 m.

2.2 Introduction

Forecasting and monitoring the potential for severe wind damage associated with thunderstorm outflow boundaries or GFs is important for structural and personal safety across a variety of sectors such as aviation, structural engineering, wind energy, the wildland fire community, and the emergency response community. A GF is the leading edge of cold air propagating horizontally away from a thunderstorm (Simpson 1969; Droegemeier and Wilhelmson 1987). The pool of cold air results from the evaporation of liquid water and the melting and sublimation of frozen hydrometers (e.g., hail or graupel) in the thunderstorm downdraft. Despite increased interest in understanding the evolution of GFs, few observations exist of GF effects on atmospheric properties (wind, temperature, humidity, turbulence) in mountainous terrain because of the limitation and sparsity of weather observations. Most observational GF studies focus on orographically-flat regions such as the United States Great Plains (e.g., Charba 1974; Goff 1976; Engerer et al. 2008; Bryan and Parker 2010). These studies mainly analyze GFs from organized thunderstorms such as supercell thunderstorms, squall lines, or mesoscale convective systems (MCSs). In and near complex terrain, however, thunderstorms are usually less organized as single cell and multicell thunderstorms (Bunkers et al. 2006; Keighton et al. 2007; Parker and Ahijevych 2007; Schneider 2009; Ashley et al. 2019). In this study, we analyze the changes in atmospheric properties of 24 GFs observed with remote-sensing and in-situ instruments in the Colorado Front Range with the goal of identifying and comparing atmospheric properties of GFs near complex terrain to those observed in flat terrain.

GFs can be associated with strong turbulence and rapid wind increase and shear creating potential dangers to humans and structures. During the 2013 Yarnell Hill Fire in Arizona, for example, 19 firefighters were killed because of rapid and severe changes to the fire's behavior,

driven by a GF moving over the fire (Hardy and Comfort 2015; Paez et al. 2015). Tragic events such as this one incentivize the wildland fire community and emergency responders to better understand the evolution of GFs in areas of complex terrain (Joint Fire Science Program 2017). Similarly, GFs can exert loads on structures like buildings and wind turbines, motivating attention from the structural engineering community (Chay et al. 2006; Kwon and Kareem 2009; Lombardo et al. 2014, 2018; Solari et al. 2015). Vertical wind shear and turbulence can directly impact the productivity of a wind turbine and influence the lifetime of its rotor blades and other components (Manwell et al. 2002; TC88-MT, I. E. C. 2005; Nguyen et al. 2011; Lu et al. 2019). Wind turbine design engineers are, therefore, concerned with potential structural damage from interactions with strong GFs (Letchford et al. 2002; Solari 2014, Lombardo et al. 2018). The duration of the peak wind gusts and turbulence associated with GF passage also has a critical role in the response of structures to wind loading (Kwon and Kareem 2009; Lombardo et al. 2018; Zhang et al. 2018). Engineers must understand both the intensity of wind speeds associated with GFs, as well as the duration over which structures are exposed to peak gusts and turbulence.

GFs often behave like density or gravity currents (Benjamin 1968; Charba 1974; Sasaki and Baxter 1986; Friedrich et al. 2005; Bryan and Rotunno 2008). On their leading edge, a nose-like shape forms which tends to be deeper and marks the region where the strongest lift and convergence between the outflow and environmental air occurs. GFs are typically on the order of 0.5 – 2 km deep; however, this depth can range between 100 m and 4 km, depending on the strength and distance from the downdraft source (Cotton et al. 2011). For example, GF depth associated with MCSs have been observed to be greater than 4 km (Bryan 2005; Bryan and Parker 2010). As a GF passes over a meteorological weather station, observations typically report an abrupt change in wind direction and speed, a decrease in temperature, and an increase

in humidity (Simpson 1969; Charba 1974; Goff 1976; Fujita 1981; Droegemeier and Wilhelmson 1987; Lompar et al. 2018). The intensity of such changes is proportional to the strength and depth of the passing GF. Few observational studies on GF behavior in mountainous or near-mountainous terrain exist (Mahoney 1988; Bidokhti and Bani-Hashem 2001; Kishscha et al. 2016). Most of these GFs originated from thunderstorms that are less organized compared to GFs from MCSs or supercell thunderstorms often studied in the United States Great Plains. The lack of organization in mountainous or near-mountainous thunderstorms can be linked to reduced temperatures, low-level moisture, and surface-based instability compared to lower elevations (Bunkers et al. 2006; Keighton et al. 2007; Schneider 2009). However, given the increase in high impact wind-driven wildfire events in recent years, there is a need to study GFs from less-organized thunderstorms that initiate in areas of complex or near-complex terrain.

Motivated by the need to better comprehend GF characteristics in and near mountainous terrain, this study quantifies the duration and magnitude of shifts in temperature, wind, turbulence, and moisture associated with GFs and how these characteristics vary with height in the lowest 300 m AGL. Section 2.3 discusses the datasets used, including location, instrumentation, and local physiography for each of the two study sites. Section 2.4 discusses methods emphasizing the detection, quantification, and statistical techniques used to assess GFs in this study. Results are presented in Section 2.5. Discussion of the results and how they compare with GFs observed in flat terrain is found in Section 2.6. Conclusions and suggestions for future work are discussed in Section 2.7.

2.3 Study Sites and Instruments

2.3.1 Colorado Study Site Descriptions

Data from two field campaigns conducted along the Colorado Front Range (Fig. 2.1) are used for this analysis. The first dataset consists of measurements from in-situ and remote-sensing instruments that were deployed during the Experimental Planetary Boundary Layer Instrument Assessment (XPIA) campaign (Lundquist et al. 2017; https://a2e.energy.gov/projects/xpia) which took place from 1 May – 30 June 2015. The XPIA campaign was located at the Boulder Atmospheric Observatory (BAO; Fig. 2.1). The BAO (Kaimal and Gaynor 1983; Wolfe et al. 2018) is located about 25 km east of the eastern slopes of the Rocky Mountains and 25 km north of downtown Denver, Colorado, at an elevation of 1584 m mean sea level (MSL). The second dataset consists of measurements from an instrument comparison campaign conducted at the National Wind Technology Center (NWTC) at the National Renewable Energy Laboratory (Fig. 2.1), also along the Colorado Front Range. Covered mostly by short grass, the NWTC is located about 4 km east of the eastern slopes of the Rocky Mountains and 20 km northwest of Denver, Colorado, and is situated at 1852 m MSL (Clifton and Lundquist 2012; Clifton et al. 2013; Aitken et al. 2014). Some instruments only operated for a limited time between 1 May – 31 August 2012, 1 June – 30 June 2013, and 1 May – 30 June 2014. Both sites are located on slightly elevated hills and are frequently influenced by terrain-channeled drainage flow, down sloping katabatic winds, or general terrain-induced diurnal circulations from the nearby Colorado Front Range mountains (Banta et al. 1993; Clifton and Lundquist 2012). Thunderstorms that develop near these sites also tend to be weaker and less organized until they propagate into far eastern Colorado where the terrain is less rugged and organization is more favorable (Cotton et al. 1983; McAnelly and Cotton 1986; Tucker and Crook 1999).

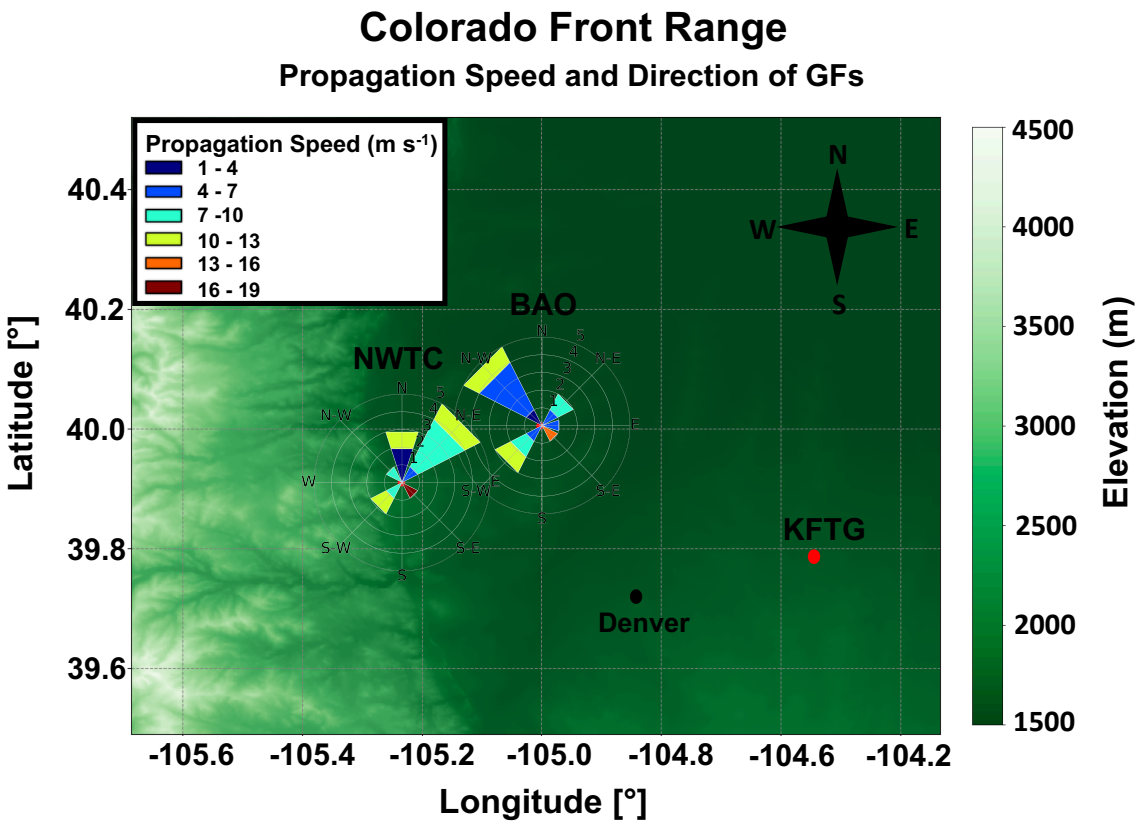

Fig. 2.1: Topographic map showing the Colorado study site locations: Boulder Atmospheric Observatory (BAO) and the National Wind Technology Center (NWTC). The location of the NWS Denver (KFTG) NEXRAD radar site is shown as a red circle. Rose diagrams at each site indicate the number of GFs (range values), the direction in which the GFs propagated from, and their propagation speeds (m s^{-1}; color coded).

2.3.2 Description of In-Situ Research Instruments

In-situ observations from one meteorological tower at the BAO and two towers at the NWTC are used in this study (Table 2.1). The 300-m BAO tower provides wind, temperature, and relative humidity measurements at 2, 10, 100, and 300 m AGL every 1 min (Kaimal and Gaynor 1983; Wolfe et al. 2018). Vaisala HMP temperature and relative humidity probes have accuracies of ± 0.1 °C and ± 0.8 %. Horizontal wind is measured every 2 s at 10 and 100 m AGL using prop vane anemometers and at 300 m using a 2 D sonic anemometer with accuracies

of ± 0.1 m s^{-1} for wind speed and ± 1° for wind direction. In addition, two 3 D sonic anemometers (Cambell CSAT3) providing vertical and horizontal wind and six Sensiron SHT75 solid-state temperature/relative humidity sensors were also deployed at six levels (for measurement heights and accuracy see Table 2.1). Anemometers are deployed on two boom arms, pointing at 334° and 154° from north, respectively. Inaccuracies and biases in wind and turbulence measurements are introduced when the tower structure is in the wake of the ambient flow (McCaffrey et al. 2017). To avoid impacts from the tower on wind measurements, we only consider winds between 25° and 100° and 175° and 300° following McCaffrey et al. (2017), which reduces the wind analysis by four events.

Wind observations from all anemometers are used to derive turbulence intensity (*TI*). *TI* is the ratio of the standard deviation of the horizontal wind speed (σ_v in m s^{-1}) and the mean horizontal wind speed ($\bar{V}$ in m s^{-1}), both averaged over 2 min:

$$TI = \sigma_v / \bar{V} \qquad (2.1)$$

In this study, we will discuss maximum and mean *TI* during the time of GF passage. The 3 D wind field from the sonic anemometers is also used to assess the turbulence kinetic energy (*TKE*):

$$TKE = 0.5[u'u' + v'v' + w'w'] \qquad (2.2)$$

The variance of the wind components (u', v', w') is calculated over 2-min intervals, and we then calculate the maximum and mean *TKE* over the duration of GF passage.

In addition to the BAO towers, two meteorological towers at the NWTC (M2 and M4) are used in this analysis. At the NWTC M2 tower, wind every 2 s is sampled using the Met One WS-201 instruments from which 1-min winds, maximum and mean *TI* are derived (specifics listed in Table 2.1). Met One T-200A temperature sensors sample every 2 s at only 2, 50, and 80 m AGL with 1-min average output and accuracies of ± 0.1°C. Relative humidity and dewpoint temperature are sampled at 2 m every 2 s and averaged to 1-min output (Jager et al. 1996; Johnson et al. 2000).

Observations from the NWTC M4 tower (Clifton et al. 2013) include Met One SS-201 cup anemometers and Met One SD-201 wind vanes that measure horizontal wind at 3, 10, 26, 88, and 134 m AGL with accuracies of 0.5 m s^{-1} and 3.6°. Additionally, 3-D ATI "K" Type sonic anemometers are mounted at 15, 30, 50, 76, 100, and 131 m AGL with accuracies of 0.01 m s^{-1}. Maximum and mean *TI* are calculated from the cup anemometer observations, while maximum and mean *TKE* is derived from the 3 D sonic anemometers. Temperature is measured at 3, 26, and 88 m AGL using a Met One T-200A probe and at 15, 30, 50, 76, 100, and 131 m AGL using the ATI 'K' Type sonic anemometers with accuracies of ± 0.1°C for both instruments. Lastly, dewpoint temperature using a Therm-x 9400ASTD sensor and relative humidity are available at 3, 26, and 88 m AGL. All M-4 tower instruments sample at 20 Hz averaged to 1-min output (Clifton et al. 2013; Clifton 2014). To avoid tower-wake impacts (Clifton 2014), we only consider winds between 25° and 100° and 175° and 300°; we removed one event at the NWTC.

Table 2.1. Research instruments deployed along the Colorado Front Range and their instrument specifics. The top bolded box highlights the tower and in-situ instruments. The bottom bolded box highlights the remote-sensing instruments.

Instrument/Facility	Output frequency (min)	Measurement heights (m) AGL	Variables measured/derived	Accuracy
Boulder Atmospheric Observatory (BAO) 300 m Meteorological Tower - **XPIA**	1	2, 10, 100, 300	u,v component of wind, turbulence intensity, temperature, relative humidity	Temperature: ± 0.1 °C, Relative Humidity: 0.8 %, Wind Speed: ± 0.1 m s^{-1} Wind Direction: ± 1 °
BAO Additional Instruments (Cambell CSAT3 3-D Sonic anemometers, Sensiron SHT75 solid-state temperature and humidity probes) - **XPIA**	1	50, 100, 150, 200, 250, 300	u, v and w component of wind, turbulence intensity, turbulent kinetic energy, temperature, relative humidity	Temperature: ± 0.1 °C Horizontal Wind Speed: ± 0.08 m s^{-1} Vertical Wind Speed: ± 0.04 m s^{-1}
National Wind Technology Center (M2) Tower with T-200 A temperature probe, Met One WS-201 wind sensor system - **NWTC**	1	2, 5, 10, 20, 50, 80	u, v component of wind, turbulence intensity temperature, 2 m relative humidity	Temperature: ± 0.1 °C, Wind Speed: ± 0.5 m s^{-1} Wind Direction: ± 3.6 °
NREL National Wind Technology Center (M4) Tower with T-200 A temperature probe, Met One SS-201 cup anemometers, Met One SD-201 wind vanes, ATI ‘K” Type 3-D Sonic anemometers, AIR AB-2AX pressure probe - **NWTC**	1	3, 10, 15, 26, 30, 50, 76, 80, 88, 100, 131, 134	u, v and w component of wind, turbulence intensity, turbulent kinetic energy, temperature, relative humidity	Temperature: ± 0.1 °C Cup - Wind Speed: ± 0.5 m s^{-1} Sonic - Wind Speed: ± 0.01 m s^{-1} Wind Direction: ± 3.6 °
Leosphere/NRG WINDCUBE, version 1 (v1) profiling lidars (WC68) - **NWTC**	1	40, 60, 80, 100, 120, 140, 160, 180, 200, 220	u, v, and w component of wind, turbulence intensity, turbulent kinetic energy	Wind Speed: ± 0.05 m s^{-1}
Leosphere/NRG WINDCUBE, version 2 (v2) profiling lidars (WC16) - **XPIA**	1	40, 50, 60, 80, 100, 120, 140, 160, 180, 200	u, v, and w component of wind, turbulence intensity, turbulent kinetic	Wind Speed: ± 0.05 m s^{-1}

			energy	
Microwave Radiometer - Radiometrics MWR-3000A – **XPIA/NWTC**	2	50 to 6000 m by 50 m intervals	Temperature, relative humidity	Temperature: ± 1 °C

2.3.3 Description of Remote-Sensing Research Instruments

In addition to tower observations, both sites use a Radiometrics MWR-3000A microwave radiometer and Leosphere/NRG Windcube lidars. A summary description of the microwave radiometer and Windcube lidars and their operations, including temporal and spatial resolution, as well as accuracy at each site, are shown in Table 2.1 and in Friedrich et al. (2012), Bianco et al. (2017), and Lundquist et al. (2017). The Radiometrics MWR-3000A microwave radiometer provides vertical profiles of temperature and relative humidity (Solheim et al. 1998a, 1998b; Rosenkranz 1998). Vertical profiles of temperature and relative humidity are derived at 2-min intervals using a radiative transfer model and a 5-year radiosonde climatology for Denver, Colorado. Accuracy of the temperature retrieval was found to be within ± 1°C below 300 m AGL based on tower, radiosonde, and radiometer temperature intercomparisons at the NWTC and BAO (Friedrich et al. 2012; Lundquist et al. 2017; Bianco et al. 2017). Here, we use radiometer-retrieved temperature and humidity at 50, 100, 150, and 300 m AGL to quantify changes in thermodynamics near the surface, and temperature up to 6 km to quantify the depth of cold air behind the leading edge of each GF.

Both sites also utilized measurements from Leosphere/NRG Windcube lidars. For events at the NWTC, data from a Windcube version 1 (v1) profiling lidar (WC68) are used. The WindCube v1 lidar operates at the 1.5-μm wavelength and samples line-of-sight (LOS) velocities

across four cardinal directions each angled at 28° from zenith. Each angled beam simultaneously samples 10 range gates (see Table 2.1 for measurement range heights) (Courtney et al. 2008; Lundquist et al. 2017). The v1 lidar derives horizontal and vertical velocities every 1 Hz using a Doppler Beam Swinging (DBS) approach (see Eq. 1-3 in Lundquist et al. 2015) that are averaged to 1-min intervals. In the DBS approach, the backscattered radiation will create a shift in the frequency based on how rapidly particles are moving away or towards the lidar along each LOS. Vertical profiles of the LOS velocity can then be calculated by shifting the beam between the four radial wind directions, and by taking the difference between the arrival time of the backscatter and the initiation of the pulse at each measurement height (Lundquist et al. 2015). Using DBS-based wind field and its variance, the maximum and mean lidar *TI* and *TKE* (Rhodes and Lundquist 2013) are derived using Eqs. (2.1-2.2) at all available lidar heights. The WindCube v2 lidar, deployed during XPIA, is similar to the v1 version, but operates with an additional fifth beam pointed zenith, which directly measures the vertical wind component. The v2 lidar sampling heights, different than the v1 lidar, and ranges are listed in Table 2.1 (Bodini et al. 2018). The accuracy of lidar-derived wind velocities is a function of an assumed horizontal homogeneity across the scanning cone at each height. In coastal flat areas, the Windcube accuracy is ± 0.05 m s^{-1} with a standard deviation of 0.15 m s^{-1} in sheared conditions (Sathe et al. 2011).

2.4 Methods

2.4.1 GF Detection and Magnitude and Rate Change Calculation

Weather radars identify the leading edge of GFs as a line of enhanced radar reflectivity (also known as the radar fine line; Rauber and Nesbitt 2018). As the spreading cold air associated with

a GF travels away from the parent thunderstorm, the air ahead of an advancing GF is lifted, insects and dust are lofted, and a shelf cloud can form, which become detectable by radar (Fig. 2.2; Wilson and Schreiber 1986; Rauber and Nesbitt 2018). To detect radar fine lines in this study, we use Level II radar reflectivity at the lowest elevation angle of 0.5° observed from the Next-Generation Radar (NEXRAD) radar located at Denver, Colorado (referred to as KFTG hereafter; Fig. 2.1). Level III radar products and Level II data are used to characterize the parent thunderstorms. As KFTG is about 48 km and 59 km southeast of the BAO and NWTC, respectively, the height of the lowest radar beam is about 0.6 km AGL over the BAO site and about 0.7 km AGL over the NWTC site. To determine GF events, we first identify days during the campaigns when thunderstorms developed in the vicinity of the instrument sites. Next, we classify GF events by visually identifying lines of enhanced (5 – 25 dBZ) reflectivity (Wilson and Schreiber 1986; Koch and Ray 1996) traveling away from parent thunderstorms and passing over the instruments (Fig. 2.2). During the XPIA and NWTC instrument operations, we identified 12 GFs passing over the NWTC and 12 GFs passing over the BAO. Radar observations are used to: (i) characterize the parent thunderstorm (thunderstorm type, size, strength, and duration), (ii) analyze radar-based GF characteristics (propagation speed and direction and distance from parent thunderstorm at time of passage), and (iii) determine the relative time the GF passed over the instruments.

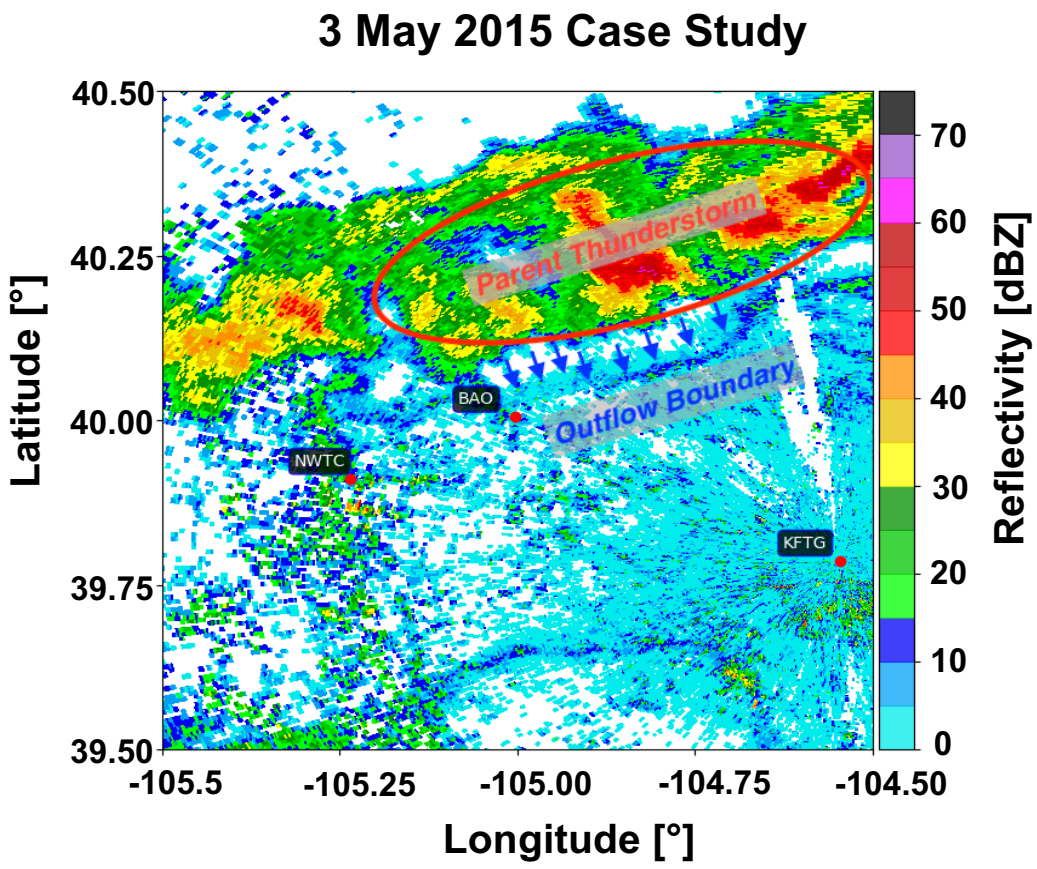

Fig. 2.2: Radar reflectivity at 0.5 ° elevation angle showing a thunderstorm and GF passing over the BAO on 3 May 2015 at 21:20 UTC observed by KTFG operational radar at Denver, Colorado.

Parent thunderstorms are classified as single-cell, multicell, or supercell thunderstorms following Smith et al. (2012). We also characterize each parent thunderstorm 10 min prior to the time we first detect the radar fine line to compare amongst each case but also to compare the results to other studies. These characteristics include the maximum height at which radar reflectivity (Z) ≥ 18 dBZ (radar echo tops), maximum rainfall rate between the lowest and highest scan angle, and the areal extent of $Z \geq 35$ dBZ at the lowest scan angle of each parent thunderstorm. Rainfall rate (R) estimates are derived from the relation $Z = 300\ R^{1.5}$. We also determine the parent thunderstorm duration from downdraft to dissipation stage, which is the

time 10 min prior to the radar fine line detection and the time the parent thunderstorm dissipated ($Z < 20$ dBZ).

GF propagation speed is calculated using an observational technique tracking the radar fine line and then compared to the theoretical propagation speed for density currents. The observed propagation speed is calculated by tracking the radar-detected fine lines and calculating the displacement of the fine line signature over time as it approaches and eventually passes through the research sites. Considering that radar fine lines tend to morph into bowing or other irregular shapes, we account for this by determining an approximately 10-km mean positional swath across the leading edge of the front as it moves over the instruments. The swath displacement is then tracked backwards to calculate the mean propagation speed between the time the fine line was first detected and the time it passed over the instrument.

GFs are considered density currents with dense cold air propagating into an environment of less dense and warmer air. Therefore, the theoretical propagation speed for density currents explicitly incorporates cold pool perturbations ($\Delta\theta$ in °C) and cold air depth (h in m) and can be considered a measure of GF intensity. It is calculated following Benjamin (1968), as:

$$c = \sqrt{\frac{\Delta\theta}{\theta} g h} \qquad (2.3)$$

where c is the frontal propagation speed (m s^{-1}), g is gravitational acceleration (m s^{-2}), and θ is the ambient air temperature (°C). We utilize 10 m measurements from the towers to calculate the cold pool perturbation and ambient temperature prior to frontal passage. Here, we consider h to be the depth of the trailing cold air behind the head of each GF. To obtain h we use the 2-minute averaged vertical temperature profiles from the microwave radiometer between the

surface and 6 km and determine the height at which the differences in temperature before and after the passage time is less than 1 °C, which corresponds to the accuracy of the temperature retrieval. The heights are determined with an accuracy of about ± 20 m. Both radar-derived and theoretical propagation speed are analyzed and compared across all GF events.

For each GF that passed over the instrument site, we analyze the change in wind speed, wind direction, temperature, and relative humidity during the GF passage (referred to as magnitude change) and the time over which this magnitude change occurs (referred to as rate change). Magnitude and rate change are analyzed separately for each variable and measurement height (see example of GF-induced wind speed change in Fig. 2.3). In order to unambiguously identify the GF passage, an approximate time over which GFs pass over the research sites is first derived by using KFTG radar data. In-situ and remote-sensing data are then analyzed 30 min before and 30 min after the radar-derived GF passage time (white shading shown in Fig. 2.3). Within this time frame, we determine the time period over which the largest gradient in the atmospheric variables occurs for each height level and each variable (yellow box in Fig. 2.3, referred to as GF passage period or GPP). Note that the GPP can differ depending on the instrument, measurement height, variable, and event. However, for the events discussed here the typical GPP for most of the variables occurs within the same time frame for each case, and the variance in GPP with height is negligible.

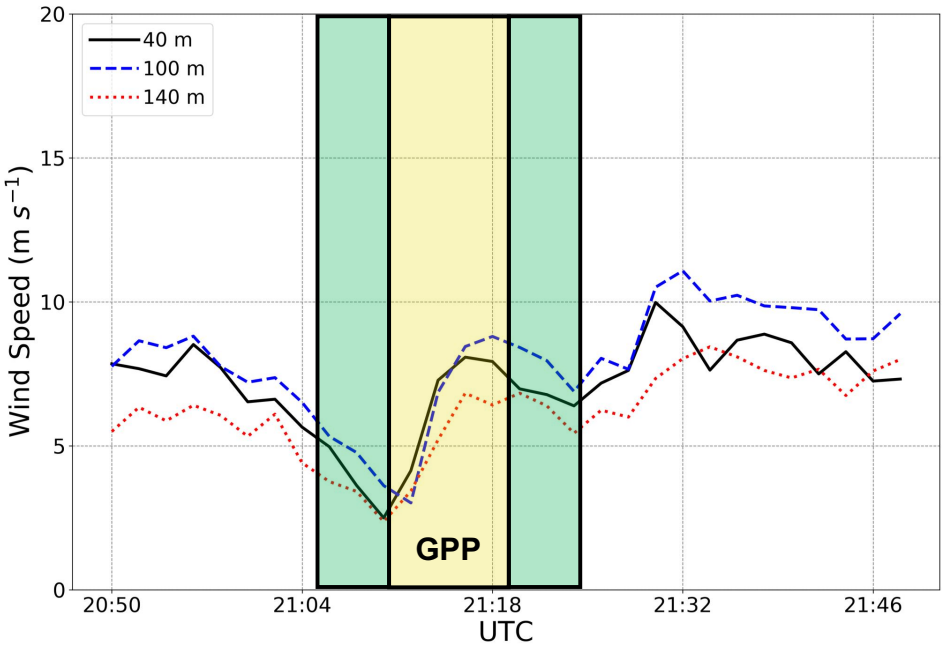

Fig. 2.3: Remotely sensed temporal evolution of wind speed at 40 m (black solid line), 100 m (blue dashed line), and 140 m (red dotted line) during a GF passage on 5 May 2015 over the BAO site. White area indicates the time 30 minutes prior to, and 30 minutes after the radar-derived GF passage time. The yellow highlighted box represents the GF Passage Period (GPP). The green highlighted areas represent the 5-min intervals where each variable is averaged in order to calculate the difference in the boundary variable prior to and after the GPP.

We then quantify the magnitude change for each variable by taking the difference between the 5-min mean of the variable prior to and after the GPP (green boxes in Fig. 2.3). We perform a sensitivity analysis comparing 5, 15, and 30-min averages to determine which averaging time most accurately represents the change in GF variables (not shown). The results indicate that a 5-min period most accurately represents conditions prior and after the GPP for the cases analyzed in this study. The magnitude change is then divided by the GPP to obtain a gradient value normalized by the duration for each variable or rate change. We conduct a t-test to determine if the differences in magnitude and rate change between any of the variables observed at the NWTC and BAO are statistically significant when comparing the two study sites. As no

statistically significant difference between the datasets is found ($p = 0.05$), we combine the measurements from the BAO and the NWTC sites and conduct a joint analysis of the 24 GF events.

Vertical profiles of changes in atmospheric variables are derived combining all available GF events. Note that while most measurement heights have data from only one instrument for each event, there are a few heights (10, 50, 80, 100, 300 m) where the instrument platforms overlap. At heights where an overlap occurs, we first merge the two data sets by averaging the measurements between the two instrument platforms. Differences in temperature are typically within ± 1°C when comparing the radiometer and in-situ temperature probes, and ± 1 m s^{-1} for horizontal wind between the lidars and wind anemometers. Vertical motion differences are negligible, within ± 0.5 m s^{-1} when comparing direct measurements from the 3-D sonic anemometers and derived measurements using the v1 lidar DBS approach. Once we have data points representing each event for each measurement height, we calculate median and interquartile ranges.

2.5. Results

2.5.1 Radar and GF Depth Analysis

During the instrument deployments, thunderstorms develop within close proximity to the study sites on 118 days with only 22 (~17 %) days where observed radar fine lines propagate through the study sites (Table 2.2). As multiple GFs passed through the instrument sites on 2 separate days, a total of 24 GF events are included in the following analysis. Ten (~42%) of the 24 GFs initiate from single-cell thunderstorms, 13 (~54 %) initiate from multicell cluster thunderstorm complexes, and 1 (4 %) event stems from a supercell thunderstorm where rotation

was evident in the radar Doppler velocity field. After the thunderstorms generate a GF, they continue to persist on average for another 58 minutes, with a minimum persistence time of 31 min and a maximum of 180 min (Fig. 2.4a). Additionally, the median echo top height 10 min prior to the first detection of each radar fine line was 9.1 km and the maximum related to the supercell thunderstorm was 16.8 km (Fig. 2.4b). Maximum rainfall rates 10 min prior to the first detection of each radar fine line ranges from 2.3 - 6.9 mm hr^{-1} (Fig. 2.4c). Medium maximum areal extent within the 35 dBZ isoline of each thunderstorm is 108 km^2, with a maximum areal extent of 527 km^2 (Fig. 2.4d).

Table 2.2. List of dates for each of the 24 GF events and their corresponding campaign. Multiple GF events occurred on 4 June 2015 and 16 June 2015 at the XPIA campaign site. The GF passage time is also included for each case.

NWTC		**XPIA**	
Date	**Time of Passage**	**Date**	**Time of Passage**
5 June 2012	01:15 UTC	3 May 2015	21:20 UTC
2 July 2012	23:14 UTC	31 May 2015	20:22 UTC
7 July 2012	22:18 UTC	1 June 2015	19:41 UTC
16 July 2012	21:41 UTC	3 June 2015	23:53 UTC
25 July 2012	21:28 UTC	4 June 2015 (1)	22:57 UTC
27 July 2012	18:19 UTC	4 June 2015 (2)	23:24 UTC
1 August 2012	21:12 UTC	7 June 2015	22:51 UTC
18 June 2013	02:44 UTC	13 June 2015	22:51 UTC
23 June 2014	00:42 UTC	16 June 2015 (1)	22:35 UTC
25 June 2014	21:13 UTC	16 June 2015 (2)	23:17 UTC
26 June 2014	01:41 UTC	24 June 2015	23:45 UTC
27 June 2014	07:22 UTC	25 June 2015	21:51 UTC

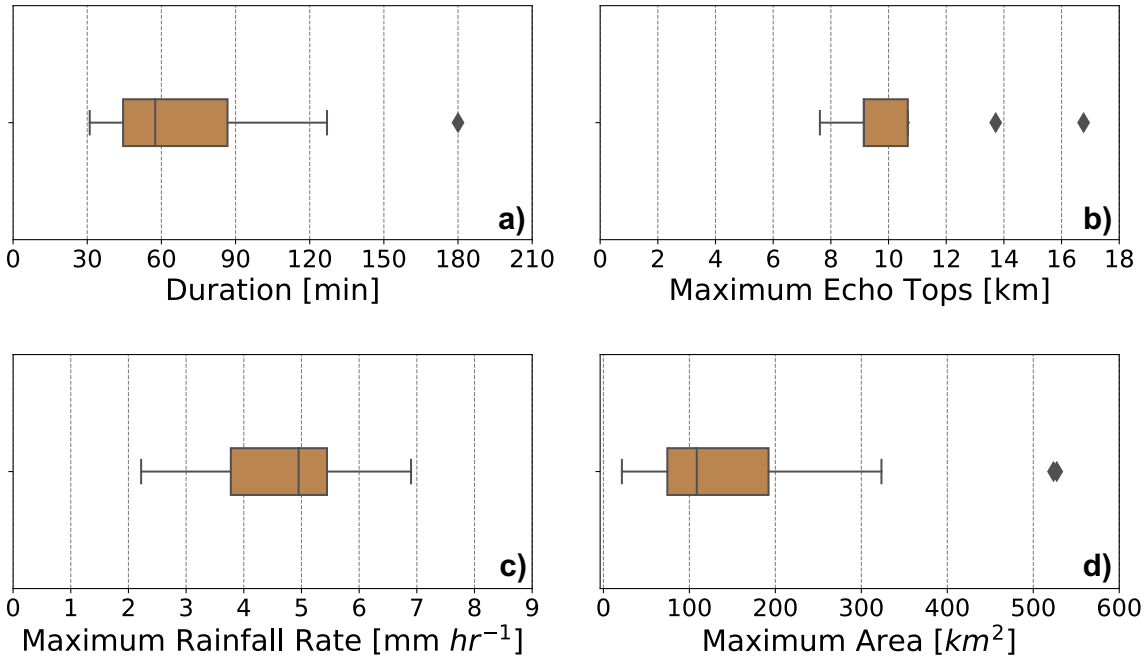

Fig. 2.4: Box-and-whiskers plots of radar-derived parent thunderstorm characteristics. Variables analyzed include a) duration from the time 10 min prior to GF detection and the time the parent thunderstorm dissipated (Z < 20 dBZ) (min), b) parent thunderstorm maximum radar echo tops 10 min prior to GF detection (km), c) parent thunderstorm maximum rainfall rate from the lowest to highest can angle 10 min prior to GF detection (mm hr^{-1}), and d) parent thunderstorm areal extent of $Z \geq 35$ dBZ at the lowest scan angle 10 min prior to GF detection (km^2). The filled box represents the interquartile range. The whiskers extend to data points that fall within 1.5 times the interquartile range of the lower and upper quantiles. Outliers that fall beyond this range are independently represented by diamond symbols.

Of the 24 GF events, 5 (~21 %) GFs propagate from the southwest (rose diagrams in Fig. 2.1), 2 (~8 %) from the southeast, 1 from the east (~4%), 7 (~29 %) propagate from the northeast, 3 (~13 %) from the north, and 6 (25 %) from the northwest. The median radar-derived GF propagation speed at time of passage is 7.6 m s^{-1} with a maximum and minimum propagation speed of 16.6 m s^{-1} and 1.2 m s^{-1}, respectively (Fig. 2.5a). Bryan and Rotunno (2008) show that observed GF propagation speed in the atmosphere can be as much as 25% slower compared to the theoretical speed, which applies better to laboratory flow or shallow density currents. Deeper

atmospheric cold pools often show larger variations in density with height compared to laboratory flow. Faster theoretical propagation speeds are also observed in the cases discussed here with median values of 13.0 m s^{-1} and maximum (minimum) propagation speed of 24.6 m s^{-1} (4.7 m s^{-1}). The correlation between radar-derived propagation speed and the theoretical density current speed is 0.36 (statistically significant at $p < 0.10$). While the depth of the observed cold pool is discussed later, we will now focus on the role of ambient wind ahead of the GF, which is not included in the theoretical propagation speed (Eq. 3).

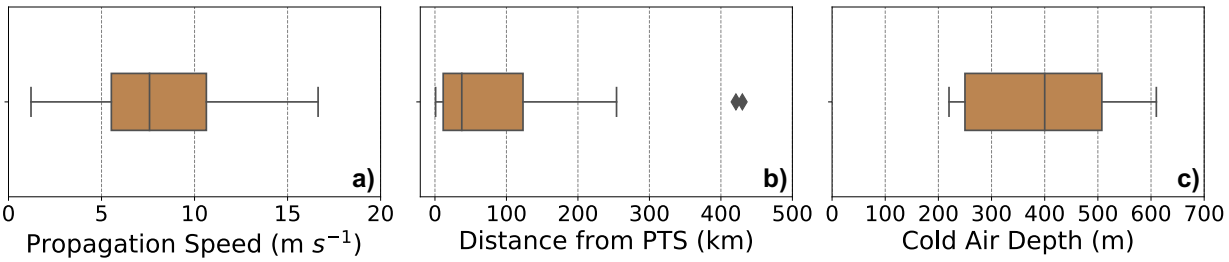

Fig. 2.5: Box-and-whiskers plots of radar-derived thunderstorm and GF characteristics. Variables analyzed include a) radar-derived propagation speed (m s^{-1}), b) distance from parent thunderstorm (PTS) (km), and c) cold air depth (m). The filled box represents the interquartile range. The whiskers extend to data points that fall within 1.5 times the interquartile range of the lower and upper quantiles. Outliers that fall beyond this range are independently represented by diamond symbols.

If we consider the influence of the pre-frontal cross-front ambient wind component in the theoretical propagation speed calculation (following Simpson and Britter 1980; Jorgensen et al. 2003), we find that the theoretical propagation speed decreases in each case and the correlation between observed and theoretical propagation speed increases to 0.48 (statistically significant at $p < 0.05$). Fitting the observed propagation speed to the pre-frontal ambient wind through linear regression (Fig. 2.6), we find that faster GFs often do not have stronger tailwinds with $R^2 = 0.2$

(statistically significant at $p < 0.05$). Since the ambient wind is not a strong determining factor for GF propagation speed in the cases discussed here, we will next investigate the role of topography.

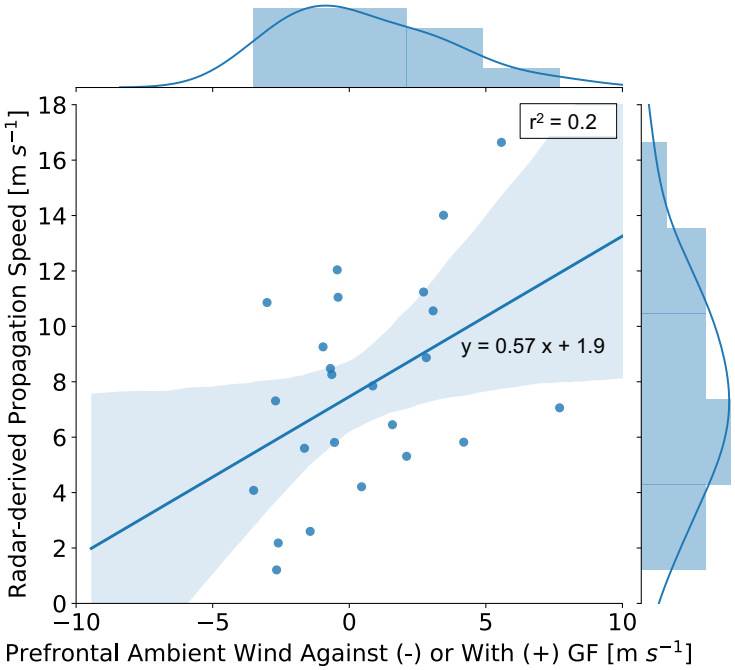

Fig. 2.6: Comparison of radar-derived propagation speed (m s^{-1}) as a function of the prefrontal cross-front ambient wind component (m s^{-1}). The prefrontal cross-front ambient wind components are derived by wind anemometers deployed on towers and measured at 10 m above the surface. The variance explained is listed in the upper right corner. Additionally, a linearly regressed fit is plotted as the solid blue line. The blue shaded regions surrounding the regressed fit represents the 95% confidence intervals of the regression. Additionally, the fitted distribution for each axis is displayed as histograms.

Radar animations show that for GFs propagating from the north, the western periphery of these GFs drags along the Colorado Front Range mountains as they approach both instrument sites (figures not shown). This drag might be the reason that the southward-moving GFs are slower (mean propagation speed of 6.6 ± 3.3 m s^{-1}), compared to the other propagation directions

with propagation speeds of 10.1 ± 3.8 m s^{-1}. The differences in observed (theoretical) propagation speed amongst these groups are statistically significantly different at $p < 0.05$ ($p < 0.05$; with and without the inclusion of the pre-frontal cross-front ambient wind component). The prefrontal cross-front ambient wind speed is on average 4.0 m s^{-1} for southward-moving GFs, and 3.7 m s^{-1} for all other propagation directions. However, when we also consider the direction of the ambient wind component in relation to the propagation vector, the prefrontal wind decelerates (accelerates) the southward-moving (non-southward moving) GFs on average by -0.3 m s^{-1} (+2.6 m s^{-1}). Furthermore, at the BAO, all except GFs from the southwest propagate uphill (Fig. 2.7a), but the slope variability is the largest from the north and northwesterly directions (Table 2.3). At the NWTC, GFs approaching from the north, northeast, east, and southeast must travel uphill to reach the study site (Fig. 2.7b) with the highest variability in slope when they propagate from northeast and north (Table 2.3). Because the six slowest GF events approached the BAO and NWTC sites from the north and northwesterly directions, both higher variability in slope and elevation are hypothesized to have contributed to the deceleration of GFs for those size events. Especially considering that the prefrontal cross-front ambient wind component marginally contributes to the deceleration of southward-moving GFs. Conversely, for non-southward moving GFs, perhaps the acceleration due to the prefrontal cross-front ambient wind coupled with encountering less terrain slope variability partially explains the faster propagation speeds from these events.

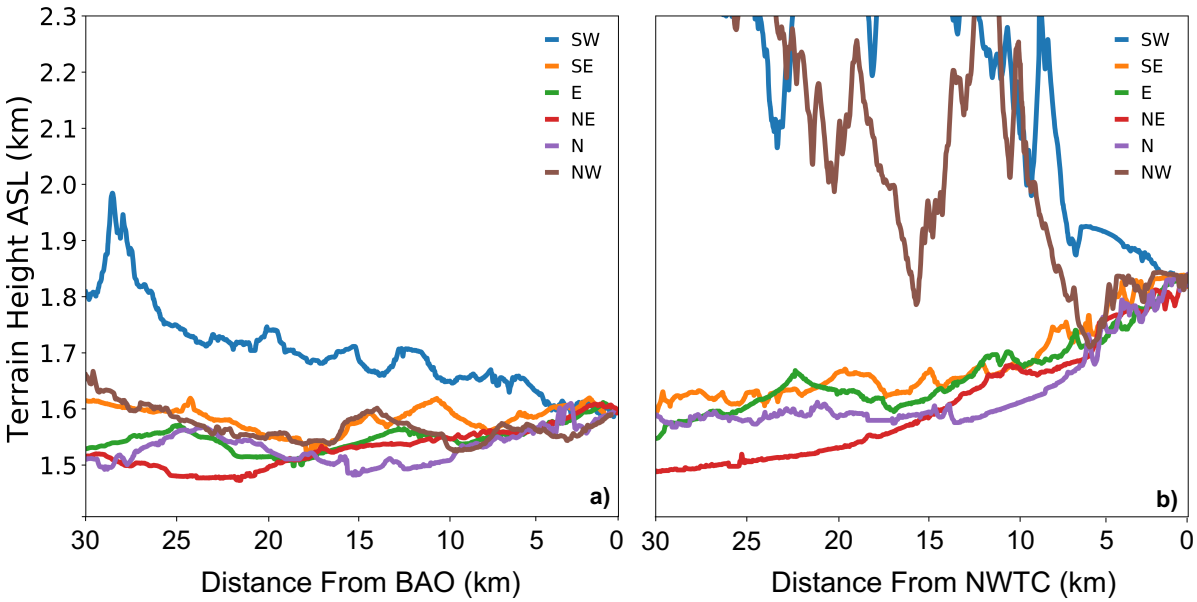

Fig. 2.7: Terrain height Above Sea Level (ASL) (km) along a 30-km path extending from each GF propagation direction at the a) BAO and b) NWTC. Terrain profiles are derived using data from the 1/3 arc-second United States Geological Survey (USGS) National Elevation Dataset (NED).

Table 2.3. Standard deviation of slope (°) and elevation (km) along a 30 km path extending from each GF propagation direction at both study sites. Elevation and slope calculations are based on data from the 1/3 arc-second United States Geological Survey (USGS) National Elevation Dataset (NED).

BAO			**NWTC**		
Direction	**Slope Standard Deviation (°)**	**Elevation Standard Deviation (km)**	**Direction**	**Slope Standard Deviation (°)**	**Elevation Standard Deviation (km)**
SW	2.9	0.07	**SW**	0.2	2.2
SE	9.1	0.02	**SE**	7.6	0.07
E	9.8	0.02	**E**	3.4	0.08
NE	4.0	0.04	**NE**	11.9	0.09
N	18.8	0.03	**N**	24.3	0.08
NW	19.1	0.03	**NW**	0.4	2.7

As the spreading cold air of the GF begins to warm due to mixing and friction as it propagates farther away from the parent thunderstorm, the pressure gradient and surface winds weaken (Cotton et al. 2011). Distance from the parent thunderstorm at the time of passage in combination with the cold pool depth and temperature difference between GF and ambient air can be used to characterize GFs (Goff 1976; Cotton et al. 2011). In our study, the median distance from the parent thunderstorm at time of passage is 38 km across all 24 GF events (Fig. 2.5b). The correlation between distance from parent thunderstorm and maximum wind gusts observed at the 10-m measurement height is negative at -0.32 (not statistically significant) (Fig.

2.8). Adding cold pool depth and temperature difference shows that deeper cold air and larger temperature drops often but not always cause stronger wind gust events, which have a similar distance to their parent thunderstorm. The mean cold air depth during GF passage is 360 m with a maximum cold air depth of 610 m and a minimum of 220 m (Fig. 2.5c). The correlation between cold air depth and the maximum wind gusts near the surface is 0.50 (statistically significant at $p < 0.05$), supporting the theory that deeper cold air can induce stronger horizontal wind gusts (Benjamin 1968; Rotunno et al. 1988; Jorgensen et al. 2003). Similarly, the correlation between cold air depth and the temperature drop near the surface is 0.48 (statistically significant at $p < 0.05$). Furthermore, the theoretical propagation speed (including the pre-frontal ambient wind), which incorporates both cold air depth and temperature deficit, also has a positive yet slightly lower correlation with temperature drop of 0.44 (statistically significant at $p < 0.05$). Both of these correlations suggest that deeper cold air also causes stronger temperature drops near the surface in these 24 GFs. Lastly, the cold air depth across the 24 GFs in this study is positively correlated with both the radar-derived propagation speed ($r = 0.30$) and the theoretical propagation speed (including the pre-frontal ambient wind) ($r = 0.62$), supporting the theory that deeper cold air leads to faster propagating GFs (Benjamin 1968; Rotunno et al. 1988; Jorgensen et al. 2003).

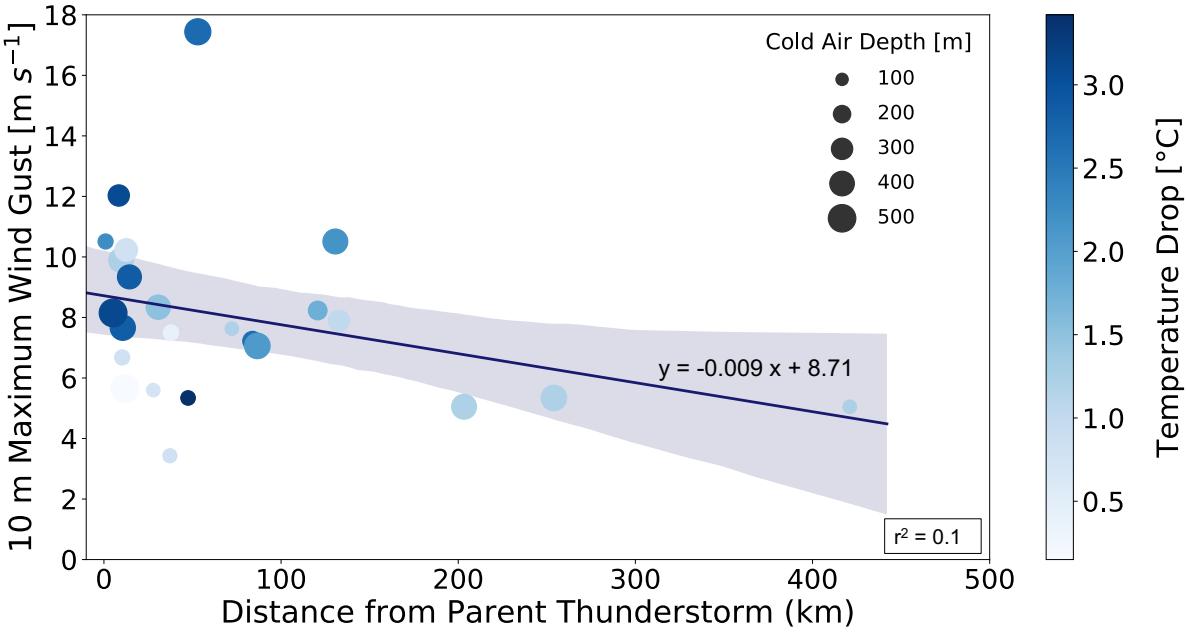

Fig. 2.8: Comparison of maximum wind gusts as the GFs passed over the instrument (m s^{-1}) as a function of distance from parent thunderstorm at time of GF passage (km). Maximum wind gusts are derived by wind anemometers deployed on towers and measured at 10 m above the surface. The variance explained is listed in the lower right corner. Additionally, a linearly regressed fit is plotted as the solid blue line. The grey shaded regions surrounding the regressed fit represents the 95% confidence intervals of the regression. Larger sized data points represent GFs with thicker trailing cold air depths. Darker blue data points represent GFs associated with stronger temperature drops near the surface as they pass over the instruments.

2.5.2 Magnitude and Rate Change During GF Passage

2.5.2.1 Horizontal Wind Speed

The horizontal wind speed is observed by the lidars and tower anemometers to increase during GF passage in all analyzed events. Between the surface and 300 m AGL, the median magnitude change in wind speed with height ranges between 1 to 8 m s^{-1} (black solid line in Fig. 2.9a). Lower magnitude changes < 4 m s^{-1} are observed close to the surface (< 25 m AGL). Above 25 m, median magnitude changes are 4-5 m s^{-1}. A peak in magnitude change of 8 m s^{-1} is observed at 120 m. Four outlier events that extend beyond 1.5 times the interquartile range

observe magnitude change in wind speeds upwards of 6 to 12 m s^{-1}. The duration of the wind speed change during GF passage ranges between 7 to 13 min across all 24 events. The resulting median rate change in wind speed between the surface and 300 m AGL ranges between 0.2 and 0.7 m s^{-1} min^{-1} with nine outlier events where rate changes are > 1.5 m s^{-1} min^{-1} (Fig. 2.9b).

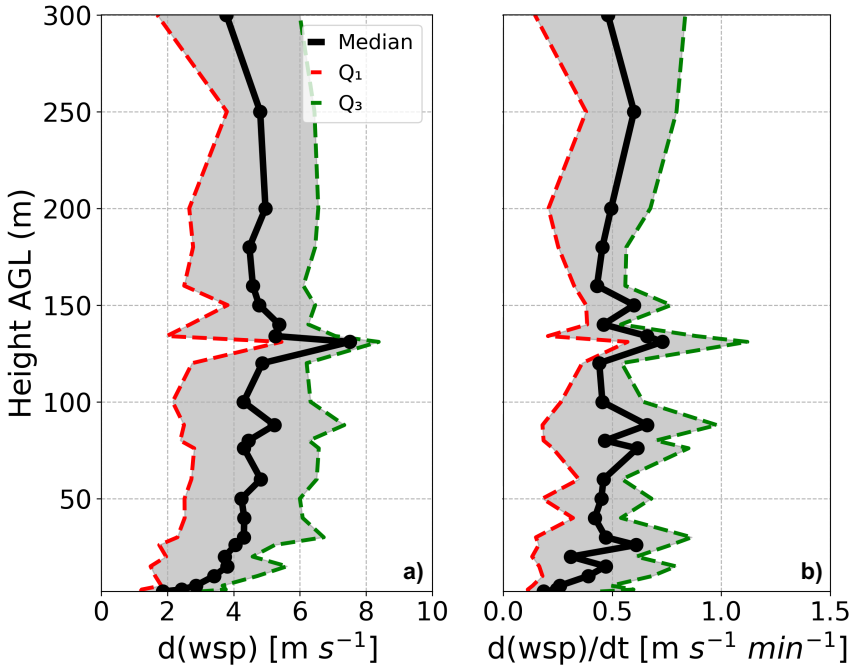

Fig. 2.9: Vertical profiles showing the a) magnitude change (m s^{-1}) and b) rate change (m s^{-1} min^{-1}) of wind speed (wsp) for the 24 events observed by the Windcube lidars and anemometers deployed on towers. The filled gray area represents the interquartile range, with the 25th (Q1) percentile denoted by the dashed red line and 75th (Q3) percentile denoted by the green dashed line. The markers indicate measurement points. The duration of wind speed change ranged from7 to 13 minutes across all 24 events.

We also investigate if the propagation speed of GFs is correlated to the maximum near surface wind gusts (Goff 1976; Mahoney 1988) as these gusts can influence fire spread. When correlating the radar-derived propagation speed to the maximum wind gusts measured at 10 m in this study, the relationship is positive and moderately strong with a correlation of 0.68

(statistically significant at $p < 0.05$) and a R^2 value of 0.46 (Fig. 2.10a). The correlation is slightly lower at 0.61 when correlating the theoretical speed (including the pre-frontal ambient wind) to the maximum observed wind gusts, yet still explains 37 % of the variance in maximum wind gusts near the surface (Fig. 2.10b). Using tower observations from 20 GFs in Oklahoma, Goff (1976) developed an empirical relationship between observed maximum wind gust and GF propagation speed of 1.49. In this study, we find the ratio of maximum wind gusts to radar-derived propagation speed to be 1.18. Mahoney (1988), who studied 30 GFs in the Colorado Front Range, also found a slightly higher ratio of 1.50. Larger ratios observed by Mahoney (1988) and Goff (1976) results primarily from higher mean maximum wind gusts (12.8 m s^{-1} in both Goff (1976) and 14.5 m s^{-1} in Mahoney (1988)).

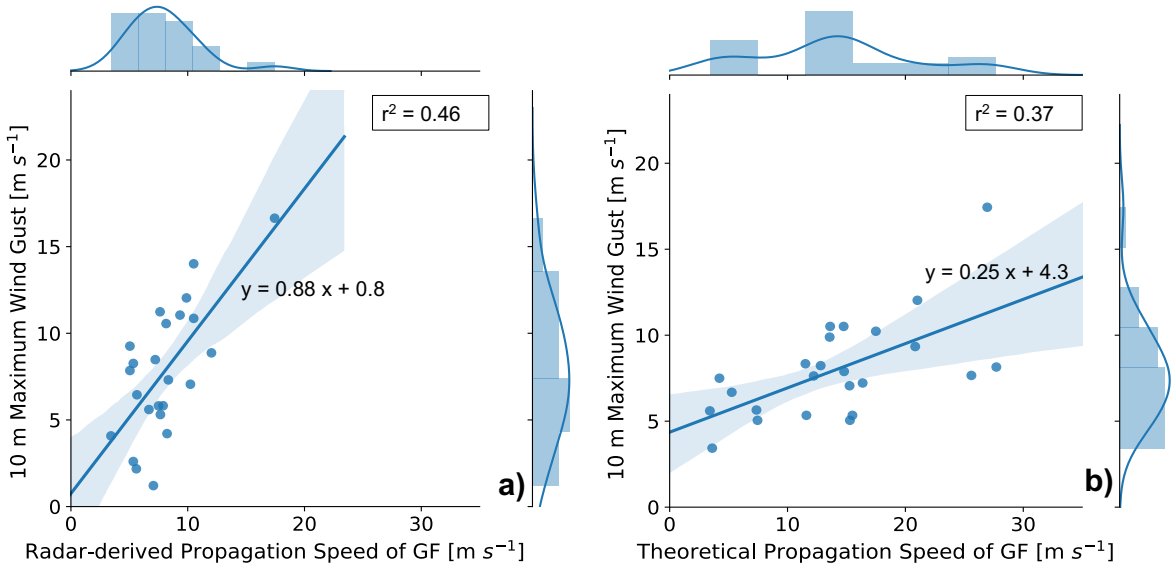

Fig. 2.10: Comparison of maximum wind gusts as the GFs passed over the instrument (m s^{-1}) as a function of propagation speed derived from the radar (m s^{-1}) (a) and from the theoretical density current equation (b) for 24 events. The variance explained is listed in the upper right corners. Additionally, linearly regressed fits are plotted as the solid blue lines. The blue shaded regions surrounding the regressed fits represents the 95% confidence intervals of the regressions. Additionally, the fitted distributions for each axis is displayed as histograms.

2.5.2.2 Wind Direction

Wind direction change associated with GFs is critical, as shown by several documented fire events in which the sudden change in wind direction from a passing GF led to loss of lives and property. Regardless of whether winds back or veer, here the median absolute magnitude change in wind direction ranges between 10 and 60° at all measurement heights observed by the lidars and anemometers (Fig. 2.11a). Similar to horizontal wind speed, the duration for wind direction change ranges between 7 and 16 min across all GF events. The resulting median rate change in wind direction is also nearly uniform in height ranging between 1 and 6° min^{-1} (Fig. 2.11b), suggesting that the rate at which the winds shift directions is mostly uniform through the lowest 300 m AGL. Outlier events are observed at all measurement heights and range from 14 and 36° min^{-1}.

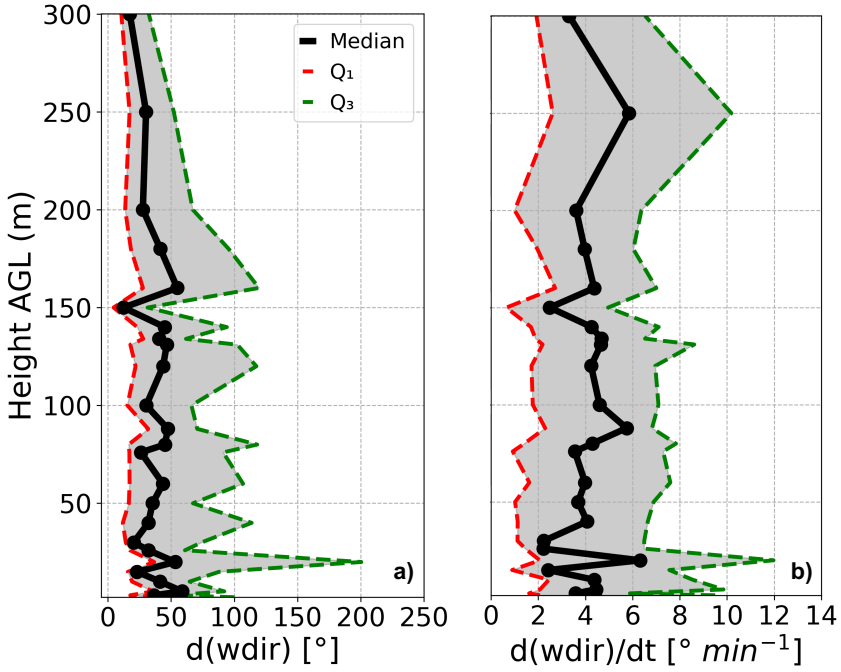

Fig. 2.11: As Fig. 2.9 but showing the a) magnitude change (°) and b) rate change (° min^{-1}) in wind direction (wdir) observed by the lidars and tower anemometers. The duration of wind direction change ranged from 7 to 16 minutes across all 24 events.

2.5.2.3 Vertical Motion

Vertical motion along the leading edge of all analyzed GFs behave as expected with maximum updrafts observed immediately prior to GF passage, followed by a spike in downward motion behind the leading edge of the boundary. Here, the median maximum updraft velocity observed using both the lidars and 3 D sonic anemometers ranges between 0.4 and 2.0 m s^{-1} between 15 and 300 m AGL (Fig. 2.12a), with the median maximum downdraft velocity ranging between -0.3 and -1.2 m s^{-1} (Fig. 2.12b). Six events experience maximum vertical motion > 2 m s^{-1} with a maximum updraft of 3.6 m s^{-1} at 300 m during one event measured.

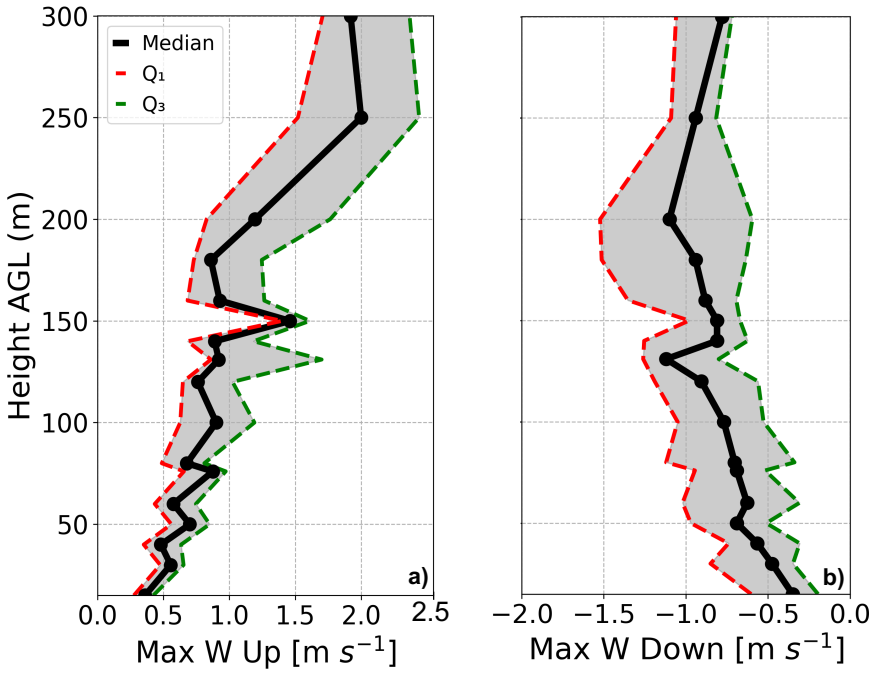

Fig. 2.12: As Fig. 2.9 but showing the a) maximum upward velocity (m s^{-1}) and b) maximum downward velocity (m s^{-1}) observed by the lidars and tower anemometers.

2.5.2.4 Turbulence

Turbulence observed by the lidars and anemometers also behaves as expected by increasing during GF passage for each the analyzed events. Median mean *TI* varies between 0.06 and 0.2 between the surface and 300 m AGL (Fig. 2.13a). Nine events experience maximum *TI* > 0.6 during GF passage (Fig. 2.13b), while *TI* > 0.3 occur during 14 GF events. Median mean *TKE* (gustiness of the 3 D wind) ranges from 0.2 to 1.7 m^2 s^{-2} between 15 and 300 m (Fig. 2.14a). Maximum *TKE* is > 4 m^2 s^{-2} during 14 of the 24 GF events with a maximum of 6.2 m^2 s^{-2} during one event (Fig. 2.14b).

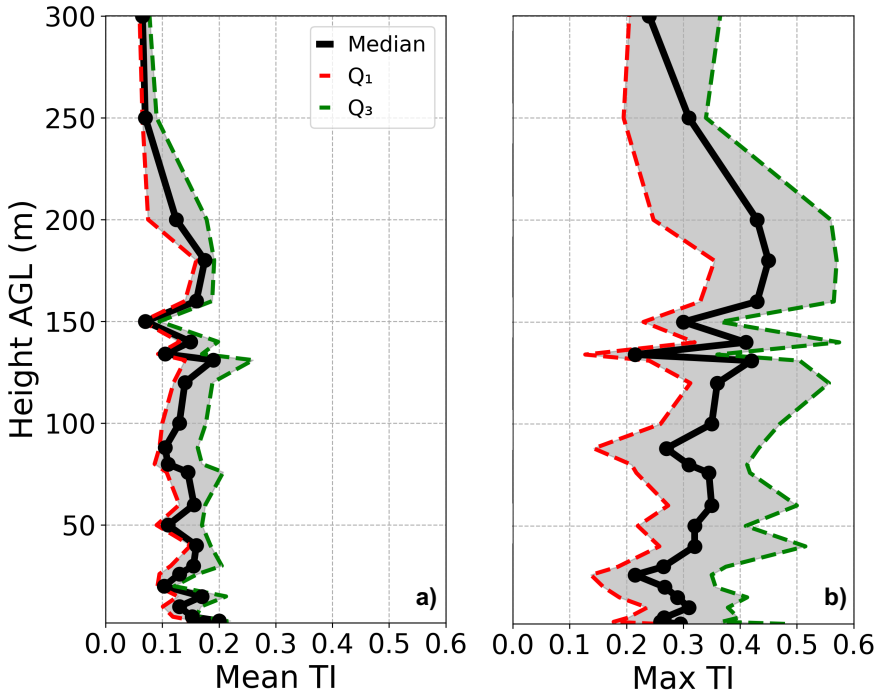

Fig. 2.13: As Fig. 2.9 but showing the a) mean and b) maximum in turbulence intensity (TI) observed by the lidars and tower anemometers.

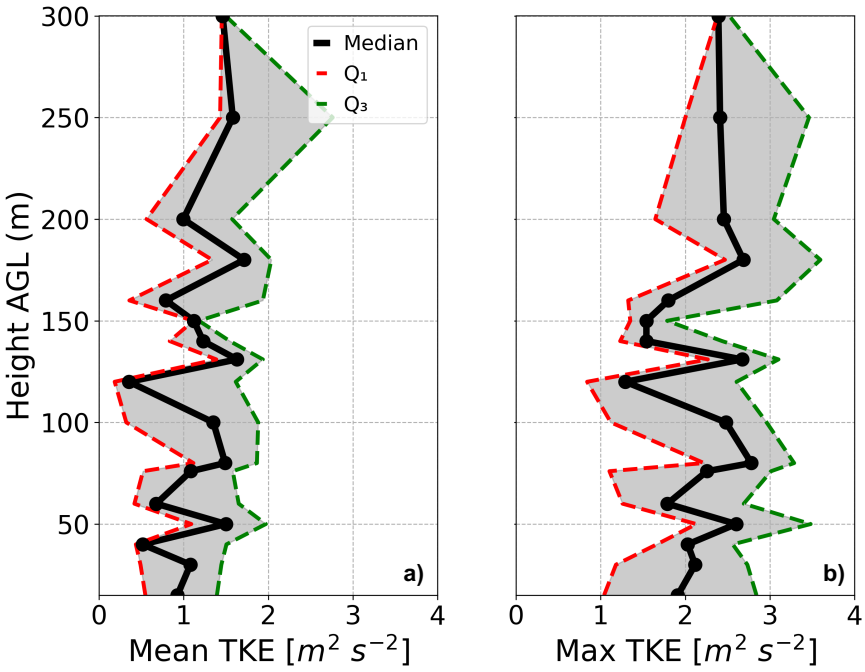

Fig. 2.14: As Fig. 2.9 but showing the a) mean (m^2 s^{-2}) and b) maximum (m^2 s^{-2}) in turbulence kinetic energy (TKE) observed by the lidars and tower anemometers.

2.5.2.5 Temperature

Atmospheric temperature measured by the radiometer and tower probes decreases during passage in all 24 GF events dropping on average by 0.2 to 3°C between 2 and 300 m AGL (Fig. 2.15a) with five outlier events with temperature drops > 6 °C extending beyond 1.5 times the interquartile range. The duration of temperature change ranges between 5 and 10 min across all 24 GFs. The resulting median rate of temperature change does not vary much with height, ranging between -0.04 and -0.3°C min^{-1} from 2 and 300 m AGL (Fig. 2.15b). During nine events rate changes > 0.5 °C min^{-1} are observed.

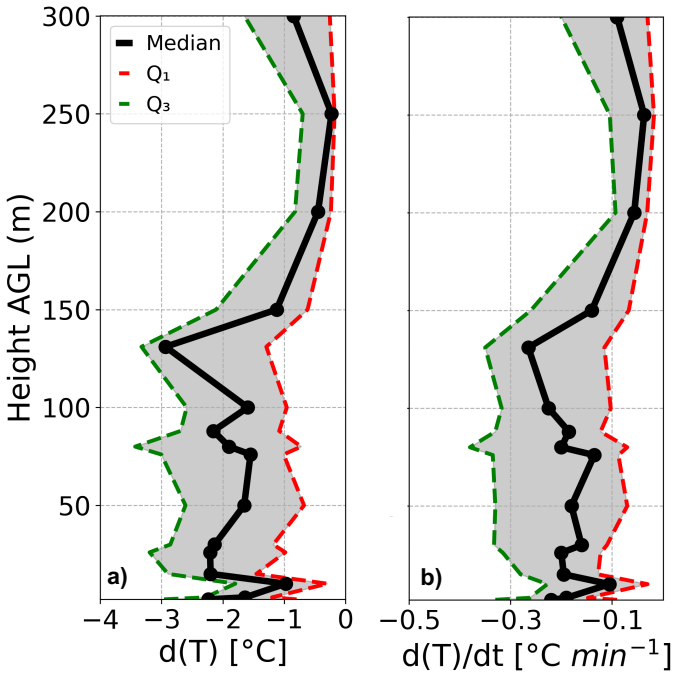

Fig. 2.15: As Fig. 2.9 but showing the a) magnitude change (° C) and b) rate change (° C min^{-1}) in temperature (T) observed by the radiometer and temperature probes on the towers. The duration of temperature change ranged from 5 to 10 minutes across all 24 events.

2.5.2.6 Relative Humidity

Coincident with the decrease in temperature, relative humidity increases during GF passage during all 24 events. Here, median relative humidity measured by the radiometer and tower probes increases by 1 to 8 % between 2 and 300 m AGL as the GFs pass over the instruments (Fig. 2.16a). However, two outlier events at 2 m experience a stronger magnitude increase in relative humidity greater than 30 %. The median duration for relative humidity change is short at 10 min across all 24 GFs. The resulting median rate of change in relative humidity ranges between 0.1 and 0.8 % min^{-1} with little variation with height (Fig. 2.16b). Six outlier events are observed where the rate change is > 3 % min^{-1}.

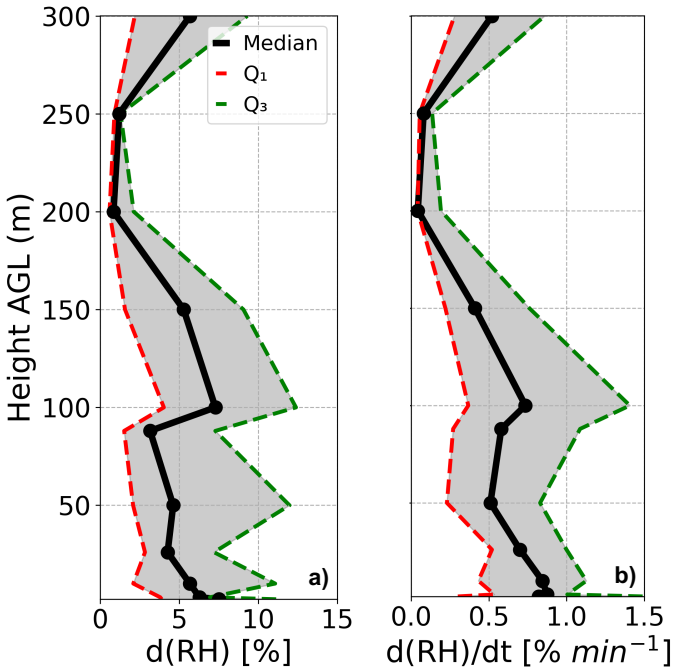

Fig. 2.16: As Fig. 2.9 but showing the a) magnitude change (%) and b) rate change (% min^{-1}) in relative humidity (RH) observed by the radiometer and moisture probes on the towers. The median duration of relative humidity change is 10 min across all 24 events.

2.6 Discussion

2.6.1 Parent Thunderstorm Characteristics

Comparing parent thunderstorm characteristics observed in this study to studies of organized thunderstorms like supercell thunderstorms, squall lines, or MCSs in flatter regions can be challenging considering that there is little uniformity on how to quantify and characterize parent thunderstorms in GF studies. MCS thunderstorms, for example, are characterized by having a region of $Z \geq 40$ dBZ that extends more than 100 km in at least one direction, and with durations between 3 and 24 hours (e.g., Houze 1993; Parker and Johnson 2000; Schumacher and Johnson 2006). Other interpretations require reflectivity of at least 35 dBZ along at least 50 % of the 100-km thunderstorm line to be considered an organized MCS (Provod et al. 2016). Supercell

thunderstorm are usually not characterized by spatial extent but rather having a lifetime of 1-4 h, a weak echo region, a mesocyclone, high lightning flash rate (Moller et al. 1994; Bunkers et al. 2006). Given these inconsistencies and lack of uniformity, here we discuss the general characteristics of the primarily single and multicell thunderstorms in this study.

The median parent thunderstorm duration of 58 min (Fig. 2.4a) across the 24 GF events in this study is typical for single and multicell thunderstorms. Additionally, the median maximum areal extent (within the $Z \geq 35$ dBZ region) of 108 km^2 (Fig. 2.4d) is also indicative of spatially smaller thunderstorms. Rainfall rates and echo top heights in the parent thunderstorms discussed here are also low. The maximum rainfall rate prior to GF detection was on average ~5 mm h^{-1}, with minimum (maximum) rain rates as low (high) as 2 to 3 (6 to 7) mm h^{-1} (Fig. 2.4c), typical of lower-reflectivity thunderstorms. Furthermore, while organized MCS or squall line thunderstorms might feed and maintain GFs for a long time (Wilson and Schreiber 1986; Weisman and Klemp 1986; Engerer et al. 2008), in our study parent thunderstorms disconnected from the GF by either remaining stationary or propagated in opposite directions. Maximum echo tops (median = 9.1 km; Fig. 2.4b) across the 24 GFs in this study are also subdued, however, high convective available potential energy (CAPE) thunderstorms generally have higher echo tops than lower CAPE thunderstorms. Therefore, the low echo top heights observed here may be driven by differing CAPE, rather than thunderstorm type and magnitude.

Organized supercell or linear thunderstorms in the Colorado Front Range are rare, and, therefore, the low rainfall rates, small areal extents, and short durations from the primarily single and multicell parent thunderstorms in this study are representative of the thunderstorms that typically initiate across the mountains in the Colorado Front Range.

2.6.2 Cold Air Depth

Density differences across the GF and the depth of cold air trailing thunderstorm GFs are related to their propagation speed, wind gusts, and associated changes in other atmospheric characteristics near the surface (Benjamin 1968; Goff 1976; Mahoney 1988; Rotunno et al. 1988; Jorgensen et al. 2003). The mean cold air depth of 360 m across the 24 GFs is much shallower compared to studies of GFs from organized convection in flatter regions where cold pools are mainly ~ 0.5-2 km deep but can reach depth of > 4 km in MCSs (Wakimoto 1982; Roux 1988; Bryan 2005; Bryan and Parker 2010; Cotton et al. 2011). Mahoney (1988) also measured an average depth of 1.2 km across 30 GFs observed in the Colorado Front Range, deeper than the cold air measured here.

However, establishing a relationship between cold pool depth and changes in atmospheric characteristics across different studies is often limited to the differences in how and where cold pool depth is determined. Cold air depth is sometimes derived using temperature profiles from *in-situ* measurements (e.g., Wakimoto 1982; Roux 1988; Bryan and Parker 2010), while other methods determine cold pool depth through the kinematic field using Doppler radar data (e.g., Mahoney 1988). Similarly, studies measure the cold pool depth at different GF stages or distances from the parent thunderstorm, as well as determine the depth either through continuous tracking (Lagrangian approach; e.g. Mahoney 1988; Bryan and Parker 2010) or by taking a measurement at a single fixed location in time (Eulerian approach; e.g. Wakimoto 1982; Roux 1988). As we use an Eulerian approach limited to a fixed instrumentation site, we may not capture the deepest cold air associated with the peak intensity of each of the 24 GFs. Instead, we generally characterized weaker, older boundaries that were further away from their parent thunderstorms (median distance = 38 km) and therefore may have already mixed with the

warmer environmental air before passing through the study sites. Similarly, Mahoney (1988) also notes that for the 30 GFs in the Colorado Front Range that they analyzed, it was the older, weaker boundaries that generally had shallower cold air depths.

2.6.3 Horizontal Wind Speed

Wind dynamics associated with passing GFs can rapidly change fire behavior which can limit response effectiveness and most importantly threaten firefighter lives (Joint Fire Science Program 2017). During the 2013 Arizona Yarnell Fire GF accident, for example, the nearest surface meteorological station measured GF wind speed change in the 13 to 17 m s^{-1} range during the GF interaction with the fire (Karels and Dudley 2013). Additionally, during the Florida Ransom Road Fire in 1981, GF-induced wind speed change of 3 to 10 m s^{-1} and maximum wind gusts as high as 23 m s^{-1} were measured at a nearby meteorological tower during the period when two individuals were engulfed by the fire (Haines 1988). The magnitude wind speed changes of 1 - 8 m s^{-1} (with outliers of 6 -12 m s^{-1}, and maximum wind gusts as high as 17.4 m s^{-1}) observed along the Colorado Front Range are comparable to those observed during those fires.

Although the median magnitude change in horizontal winds appear to vary little with height, a low-level jet like profile (or "GF nose –shape" profile) is observed to peak near 120 m AGL (Fig. 2.9a). Similar low-level jet like structures and maximum horizontal winds near 120 m have been observed and modeled in other GF studies (Hjelmfelt 1988; Bowen 1996; Kwon and Kareem 2009; Kwon et al. 2012). Considering that typical tower heights for utility wind turbines range between 45 – 105 m (AWEA 2008; Kwon et al. 2012), low- to mid-rise structures would

potentially be exposed to the maximum median change in horizontal winds observed across the GFs in this study.

Mean rate change in wind speed of 0.2 to 0.7 m s^{-1} min^{-1} (with rate changes > 1.5 m s^{-1} min^{-1} for individual cases) observed along the Colorado Front Range are also lower compared to other studies. Zhang et al. (2018) observe a wind speed rate change of 1.5 to 2 m s^{-1} min^{-1} over 10 minutes in 88 (63%) of 141 GFs that are detected along the coastal plains of the Northern Mediterranean coast. They observe wind speed rate changes from 2 to 3.5 m s^{-1} min^{-1} during the remaining 53 (37%) GF events.

The mean maximum horizontal wind gusts observed near the surface in this study is 7.9 m s^{-1}, weaker than what is typically associated with GFs that initiate from organized convection in flatter terrain. For example, mean maximum wind gusts of 15 m s^{-1} are associated with 39 GFs that initiated from organized MCSs in Oklahoma (Engerer et al. 2008). Since most of the GF events in this study originate from single and multicell thunderstorms, the difference in organization and downdraft strength (i.e., depth of cold air at time of passage) may explain the weaker mean maximum wind gusts observed in this study. However, Mahoney (1988) observed mean maximum wind gusts of 12 to 14 m s^{-1} along 30 GFs in the Colorado Front Range with several events occurring near the BAO tower. Therefore, GF-induced maximum wind gusts in this region can most definitely exceed the gusts associated with the GFs in this study.

2.6.4 Wind Direction

While many studies emphasize the important role of wind direction change on fire behavior and intensity (Surveys and Investigation Staff 1981; Haines 1988; Goens and Andrews 1998; Kern et al. 2004; Johnson et al. 2014; Sharples et al. 2017), only few quantify change in wind

direction associated with GF passages. During the 2013 Arizona Yarnell Hill Fire GF accident, the wind direction shifted 90° during the GF passage, which undermined the decision-making of the firefighters (Karels and Dudley 2013). While thermodynamic variables like temperature change are weaker along the Colorado Front Range, the magnitude of wind direction ranges is still significant between 10 and 60° in our study, strong enough to significantly re-direct fire behavior (Surveys and Investigation Staff 1981; Goens and Andrews 1998; Kern et al. 2004; Karels and Dudley 2013; Johnson et al. 2014).

2.6.5 Vertical Motion

Understanding the location and strength of both the updraft and downdraft velocities associated with the leading edge of GFs is important for the landing and takeoff of airplanes (Federal Aviation Administration 1988, 2008, 2013; O'Connor and Kearney 2019). Vertical motion along the leading edge of GFs from organized severe supercell and MCS thunderstorms often exceeds 6 m s^{-1} and, in extreme cases, can reach upwards of 15 m s^{-1} (Charba 1974; Goff 1976; Wakimoto 1982; Martner 1997; Bryan and Parker 2010). GFs discussed in this study mainly observed weaker vertical velocities with maximum vertical motion in the 2 – 3.6 m s^{-1} range.

The weaker vertical motion observed across the GFs in this study may be related to the shallow cold air (mean depth = 360 m) measured on average about 38 km from the parent thunderstorm (see section 2.6.2). Similar mean cold air depths (~330 m) and maximum updrafts (between 1.1 and 3.1 m s^{-1}) are observed across 25 GFs from non-severe, shallow convective systems in Wilbanks et al. (2015). In contrast, deeper cold air is present in many studies that feature stronger vertical motion along GFs from severe supercell and MCS thunderstorms

(Charba 1974; Goff 1976; Wakimoto 1982; Bryan and Parker 2010). Similarly, Mahoney (1988) who tracked the evolution of two colliding GFs (with cold air depths of ~1.5 to 2 km) in the Colorado Front Range measured updrafts in the 3 to 9 m s^{-1} range. Therefore, observing stronger vertical motion along GFs in the Colorado Front Range is possible, especially if measurements are taken during the time when the deepest cold air is present. Here, however, the average cold air depth at time of GF passage is shallow, perhaps explaining the relatively weak maximum updrafts.

2.6.6 Turbulence

The mean *TI* during GF passage observed in this study is similar to other studies that focus on GF loading effects on wind energy structures. For example, the mean *TI* observed during 144 GF events along the northern Mediterranean coastline ranged from 0.08 to 0.18 (Zhang et al. 2018), similar to the 0.06 to 0.20 *TI* range observed in this study. High turbulent environments ($TI > 0.3$; $TKE > 4$ m^2 s^{-2}) have been linked to increased wear on wind turbines and an increase in operation and maintenance costs (Manwell et al. 2002; TC88-MT, I. E. C. 2005; Nguyen et al. 2011; Hadi et al. 2015; Lu et al. 2019). Considering that we observe short duration spikes in maximum *TI* and *TKE* exceeding > 0.3 and > 4 m^2 s^{-2}, respectively, turbulence induced by the GF events along the Colorado Front Range could be strong enough to potentially negatively influence wind energy structures (Manwell et al. 2002; Hadi et al. 2015; Zhang et al. 2018). *TI* values between 0.1 and 0.2, and *TKE* values around 2 m^2 s^{-2} are typically associated with the convective boundary layer (Stull 1988; Kumer et al. 2016). Short duration spikes in *TI* and *TKE* during the passage of these GF events also often exceeded the turbulence associated with general buoyancy during unstable boundary layer conditions.

2.6.7 Temperature

Rapid shifts in temperature and moisture content associated with GF passage can also heavily influence fire behavior and spread near the surface (Hanley et al. 2013; Coen and Schroeder 2017; Coen et al. 2018). Cooler temperatures and increased moisture content from passing boundaries are associated with diminishing fire growth and intensity. For example, a decrease in fire intensity was observed during the 2004 East Fork Fire near Tallahassee, Florida, as a sea breeze boundary interacted with the fire and filtered in cooler, moist ocean air (Hanley et al. 2013). A period of slowed fire growth during the 2014 California King Fire was also observed and partly attributed to an increase in atmospheric humidity (Coen et al. 2018).

Temperature decreases observed in our study (0.2 - 3 °C with up to 6 °C) are again subdued compared to other studies. Temperature drops between 1.8 and 13.1°C are observed at the surface from 38 GFs in Niger, Africa, that initiated from organized MCSs (Provod et al. 2016). Similarly, temperature drops beyond 10°C was observed for most of 39 GF events that spawned from MCS events in Oklahoma, with a maximum drop of 17.1°C (Engerer et al. 2008). The shallow cold air (mean depth = 360 m) measured at time of passage across the 24 GFs in this study may partially explain the weaker temperature drops observed here compared to the MCS initiated GFs studied in Provod et al. (2016) and Engerer et al. (2008). However, direct comparisons with Provod et al. (2016) and Engerer et al. (2008) is difficult considering their methods used to calculate temperature deficits differed from this study in that they subtract the maximum temperature before the GF from the minimum after the GF, as opposed to using an averaging technique like the one applied here. Therefore, conclusions drawn from comparing

temperature deficits from the mostly single and multicell thunderstorm GFs in this study to the MCS initiated GFs in those studies is somewhat limited.

2.6.8 Relative Humidity

To put the magnitude changes of relative humidity of 1 to 8 % observed along the Colorado Front Range in perspective, an increase in relative humidity of ~20% was observed over a period of slowed fire growth during the 2014 California King megafire (Coen et al. 2018). Likely, then, the increase in relative humidity observed during the 24 GF events in this study would not contribute to the diminished fire intensity. The increase in wind gusts associated with GF passage would most likely overshadow any diminishing effects from the drop in temperature and rise in moisture content.

2.7 Conclusions

Knowledge of GF propagation and atmospheric characteristics predominantly stems from studies of organized and severe supercell or MCS thunderstorms that develop in flatter terrain regions. This study focuses on GFs from mainly single and multicell thunderstorms in and near complex terrain in the Colorado Front Range, east of the Rocky Mountains. In this study, in-situ and remote sensing observations are combined to quantify the magnitude and rate change of atmospheric variables that occur in 24 GF events. Horizontal wind, turbulence (*TI* and *TKE*), vertical velocity, temperature, and humidity are analyzed in the lowest 300 m AGL using a remote-sensing microwave radiometer, wind-profiling lidars, and *in-situ* data from three meteorological towers. The main findings from this analysis are:

- The median radar-derived propagation speed was 7.6 m s^{-1} with a maximum of 16.6 m s^{-1}, and the influence of the pre-frontal cross-front ambient wind component on propagation speed was found to be negligible. However, GFs that encountered higher variability in terrain and slope (from the northerly directions) were on average slower (6.6 ± 3.3 m s^{-1}), compared to the other propagation directions (10.1 ± 3.8 m s^{-1}). Variability in terrain slope and elevation influenced the propagation speed of GFs in this study.
- Magnitude changes in temperature (0.2 to 3 °C), maximum vertical velocities (2 – 3.6 m s^{-1}), and maximum wind gusts (mean = 7.9 m s^{-1}) observed here are generally weaker compared to studies of GFs initiating from organized, severe thunderstorms in flatter terrain. The average cold air depth is about 360 m, shallower compared to other studies, which may explain the weaker magnitude changes observed in this study.
- While most wind energy GF studies focus on quantifying turbulence using 2 D *TI,* this is one of the first studies that also evaluates the 3 D *TKE* associated with GFs. Short duration spikes in *TKE* (> 4 m^2 s^2) occur in 14 (58 %) of the 24 GF events, exceeding *TKE* values often associated with unstable boundary layer conditions.

Comparing GF characteristics amongst different types of thunderstorms and in different terrain is often challenging considering that methods and instruments used in GF studies are not always uniform. In particular, calculating the change in GF atmospheric characteristics is highly dependent on the interpretation of when the boundary passed over the instruments. A more uniform understanding of how to quantify the GF passage time would help to better facilitate regional comparisons. A future observational study could, therefore, address the influence of terrain on propagating GFs by comparing the magnitude change in GF boundary variables in this

study, to the magnitude change in GF boundary variables from single or multicell thunderstorms in flatter terrain using similar methods and instruments. A future study should also expand this analysis to surface stations scattered across the Intermountain West. Statistically examining many more GF events in the complex terrain of this region would ideally further our understanding of how the underlying terrain may influence propagating GFs. The additional statistics could also help to validate numerical weather prediction models, which in the past have shown promise in their ability to accurately model GFs and other high-impact wind events in mountainous terrain (Coen and Riggan 2011; Coen et al. 2013; Johnson et al. 2014; Coen et al. 2017; Coen et al. 2018; Jiménez et al. 2018; Muñoz-Esparza et al. 2018).

2.8 Acknowledgement

This research is supported through an award L17AC00227 ("JFSP Project 17-1-05-2 Evaluating thunderstorm outflow boundaries in WRF-Fire") from the Bureau of Land Management as part of the Joint Fire Science Program under the subject opportunity FA-FON0017-0002. This work was authored in part by the National Renewable Energy Laboratory, operated by Alliance for Sustainable Energy, LLC, for the U.S. Department of Energy (DOE) under Contract No. DE-AC36-08GO28308. Funding provided by the U.S. Department of Energy Office of Energy Efficiency and Renewable Energy Wind Energy Technologies Office. The views expressed in the article do not necessarily represent the views of the DOE or the U.S. Government. The U.S. Government retains and the publisher, by accepting the article for publication, acknowledges that the U.S. Government retains a nonexclusive, paid-up, irrevocable, worldwide license to publish or reproduce the published form of this work, or allow others to do so, for U.S. Government purposes. The authors would like to acknowledge and

thank the reviewers of this manuscript whose suggestions strengthened the fundamentals of this article.

3 Evaluating Thunderstorm Gust Fronts in New Mexico and Arizona

This chapter is adapted and reformatted from:

Luchetti, N. T., K. Friedrich, and C. E. Rodell, Evaluating Thunderstorm Gust Fronts in New Mexico and Arizona. *Mon. Wea. Rev.*, doi: https://doi.org/10.1175/MWR-D-20-0204.1.

3.1 Abstract

Strong winds generated by thunderstorm GFs can cause sudden changes in fire behavior and threaten the safety of wildland firefighters. Wildfires in complex terrain are particularly vulnerable as GFs can be channeled and enhanced by local topography. Despite this, knowledge of GF characteristics primarily stems from studies of well-organized thunderstorms in flatter areas such as the Great Plains, where the modification of GFs by topography is less likely. Here, we broaden the investigation of GFs in complex terrain by statistically comparing characteristics of GFs that are pushed uphill and propagate atop the Mogollon Rim in Arizona to those that propagate down into and along the Rio Grande Valley in New Mexico. Using operational WSR-88D radars and in-situ observations from Automated Surface Observing System (ASOS) stations, 122 GFs in these regions are assessed to quantify changes in temperature, wind, relative humidity, and propagation speed as they pass over the weather stations. GFs that propagated down into and along the Rio Grande Valley in New Mexico were generally associated with faster propagation speeds, larger decreases in temperature, and larger increases in wind speeds compared to GFs that reached the crest of the Mogollon Rim in Arizona. GFs atop the Mogollon Rim in Arizona behaved less in accordance with density current theory compared to those in the Rio Grande Valley in New Mexico. The potential reasons for these results, and their implications for our understanding of terrain influence on GF characteristics, are discussed.

3.2 Introduction

Rapid changes in wind direction and speed from passing thunderstorm GFs can threaten the safety of wildland firefighters by redirecting fire spread towards locations that were previously considered safe. In the past, studies of GF characteristics have primarily focused on severe thunderstorms in flatter areas such as the United States Great Plains region (e.g., Charba 1974; Goff 1976; Engerer 2008; Bryan and Parker 2010). However, little observational work has investigated the characteristics of GFs in complex terrain where thunderstorm outflow winds can be channeled and enhanced by local terrain features (Wakimoto et al. 1994; Goens and Andrews 1998; Sharples et al. 2017; Luchetti et al. 2020). Given that several dangerous fires occur in mountainous regions around the world each convective season, here we explore how GFs evolve and interact with local terrain in two complex terrain regions. Specifically, we statistically analyze the propagation and atmospheric characteristics (wind, temperature, moisture) of 122 GFs observed by in-situ surface instruments in the complex terrain of New Mexico (NM) and Arizona (AZ) with the goal of exploring if variability in GF characteristics can be linked to the underlying terrain.

GFs are considered density currents with dense cold air propagating into an environment characterized by less dense and warmer air (e.g., Charba 1974; Sasaki and Baxter 1986; Friedrich et al. 2005). When thunderstorm GFs pass over a meteorological station, the station typically records an increase in wind speed, a rapid wind direction shift, a drop in temperature, and an increase in moisture content (Simpson 1969; Charba 1974; Goff 1976; Fujita 1981; Droegemeier and Wilhelmson 1987; Lompar et al. 2018; Luchetti et al. 2020). While temperature drop and moisture rise can act to diminish fire intensity (Hanley et al. 2013; Coen and Schroeder 2017; Coen et al. 2018), the ramp up of winds and directional shifts associated

with GF passage mostly overshadows these diminishing effects, and instead typically lead to rapid enhancement of fire intensity and spread. Several studies and accident reports emphasize GF-induced wind direction change as the main catalyst for rapid fire intensification during accidents where individuals became entrapped and lost their lives (Surveys and Investigation Staff 1981; Haines 1988; Goens and Andrews 1998; Kern et al. 2004). Similarly, GF-induced fire accidents and structural damage have occurred in areas of complex terrain where monitoring and tracking of thunderstorms can be more difficult (Karels and Dudley 2013; Johnson et al. 2014; Hardy and Comfort 2015; Paez et al. 2015). For example, during the destructive 2012 Colorado Waldo Canyon Fire multiple GFs rapidly shifted the direction of the fire spread towards a local neighborhood (Johnson et al. 2014). These wind shifts can also re-direct fire spread towards topographic features favorable for fire growth such as canyons (Goens and Andrews 1998; Sharples et al. 2017). Considering the potential safety hazards associated with gust-front-induced fire spread in mountainous areas, it is essential for the fire weather community to understand how GFs evolve in these regions (Joint Fire Science Program 2017).

Our traditional understanding of GF characteristics mostly stems from observational and numerical studies of GFs that initiate from severe thunderstorms such as mesoscale convective systems (MCSs) and supercell thunderstorms (e.g., Charba 1974; Goff 1976; Engerer et al. 2008; Bryan and Parker 2010), both of which tend to require flatter terrain to develop (Bunkers et al. 2006; Keighton et al. 2007; Parker and Ahijevych 2007; Schneider 2009; Ashely et al. 2019). While cases of MCS and supercell thunderstorms have been observed in areas of complex terrain in the past (LaPenta et al. 2005; Bosart et al. 2006; Schneider 2009), most thunderstorms that initiate across mountains typically remain as single or multicell thunderstorms until they can propagate into flatter regions (Cotton et al. 1983; McAnelly and Cotton 1986; Tucker and Crook

1999). This may be related to reduced temperatures, low-level moisture, and surface-based instability typically observed at higher elevations compared to lower elevations (Bunkers et al. 2006; Keighton et al. 2007; Schneider 2009). Despite this, single and multicell mountain thunderstorms can undoubtedly still produce gusty outflow boundaries with surface wind gusts strong enough to significantly alter fire behavior (Goens and Andrews 1998; Luchetti et al. 2020), and, therefore, need to be further evaluated.

Given the lack of focus on GFs in complex terrain regions throughout the literature, in this paper we broaden the investigation of GF characteristics to those that evolve in the complex terrain of NM and AZ. The mountains of NM and AZ are ideal study regions as orographic thunderstorms frequently initiate during the North American Monsoon season between June and August (Adams and Comrie 1997). The chosen study areas also allow for the comparison of GFs that propagate across two differing terrain features commonly found in complex terrain regions: i) up and over a ridgeline and ii) down into a valley. To quantify GF characteristics in these regions, we use the operational Weather Surveillance Radar 88 Doppler (WSR-88D) radars in Albuquerque, NM and Flagstaff, AZ and Automated Surface Observing System (ASOS) weather stations.

The study is organized as follows: Section 3.3 discusses the datasets and methods used including location, instrumentation, and local physiography for each of the two study regions. Results and comparisons between the study regions are presented in Section 3.4. The potential role of topography on GF characteristics is discussed in Section 3.5. Conclusions and suggestions for future work are discussed in Section 3.6.

3.3 Study Sites, Instrumentation, and Analysis Methods

3.3.1 Description of the Study Sites and the WSR-88D Radars

To study GF characteristics in complex terrain, we choose two study sites near Albuquerque, NM, and Flagstaff, AZ (Fig. 3.1). These study sites are chosen based on the following criteria. Each site needs to i) be located in complex terrain, ii) have a convective season, iii) experience wildfires during the convective season, iv) be within 80 km range of an operational WSR-88D radar, and v) have at least one ASOS station within the 80 km radar range.

The two WSR-88D radars used to identify and track GFs are the Albuquerque, NM, radar (referred to as KABX hereafter; Fig. 3.1a) and the Flagstaff, AZ, radar (referred to as KFSX hereafter; Fig. 3.1b). KABX is located 20 km northwest of Albuquerque at 1.8 km MSL in the Rio Grande Valley between the NM West Central Highlands and Mountains to the west and the Sandia Mountains to the east (Fig 3.1a). Thunderstorms that impact the Albuquerque region often originate from the West Central Mountains further west or the Sandia Mountains to the east. Within the 80 km range, the KABX radar beam at the lowest elevation angle of 0.47° experiences no beam blockage to the southeast and throughout the surrounding Rio Grande Valley at the radar (Shipley et al. 2009). However, along the crest and to the east of the north-south oriented Sandia Mountains, the KABX radar beam experiences 50-100% beam blockage. Additionally, the KABX radar beam experiences 20-50 % beam blockage towards the west and over the West Central Highlands and Mountains region. Therefore, identifying and tracking GFs east of the Sandia Mountains and over the West Central Highlands region is more challenging compared to those that occur in the Rio Grande Valley.

KFSX is located about 79 km southeast of Flagstaff at 2.3 km MSL atop the Mogollon Rim (Fig. 3.1b), which favors convection initiation in the afternoon during the convective season (Adams and Comrie 1997; Goens and Andrews 1998). Within the 80 km range, the KFSX radar beam at the lowest radar elevation angle of 0.47° experiences roughly 20-30% beam blockage to the northwest towards Humphreys Peak (Fig. 3.1b), and directly south to the edge of Mogollon Rim (Shipley et al. 2009). However, the KFSX radar beam experiences no beam blockage along the remainder of the Mogollon Rim to the east and west. Therefore, from a beam blockage perspective, identifying and tracking GFs on the east and west edge of the Mogollon Rim is less challenging than for those GFs that develop to the north near Humphreys Peak. Since the KFSX radar is located on top of the Rim, lower terrain to the east and west is ~1 – 1.5 km below the radar. GFs originating in the lower terrain might not be captured by the lowest 0.47° radar scan until they move up to the Rim.

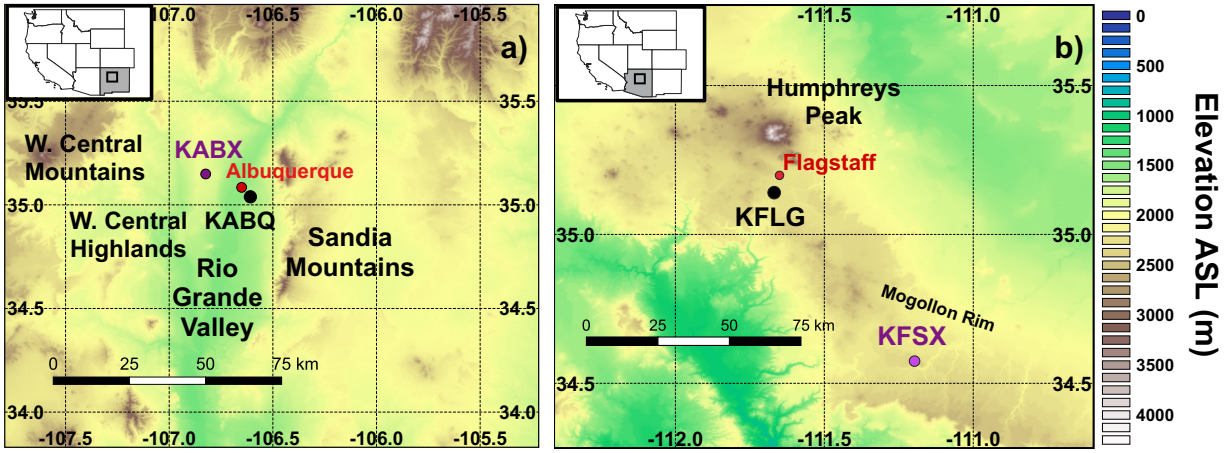

Fig. 3.1: Topographic maps showing the a) New Mexico and b) Arizona study regions. The location of the Albuquerque (KABQ) and Flagstaff (KFLG) ASOS stations are highlighted as the black dots. NWS Albuquerque (KABX) and the NWS Flagstaff (KFSX) NEXRAD radar sites are highlighted as the purple dots. Topographic features discussed in the text are highlighted.

3.3.2 Description of Automated Surface Observing System Instrumentation

Surface data from the ASOS weather stations are used to assess the change in horizontal wind speed and direction, temperature, and relative humidity during GF passage. ASOS stations provide high-resolution measurements of basic weather elements that undergo multiple levels of quality control (Nadolski 1998). Wind speed and direction is measured at 10 m AGL using a sonic anemometer every 1 s from which a 3 s running mean is computed producing a "3 s peak" (NWS 2008). A running 2-min average is then computed across 24 discrete 5 s samples. The value of the 2-min averaged peak wind speed consists of the "3 s peak" from the 5 s sample which contains the highest "3 s peak" wind speed (NWS 2008). Wind gusts are also measured and updated every 3 s. The accuracy for wind direction is ± 3° for winds greater than 2.5 m s^{-1}, and the accuracy for wind speed is ± 1 m s^{-1}. The ambient dry-bulb and dewpoint temperatures are measured using a HO-83 hygrothermometer every 10 s and averaged to 1-min intervals. 5-min averages of the 1-min averaged intervals are then reported every 1-min. Accuracies for temperature and dewpoint temperature measurements are within ± 1°C and ± 3°C, respectively. Here, we utilize 1-min averages of wind, temperature, and relative humidity to evaluate GF events in these study regions.

The New Mexico ASOS station (KABQ) is located at 1.6 km MSL just downslope of the Sandia Mountains in the Rio Grande Valley about 23 km southeast of the operational radar KABX (Fig. 3.1a). Considering the height difference between the radar and the ASOS station, the center of the lowest radar beam at 0.47° elevation is about 0.2 km above the KABQ station.

The Arizona ASOS station (KFLG) is located at 2.1 km MSL on the Mogollon Rim just south of Humphreys Peak (Fig. 3.1b) and about 76 km northwest of the operational radar

KFSX. Considering the height difference between the radar and the ASOS station, the center of the lowest radar beam at 0.47° elevation is about 0.9 km above the KFLG station.

3.3.3 GF Detection and Tracking Method and Categorizing

To quantify changes in wind, temperature, and moisture associated with a GF, we first need to identify the times when a GF passes over one of the ASOS stations. To do that, we identify days during the 2010 to 2018 monsoonal seasons (June-August) when thunderstorms develop in close proximity to the ASOS stations using Level II radar reflectivity at the lowest level at 0.47° elevation every 5 min from the operational WSR-88D radars. From those days, we isolate the days where lines of reflectivities of 5 - 25 dBZ (also radar fine lines) propagate away from a parent thunderstorm and pass through the ASOS station (Fig. 3.2). Identifying thunderstorm GFs via the radar fine lines is a widely accepted method (Wilson and Schreiber 1986; Koch and Ray 1996; Luchetti et al. 2020). Tracking of radar fine lines is used to determine (i) the time when GFs pass over the ASOS stations and (ii) GF propagation speed and direction between the time of first detection and passage through the station (Fig. 3.2). GF propagation speed is determined by calculating the displacement of the radar-detected fine lines over time as they approach and pass over the ASOS stations. Since radar fine lines tend to morph into irregular shapes, we account for this by determining an approximately 10-km mean positional swath across the leading edge of the boundary as it moves over the ASOS stations. The swath displacement is then tracked backward to calculate the mean propagation speed between the time the fine line is first detected and the time it passes over the ASOS stations. Level II radar reflectivity is also used to categorize parent thunderstorms as single-cell, multicell, quasi-linear, or supercell thunderstorms following Smith et al. (2012).

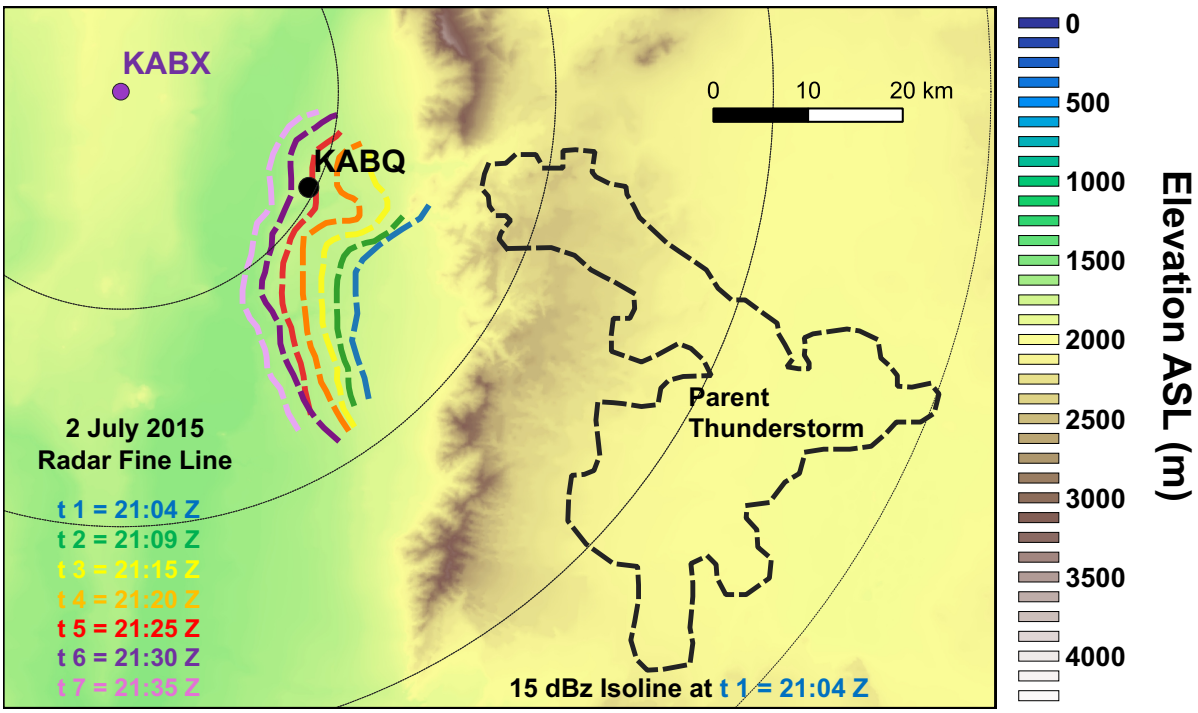

Fig. 3.2: Topographic map with the time-series of the position of a radar fine line that passed over the KABQ ASOS site (black dot) on 2 July 2015 observed by the KABX operational radar (purple dot) at Albuquerque, New Mexico. Radar reflectivity at 0.47° radar elevation angle approximately every 5 minutes is used to track the movement of the 5 - 25 dBZ radar fine line from the time it first appears (t1) until it passes the KABQ ASOS station (t7). The 15-dBZ isoline of the parent thunderstorm at t1 is outlined (dashed black line). KABX radar range rings at 25 km intervals are displayed as thin black lines with the radar site at the center.

3.3.4 Magnitude Change Calculation

Once we determine the time when each radar-indicated GF passes over the ASOS stations, we then quantify the change in wind speed and direction, temperature, and relative humidity during that time (referred to as the magnitude change and described in more detail in Luchetti et al. 2020). In-situ 1-min ASOS data are analyzed 30 min prior-to and 30 min after the radar-indicated GF passage time (Fig. 3.3). During this timeframe we identify the time when the largest gradient in each atmospheric variable occurs (yellow box in Fig. 3.3, referred to as the GF

Passage Period or GPP; Luchetti et al. 2020). We then quantify the magnitude change in each atmospheric variable by taking the difference between the 5-min mean of the variable prior-to and after the GPP (green boxes in Fig. 3.3). The magnitude change is analyzed for each atmospheric variable across all GF events in each of the two study areas.

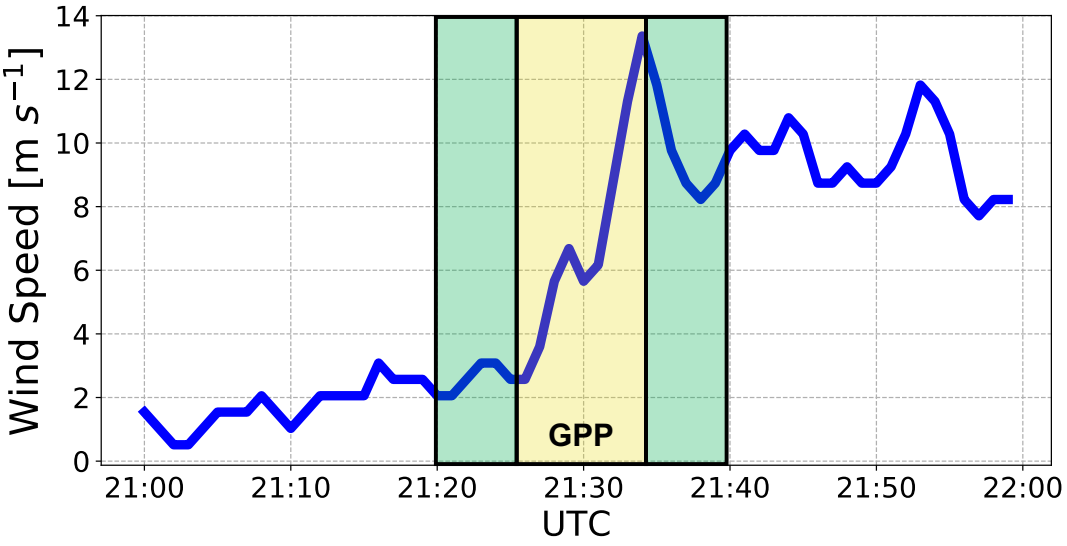

Fig. 3.3: Temporal evolution of horizontal wind speed (m s^{-1}) during a GF passage on 2 July 2015 over the KABQ ASOS site. White area indicates the time 30 minutes prior to, and 30 minutes after the radar-derived GF passage time. The yellow highlighted box represents the GF Passage Period (GPP). The green highlighted areas represent the 5-min intervals where the variable is averaged in order to calculate the difference in the variable prior to and after the GPP.

3.3.5 GF Area Clustering

In order to determine the role of the underlying terrain on GF characteristics, we first group radar fine lines based on where they are first observed and from which direction they approach the ASOS station. To do this, we digitize the entire extent of the radar fine line from its first detection till it passes over the ASOS station using Level II radar reflectivity and ArcGIS (Esri 2011). In a next step, we group each GF based on the location where the GF is first detected

with respect to the topography around the ASOS stations and from which direction the GF approaches the ASOS station. The NM study region is divided into three main groups with GFs (Fig. 3.4) that are first i) detected and continued to propagate through the Rio Grande Valley, ii) detected over the Sandia Foothills and Mountains and continued to propagate downhill into the Rio Grande Valley, and iii) detected over the West Central Highlands and continued to propagate into the Rio Grande Valley (Fig. 3.4; Table 3.1). GFs in the Rio Grande Valley are further subdivided depending on where they are first detected north, south, or west of the ASOS station. GFs from the Sandia Foothills and Mountains are subdivide into GFs that are first observed over the Foothills (Sandia Foothills) and those detected over the mountains (Sandia Mountains; Fig. 3.4). The GF detected on 2 July 2015 shown in Fig. 3.2 would be placed into the Sandia Foothills group as it was first detected along the foothills approaching the station from the southeast.

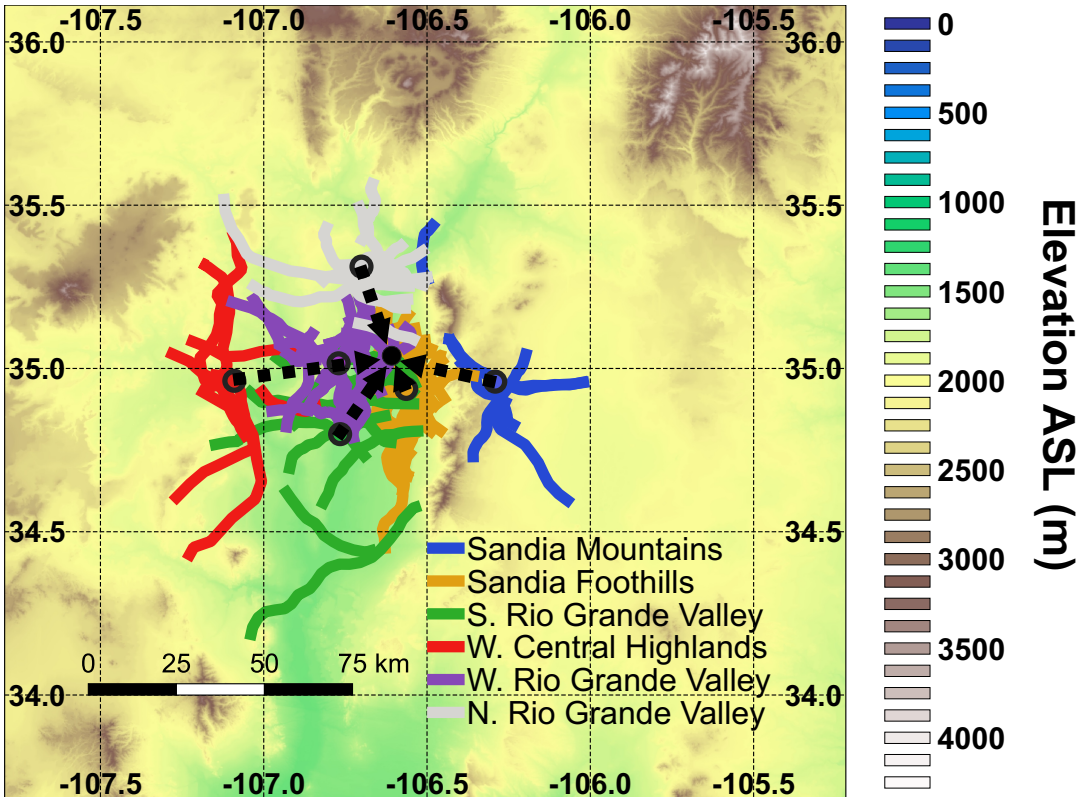

Fig. 3.4: Topographic map with radar fine lines for the 79 New Mexico GFs at the moment they first appear on the KABX operational radar at Albuquerque, New Mexico. GFs are grouped into six groups depending the location of first detection and the direction they propagate towards the KABQ New Mexico ASOS station (black dot). The open colored circles represent the centroid of each GF group. The black dashed arrows represent the path between the centroid and the ASOS station used to calculate the approximate terrain profile.

Table 3.1: Event overview for the 79 GFs observed between 2010-2018 passing over the New Mexico ASOS station. GFs are grouped into six areas depending on the location of first detection and the direction from which they approach the ASOS station. Number of GFs (N), the range of directions from which GFs propagate (º), the percentage of events that occurred in June, July, and August, and the percentage breakdown of parent thunderstorm (PTS) type are listed.

New Mexico							
Gust Front Area	N	Propagation Dir Range (°)	% of events in Jun	% of events in Jul	% of events in Aug	% Single Cell PTS	% Multicell PTS
Sandia Mountains	5	60 - 120	25	75	0	60	40
Sandia Foothills	30	60 - 150	1	76	13	77	23
S. Rio Grande Valley	10	135 - 195	20	50	30	40	60
W. Central Highlands	7	225 - 315	14	14	72	50	50
W. Rio Grande Valley	16	225 - 315	0	63	37	50	50
N. Rio Grande Valley	11	315 - 45	36	27	37	45	55

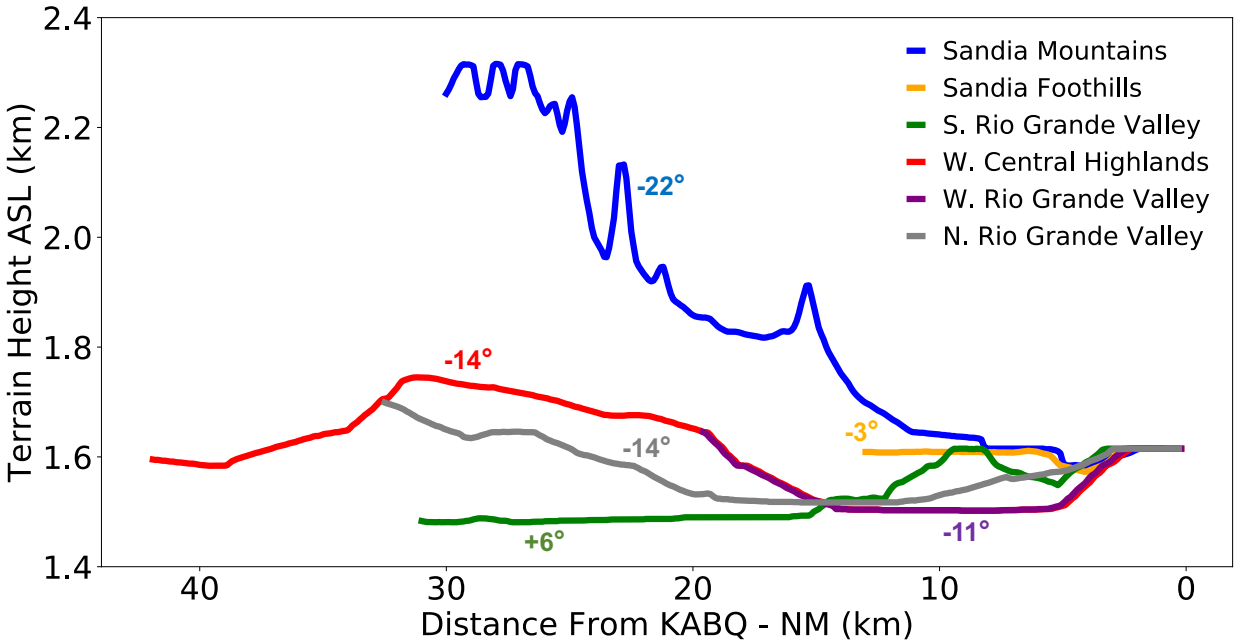

Fig. 3.5: Terrain height Above Sea Level (ASL) (km) along each New Mexico GF area's

propagation path to the KABQ ASOS station located at 0 km. Solid lines represent the terrain profile calculated from the mean centroid location of the detected radar fine lines for each gust front area to the KABQ ASOS station. Terrain profiles are derived using data from the 1/3 arcsecond United States Geological Survey (USGS) National Elevation Dataset (NED). The mean directional slope along each group's path is annotated as either (-) for downhill, or (+) for uphill.

In the AZ study region, GFs are grouped into those that are first detected on top of the Mogollon Rim i) east, ii) north, or iii) south of the ASOS station (Fig. 3.6; Table 3.2). Note that as the radar is located on top of the Rim, GFs originating in the lower terrain about ~1-1.5 km lower than the radar height might not be captured by the lowest radar scan at 0.47° until they move up to the Rim.

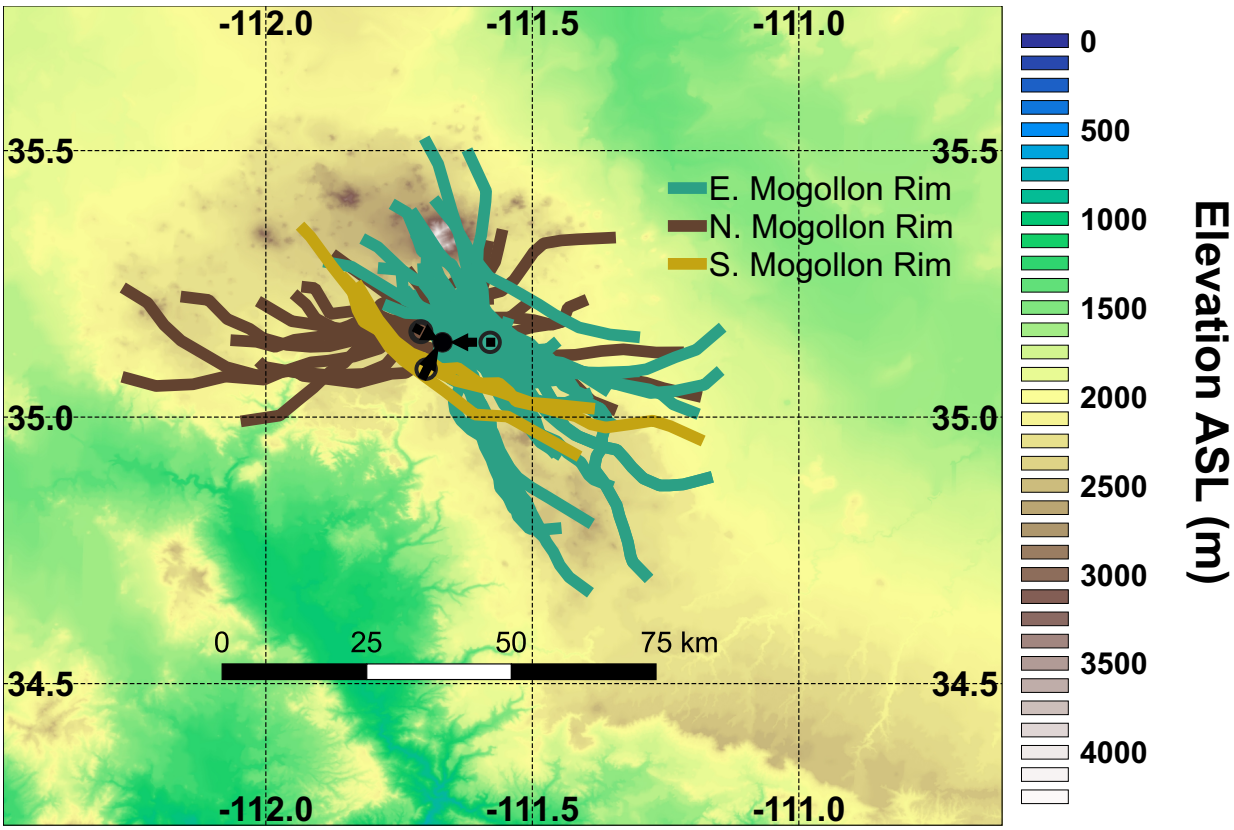

Fig. 3.6: As Fig. 3.4, but for the 43 Arizona GFs observed by the KFSX operational radar at Flagstaff, Arizona. GFs are grouped into three groups depending the location of first detection and the direction they propagate towards the KFLG Arizona ASOS station (black dot).

Table 3.2: As Table 3.1, but the event overview for the 43 GFs passing over the Arizona ASOS station.

Arizona							
Gust Front Area	N	Propagation Dir Range (°)	% of events in Jun	% of events in Jul	% of events in Aug	% Single Cell PTS	% Multicell PTS
E. Mogollon Rim	26	15 -135	0	77	23	38	62
N. Mogollon Rim	14	300 - 360	12	65	23	71	29
S. Mogollon Rim	3	180 - 225	67	33	0	67	33

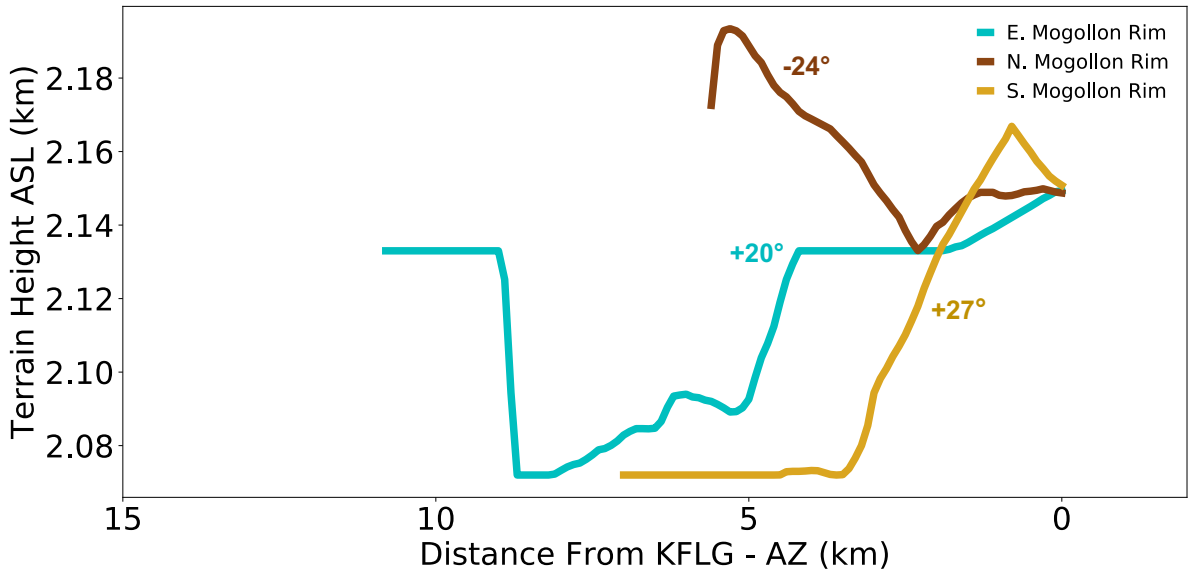

Fig. 3.7: Terrain height Above Sea Level (ASL) (km) along each Arizona GF area's propagation path to the KFLG ASOS station at 0 km. Solid lines represent the terrain profile calculated from the mean centroid location of the detected radar fine lines for each GF area to the KFLG ASOS station. Terrain profiles are derived using data from the 1/3 arc-second United States Geological Survey (USGS) National Elevation Dataset (NED). The mean directional slope along each area's path is also annotated as either (-) for downhill, or (+) for uphill.

Note that the GF grouping in each region is based on the location of when and where the fine lines are first detected by the operational radars, but do not necessarily represent the location and timing of when the GFs actually initiate. In NM, this is especially true east of the Sandia

Mountains, where the radar beam blockage is high (50 – 100 %) relative to the other NM areas. Similar challenges exist for detecting the initiation of GFs that propagate down from Humphreys Peak and up the sidewalls of the Mogollon Rim in AZ where the radar scan height is ~1 – 1.5 km AGL. Shallow GFs in these regions may not be detectable until they migrate within a closer range of the radars or into areas with less beam blockage. Despite this, grouping the GFs based on when and where the radars first detect them still provides inter-comparisons of GFs that encounter differing terrain features as they approach the ASOS stations.

3.3.6 Terrain Profiles

After grouping the GFs, we then calculate the initial detection centroid of all digitized GF fine lines in each group (open circle in Figs. 3.4, 3.6) and the terrain profile between the centroid and the ASOS station. By doing so, we can compare how differences in the variability of terrain for each group might influence GF propagation and its atmospheric characteristics. In order to calculate the initial detection centroid for each group, we first calculate the center point of each digitized radar fine line. The initial detection centroid is then found by calculating the weighted mean center of all radar fine line center points. The terrain profile consists of the height change between the initial detection centroid and the ASOS station and the mean terrain slope over the entire profile. The latter indicates if the GFs predominantly propagates downhill, experiencing adiabatic warming, or uphill, experiencing orographic lift and cooling.

Once terrain profiles for each GF group are calculated, we statistically compare the mean propagation speed and atmospheric characteristics within each study region and amongst the two study regions. We then explore if any differences in atmospheric characteristics can be attributed to the differing terrain profiles. We acknowledge that by using the centroids and mean terrain

profiles not all GFs within each group follow the exact same terrain path to the ASOS station. To address that we also conduct a sensitivity study where we use the exact terrain profile between the center point of each initially detected radar fine line and the ASOS station. However, we expect the deviation from the centroid terrain profile to be minimal for each GF profile, and therefore suspect that the centroid terrain profiles will be sufficient for facilitating comparisons amongst groups.

3.4 Results

3.4.1 Events Overview and Regional Comparison

During the 2010 to 2018 monsoonal seasons (June-August) 79 thunderstorm GFs are identified as radar fine lines that pass through the KABQ station in Albuquerque. GFs are first observed either over the terrain to the east and west of the station (53%) or within the Rio Grande Valley (47%). GFs propagate from the West Central Highlands approaching the ASOS station from the west (9% of the cases) or the Sandia Foothills (38%) and Mountains (6%) east of the ASOS station (Table 3.1; Fig. 3.4) propagating downslope into the Rio Grande Valley with mean slopes between -3 to -22° (Fig. 3.5). GFs also propagate downslope from the northern (14%) or western (20%) Rio Grande Valley with mean slopes of -11° and -14°, respectively. 13 % of the NM GFs are first observed in the southern Rio Grande Valley (Table 3.1; Fig. 3.4) and approach the station from the south and uphill with a mean slope of +6° (Fig. 3.5).

The largest number of GFs is observed in either July or August (Table 3.1). Note that, the number of GFs in the North Rio Grande Valley is more evenly spread across the three months compared to the West Central Highlands, Sandia Foothills, and Sandia Mountains. The GFs in this study develop from either single or multicell thunderstorms, with a relatively even spread

between the two thunderstorm types for most of the areas (Table 3.1). Note that supercell parent thunderstorms and squall lines are not observed during this time period in this area. The dominance of single and multicell thunderstorms and lack of supercell thunderstorms has also been observed in other studies of thunderstorms in complex terrain (Cotton et al. 1983; McAnelly and Cotton 1986; Tucker and Crook 1999; Luchetti et al. 2020).

In AZ, a total of 43 GFs are identified to pass through the KFLG ASOS station during the 2010 to 2018 monsoonal seasons (June- August). GFs are first observed on top of the Mogollon Rim east of the ASOS station traveling westwards (60% of the cases), north of the station traveling southwards (33 %), and south of the ASOS station traveling northwards (7%; Table 3.2; Fig. 3.6). East and South Mogollon Rim GFs propagate mainly uphill (mean slopes of 20 and 27°), while those from the North Mogollon Rim propagate mainly downhill with a mean slope of -24° (Fig. 3.7). Most of the GFs in the AZ study region also predominantly occur in the wetter monsoon months (July-August; Table 3.2). Similar to the NM GFs, all AZ GFs in this study develop from single or multicell thunderstorms (Table 3.2).

The NM and AZ study regions are similar in that they both reside in a predominantly dry climate and thunderstorms and precipitation are most frequent during the North American Moonsonal period (Adams and Comrie 1997). As outlined above, the two study regions differ in the dominant terrain feature present in each area with NM GFs predominantly propagating downhill into a valley (Fig. 3.4) and AZ GFs being either pushed uphill or propagate on top of a major ridgeline (Fig. 3.6). For the remaining analysis we will focus on exploring statistical differences between GFs that propagate down into and along a valley (NM) and those that are pushed up to and propagate on a ridgeline (AZ), as well as analyze any localized terrain effects amongst the categorized GF areas in both regions.

3.4.2 Propagation Speed and Magnitude Changes

3.4.2.1 GF Propagation Speed

When comparing the median propagation speed ($\widetilde{pspd}$) at the time of passage over the ASOS stations, NM GFs are faster with $\widetilde{pspd}$ ranging from 7.9 to 11.9 m s^{-1} (Fig. 3.8a), compared to AZ area GFs with $\widetilde{pspd}$ ranging from 4.1 to 7.2 m s^{-1} (Fig. 3.8b). Additionally, the mean propagation speed ($\overline{pspd}$) calculated across all 79 NM GFs is on average faster at 8.6 m s^{-1} compared to 5.2 m s^{-1} across the 43 AZ GFs (statistically significantly different at $p < 0.05$ using a two-sided Student's t-test) (Fig. 3.8). In general, the GFs in this study that propagate downhill into and along the Rio Grande Valley in NM are faster compared to the GFs that are pushed up to the crest of the Mogollon Rim in AZ. These results are likely related to acceleration by cold air density currents which is typically observed in laboratory experiments of density currents traveling downslope (e.g., Dai et al. 2012; Dai and Huang 2016; He et al. 2017).

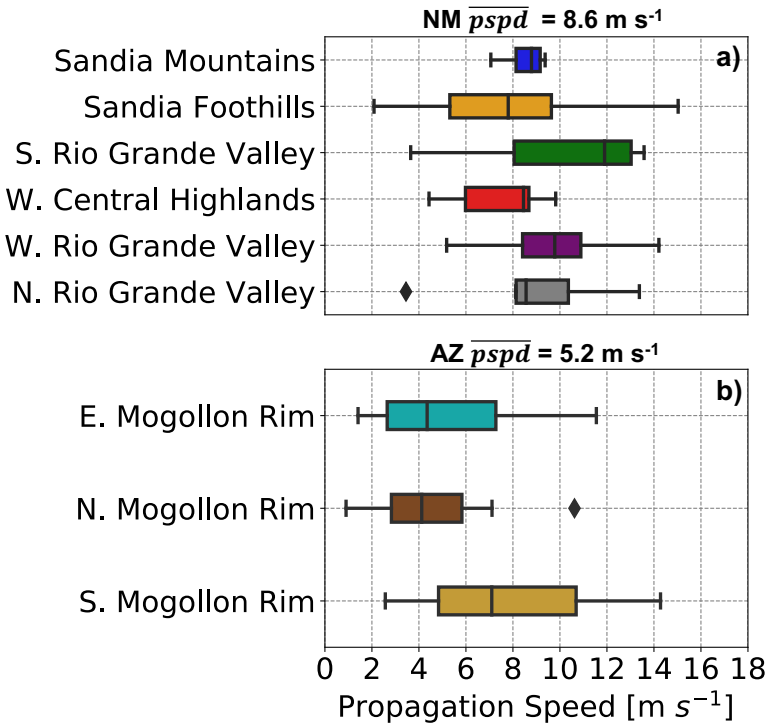

Fig. 3.8: Box-and-whiskers plots of radar-derived GF propagation speeds (m s^{-1}) for gust front groups observed in a) New Mexico and b) Arizona. The mean propagation speed across all 79 NM and 43 AZ GFs is listed at the top of panel a) and b), respectively. The filled boxes represent the interquartile range for each individual GF area in both study regions. The whiskers extend to data points that fall within 1.5 times the interquartile range of the lower and upper quantiles. Outliers that fall beyond this range are independently represented by diamond symbols. Colors correspond to each individual GF area shown in Figs. 3.4 and 3.6.

We also analyze the influence of the pre-frontal ambient wind on each GF, which can act to slow down (headwind) or speed up (tailwind) propagating GFs (Simpson and Britter 1980; Jorgensen et al. 2003). Fitting the observed propagation speed to the pre-frontal ambient wind through linear regression (Fig. 3.9a), we find that faster GFs in the Rio Grande Valley in NM often do not have stronger tailwinds with a coefficient of determination of $R^2 = 0.07$ and correlation of $r = 0.26$ (not statistically significant at $p < 0.05$ using a two-sided t-test with confidence intervals based on the Fisher transformation). This suggests that there is no linear relationship between the pre-frontal ambient wind and the GF propagation speed in the NM cases

discussed here. Atop the Mogollon Rim in AZ, however, this linear relationship is slightly stronger with $R^2 = 0.32$ and $r = 0.57$ (statistically significant at $p < 0.05$ using a two-sided t-test with confidence intervals based on the Fisher transformation), suggesting that faster (slower) AZ GFs often do have stronger tailwinds (headwinds) (Fig. 3.9b). Note that both Breusch-Pagan and White tests are performed as the data in Fig. 3.9b visually appears to be heteroscedastic. Both tests resulted in high p values, concluding that the data are not heteroscedastic and, therefore, linear regression is not violated. However, the GF propagation speed in Fig. 3.9b does appear to increase in variability as the magnitude of the pre-frontal tailwind increases. This may suggest that if the tailwind is too strong, it may suppress the GF as opposed to accelerate it in some cases. This is often reported in studies of sea breeze (also a density current) interactions with onshore ambient tailwinds (e.g., Aritt 1993; Gilliam et al. 2004). Regardless, the GFs in this study that are pushed up to the crest of the Mogollon Rim in AZ are more likely to be influenced by the magnitude and direction of the pre-frontal ambient wind compared to those GFs propagating down into and along the Rio Grande Valley in NM.

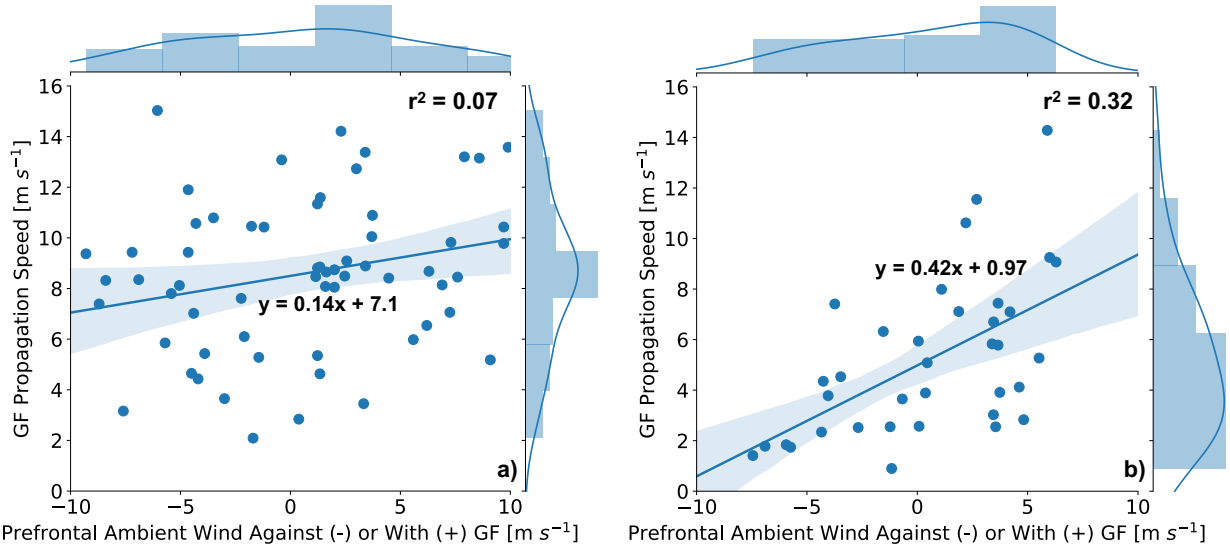

Fig. 3.9: Scatter plot of radar-derived propagation speed (m s^{-1}) as a function of the prefrontal ambient wind component (m s^{-1}) for GFs in a) New Mexico and b) Arizona.
The prefrontal cross-front ambient wind is derived by wind anemometers deployed at the ASOS stations. Linear regression fit is plotted as the solid blue line with coefficient of determination (r^2) shown in the upper right. The blue shaded region surrounding the regressed fit is the 95% confidence intervals of the regression. The fitted distribution for each axis is displayed as histograms.

3.4.2.2 GF Temperature, Relative Humidity, Wind Speed and Direction

The median temperature decrease ($\Delta\tilde{T}$) during passage for NM GFs ranges from 0.4 to 2.8 °C (Fig. 3.10a), compared to AZ GFs with 1.3 < $\Delta\tilde{T}$ < 2.8 °C (Fig. 3.10e). Additionally, when comparing the mean temperature difference ($\Delta\bar{T}$) across all GF events in both regions, we find that the $\Delta\bar{T}$ decrease is on average larger for the 79 NM GFs ($\Delta\bar{T}$ = -2.2°C) when compared to the 43 AZ GFs where $\Delta\bar{T}$ = -1.5°C (Fig. 3.10). The difference is statistically significant at p < 0.05 using a two-sided Student's t-test. Therefore, the GFs in this study that propagate down into and along the Rio Grande Valley in NM experience larger decreases in temperature compared to the GFs that are pushed up to the crest of the Mogollon Rim in AZ. Again, these findings are consistent with density current experiments which show that for currents traveling upslope, the associated cold air driving the current tends to thin out with increasing upslope angles (Marleau et al. 2014; Lombardi et al. 2015; De Falco et al. 2020).

The median change in relative humidity ($\Delta\widetilde{RH}$) is smaller across the NM area GFs ranging from -0.01 to 6.7 % (Fig. 3.10b), compared to the AZ GFs with 3.2 < $\Delta\widetilde{RH}$ < 10.4 % (Fig. 3.10f). The mean change in relative humidity ($\Delta\overline{RH}$) across all 43 AZ GFs is also higher ($\Delta\overline{RH}$ = 5.8 %) compared to the 79 NM GFs ($\Delta\overline{RH}$ = 3.5%) with a statistically significant difference at p < 0.05 using a two-sided Student's t-test (Fig. 3.10). GFs in this study that propagate atop the Mogollon Rim in AZ, therefore, experience larger increases in RH compared to those that propagate down

into and along the Rio Grande Valley in NM. An analysis of the dew point temperature change (ΔT_d) reveals that the AZ GFs are associated with larger changes in absolute moisture ($\Delta\bar{T}_d$ = 1.8 °C) during GF passage compared to NM GFs ($\Delta\bar{T}_d$ = 0.8 °C) (statistically significantly different at $p < 0.05$ using a two-sided Student's t-test; not shown). Thus, relative to the prefrontal ambient air, GFs that propagate down into Rio Grande Valley in NM are cooler, but also drier compared to those atop the Mogollon Rim in AZ, which explains the smaller changes in RH observed in NM.

As the GFs pass through the ASOS stations, the median increase in horizontal wind speed ($\Delta\widetilde{wsp}$) is larger across the NM GFs ranging from 5.2 to 8.7 m s^{-1} (Fig. 3.10c), compared to the AZ GFs with 2.9 < $\Delta\widetilde{wsp}$ < 4.8 m s^{-1} (Fig. 3.10g). Furthermore, the mean increase in wind speed ($\Delta\overline{wsp}$) across all 79 NM GFs is larger ($\Delta\overline{wsp}$ = 7.5 m s^{-1}) compared to the 43 AZ GFs ($\Delta\overline{wsp}$ = 3.5 m s^{-1}). The difference between $\Delta\overline{wsp}$ is statistically significant at $p < 0.05$ using a two-sided Student's t-test (Fig. 3.10). Thus, the GFs in this study that propagated downhill into and along the Rio Grande Valley in NM generally produced larger increases in wind speed compared to those that are pushed up to and propagate atop the Mogollon Rim in AZ. These results agree with density current theory which suggests that the larger the temperature difference between the cold air of the density current and the warmer environmental air (true for NM GFs in this study), the stronger the difference in wind speeds across the different air masses (Benjamin 1968; Simpson and Britter 1980; Jorgensen et al. 2003).

After passing over the ASOS stations, the median absolute magnitude change in wind direction ($\Delta\widetilde{wdir}$) is larger across the NM GFs ranging between 26.2 and 99.3° (Fig. 3.10d) compared to the AZ GFs with 39.2 < $\Delta\widetilde{wdir}$ < 54.8° (Fig. 3.10h). Using a two-sided Student's t-test, the mean wind direction change across the 79 NM GFs ($\Delta\overline{wdir}$ = 76.5°) is found to be

statistically significantly larger at $p < 0.05$ when compared to $\Delta\overline{wdir}$ across the 43 AZ GFs ($\Delta\overline{wdir}$ = 53.1°). Therefore, GFs that propagated downhill into the Rio Grande Valley in NM on average produce larger $\Delta wdir$ compared to those that propagated atop the Mogollon Rim in AZ.

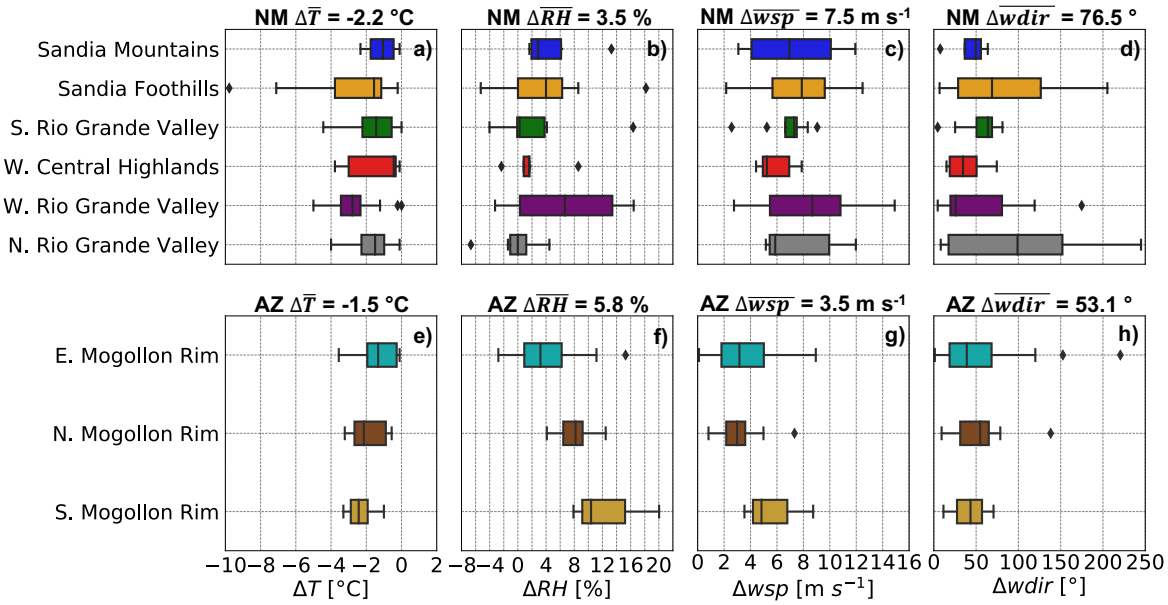

Fig. 3.10: As Fig. 3.8., but for the a, e) magnitude change in temperature (°C), b, f) the magnitude change in relative humidity (%), c, g) the magnitude change in wind speed (m s^{-1}), and d, h) the magnitude change in wind direction (°). The mean value for each variable across the 79 NM GFs is listed atop the upper panels (a-d), and the mean value for each variable across the 43 AZ GFs is listed atop the bottom panels (e-h).

3.4.2.3 Relationship Between Magnitude Change in Temperature and Wind Speed

In both terrain regions, the magnitude decrease in temperature is often accompanied by a magnitude increase in horizontal wind speed (Fig. 3.11). However, this relationship is considerably stronger for GFs in the Rio Grande Valley in NM with a correlation of $r = 0.57$ and $R^2 = 0.33$ (statistically significant at $p < 0.05$ using a two-sided t-test with confidence intervals based on the Fisher transformation) (Fig. 3.11a), compared to those atop the Mogollon Rim in

AZ (r = 0.28; R^2 = 0.08; not statistically significant at $p < 0.05$ using a two-sided t-test with confidence intervals based on the Fisher transformation) (Fig. 3.11b). Therefore, the GFs in this study that propagate downhill into and along the Rio Grande Valley in NM tend to behave more consistently in accordance with density current theory. GFs atop the Mogollon Rim in AZ, however, do not behave like density currents considering the weak relationship (r = 0.28; R^2 = 0.08) between the magnitude decrease in temperature and the magnitude increase in horizontal wind speed observed here (Fig. 3.11b).

While the NM GFs discussed thus far are associated with expected decreases in temperature during passage over the KABQ ASOS station, we did observe 15 additional GFs (not included in the analysis pertaining to the 79 NM cases discussed above) that actually induce an increase in temperature during passage (not shown). The mean propagation speed ($\overline{pspd}$) across these 15 GFs at time of passage is 8.2 m s^{-1}, with a mean increase in wind speed ($\Delta\overline{wsp}$) of 5.1 m s^{-1}. These 15 GFs are visible on radar as fine lines propagating at speeds similar to the 79 NM GFs ($\overline{pspd}$ = 8.6 m s^{-1}) associated with decreases in temperature (Fig. 3.8a). Perhaps, the cold air driving these 15 GFs may be elevated above the surface and, thus, the boundary is only detectable as a radar fine line and not by the ASOS station itself. An alternative hypothesis, however, is perhaps these 15 GFs are simply associated with very little precipitation, resulting in weak GFs which induce downslope warming observed by the ASOS station.

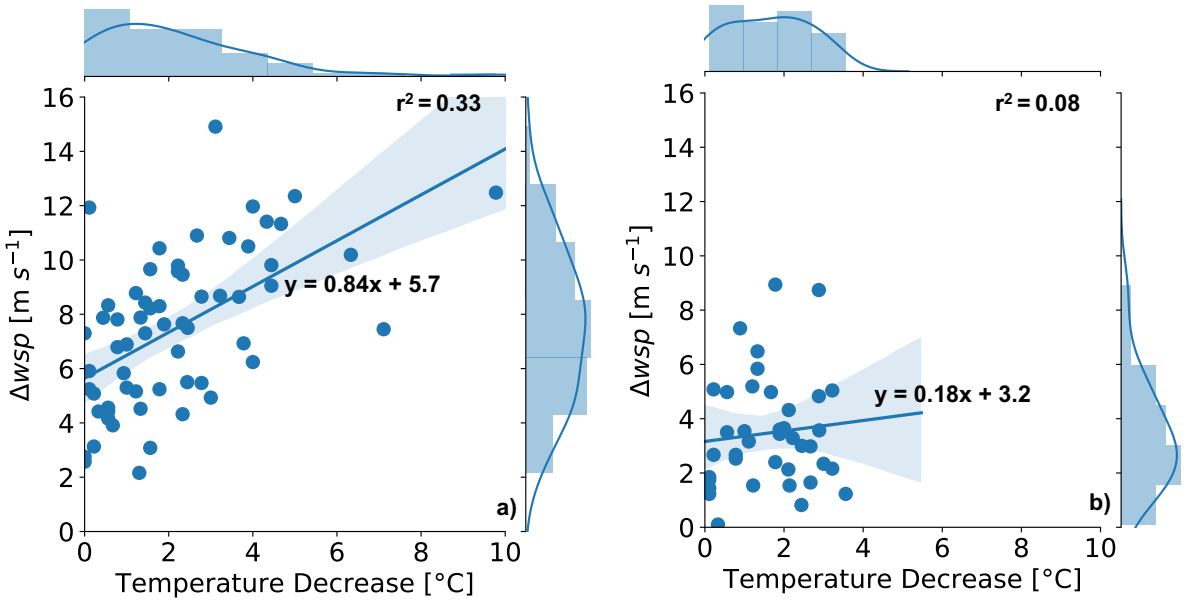

Fig. 3.11: As Fig. 3.9, but comparison of the magnitude change in wind speed (m s^{-1}) as a function of the decrease in temperature (°C) measured by the ASOS stations in a) New Mexico and b) Arizona.

3.5 Discussion – Role of Topography

Terrain profiles for each study region are calculated to quantify the potential influence of adiabatic heating and cooling on GF characteristics (see section 3.3.6, Figs. 3.5, 3.7). For NM GFs that propagate downhill, smaller $\Delta\tilde{T}$ and $\Delta\widetilde{wsp}$ are observed for GFs from areas experiencing steeper terrain downslopes (-14 to -22°) (e.g., Sandia Mountains, West Central Highlands, North Rio Grande Valley; Fig. 3.10a, c), when compared to areas experiencing shallower terrain downslopes (-3 to -11°) (e.g., Sandia Foothills and West Rio Grande Valley; Fig. 3.10a, c). Statistically, a positive, albeit weak relationship between the magnitude decrease in temperature and the mean terrain slope calculated for each individual NM GF is observed (r = 0.24; R^2 = 0.06, statistically significant at p <0.05 using a two-sided t-test with confidence intervals based on the Fisher transformation) (Fig. 3.12a). This suggests that larger magnitude decreases in temperature are weakly associated with less negative mean terrain slopes.

Furthermore, a positive relationship between the magnitude change in wind speed and the mean terrain slope for each individual NM GF is observed (r = 0.36; R^2 = 0.13, statistically significant at p <0.05 using a two-sided t-test with confidence intervals based on the Fisher transformation) (Fig. 3.12b). This suggests that larger increases in wind speed are also weakly associated with less negative mean terrain slopes for the NM cases studied here. Therefore, perhaps subtle differences in GF strength can be partially attributed to the degree of downslope adiabatic warming potential for GFs that propagate down or within valley slopes.

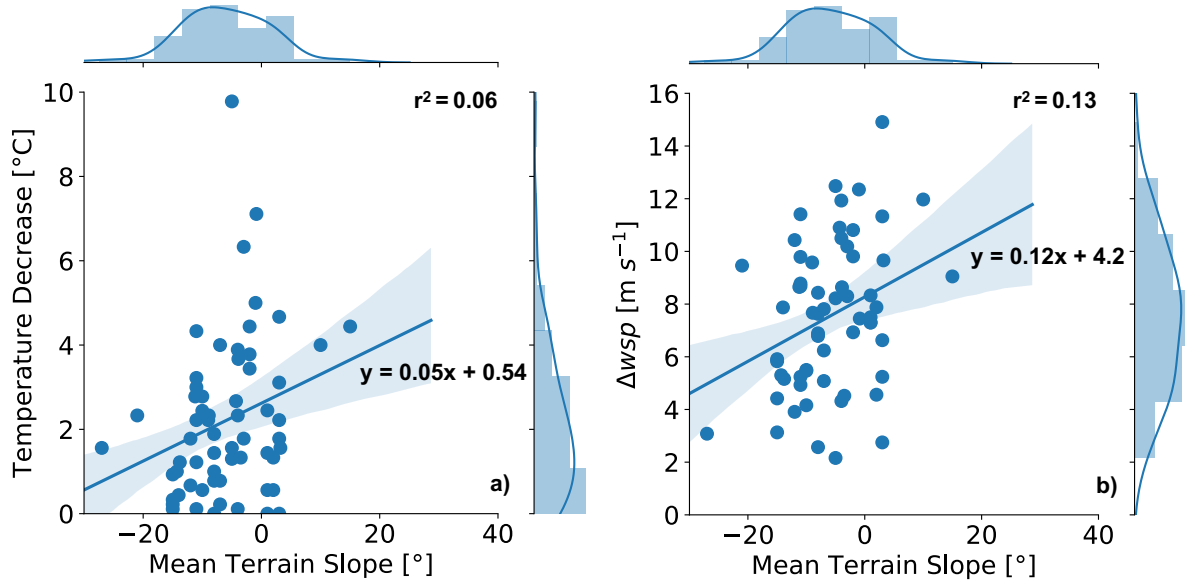

Fig. 3.12: As Fig. 3.9, but comparison of a) the decrease in temperature (°C), and b) the magnitude change in wind speed (m s^{-1}) measured by the New Mexico KABQ ASOS station, each as a function of the mean directional terrain slope (°) calculated along the propagation path for each individual GF.

In AZ, there is no discernable relationship between upslope or downslope adiabatic processes and GF strength. For example, $\Delta\tilde{T}$ for GFs from the North Mogollon Rim is actually larger ($\Delta\tilde{T}$ = -2.1°C) than for GFs from the East Mogollon Rim with $\Delta\tilde{T}$= -1.3°C (Fig. 3.10e), despite a strong mean terrain downslope (-24°) profile from the north side of the rim (Fig. 3.7). Similarly,

$\Delta\widetilde{wsp}$ is essentially identical ($\Delta\widetilde{wsp}$= 2.9 m s^{-1}; $\Delta\widetilde{wsp}$ = 3.0 m s^{-1}) when comparing these two areas (Fig. 3.10g). For GFs from the South Mogollon Rim, whether upslope adiabatic cooling contributes to the larger median temperature decrease ($\Delta\tilde{T}$= -2.8°C) (Fig. 3.10e) and larger median increase in wind speed ($\Delta\widetilde{wsp}$= 4.8 m s^{-1}) (Fig. 3.10g) is difficult to discern with only three GF cases. Statistically, the correlation between the magnitude decrease in temperature and the mean terrain slope calculated for each individual AZ GF is very weak (r = 0.03; R^2 = 0.001, not statistically significant at $p < 0.05$ using a two-sided t-test with confidence intervals based on the Fisher transformation) (Fig. 3.13a). This further suggests no connection between the degree of downslope warming or upslope cooling potential and the magnitude decrease in temperature associated with the AZ GFs analyzed here. A weakly positive relationship between the magnitude change in wind speed and the mean terrain slope for each individual AZ GF is observed (r = 0.35; R^2 = 0.11) (Fig. 3.13b). However, this relationship is not statistically significant at p <0.05 when using a two-sided t-test with confidence intervals based on the Fisher transformation. Therefore, given these weak, non-statistically significant relationships, the degree of downslope adiabatic warming or upslope cooling potential does not influence GF strength for the AZ cases studied here.

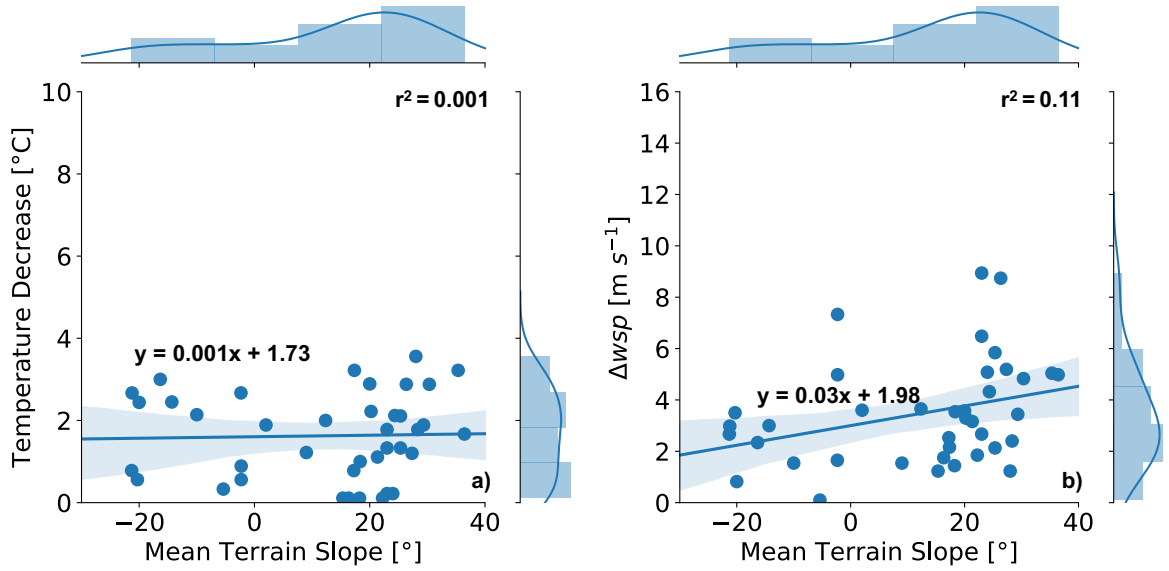

Fig. 3.13: As Fig. 3.9, but comparison of a) the decrease in temperature (°C), and b) the magnitude change in wind speed (m s^{-1}) measured by the Arizona KFLG ASOS station, each as a function of the mean directional terrain slope (°) calculated along the propagation path for each individual GF.

While localized adiabatic influence on the GFs in this study is hard to discern, comparisons of GFs between the two regions show that GFs that propagate downhill into and along the Rio Grande Valley in NM are generally associated with faster propagation speeds ($\overline{pspd}$ = 8.6 m s^{-1}), larger decreases in temperature ($\Delta\bar{T}$ = -2.2°C), and larger increases in horizontal wind speeds ($\Delta\overline{wsp}$ = 7.5 m s^{-1}) and wind direction ($\Delta\overline{wdir}$ = 76.5°) compared to GFs that reach the crest of the Mogollon Rim in AZ ($\overline{pspd}$= 5.2 m s^{-1}; $\Delta\bar{T}$ = -1.5°C; $\Delta\overline{wsp}$ = 3.5 m s^{-1}; $\Delta\overline{wdir}$ = 53.1°). The results suggest that GFs that primarily propagate downhill into (between -3 and -22°) and within a valley may induce larger increases in wind speed during passage compared to those that are pushed uphill (between 20 to 27°) to or propagate atop a ridgeline. These findings agree with Kishcha et al. (2016) who also observed strong maximum horizontal wind speeds ($\Delta\overline{wsp}$ = 12 m s^{-1}) associated with a downslope accelerated GF on the lee side of the Judean Mountains in the Dead Sea valley. Conversely, Luchetti et al. (2020) observed $\Delta\widetilde{wsp}$ increases of < 4 m s^{-1} close

to the surface (< 25 m AGL) across 24 GFs that primarily propagated uphill to study sites located in the Colorado Front Range. These values are similar to those produced by the AZ GFs studied atop the Mogollon Rim ($2.9 < \Delta\widetilde{wsp} < 4.8$ m s^{-1}), but weaker than the GFs that propagated downhill into and along the Rio Grande Valley in NM ($5.2 < \Delta\widetilde{wsp} < 8.7$ m s^{-1}). Therefore, the results in this study support observational findings from previous work suggesting that GFs that travel downslope (upslope) can accelerate (decelerate) and induce larger (smaller) increases in wind speed (Kishcha et al. 2016; Luchetti et al. 2020). Furthermore, laboratory and numerical experiments of density current interactions with upslope inclines show that as the upslope angle increases, density currents become thinner and gravity parallel to the upslope induces a deceleration of the density current (Marleau et al. 2014; Lombardi et al. 2015; De Falco et al. 2020). For density currents propagating downslope, an acceleration phase is observed as available potential energy is converted into kinetic energy (Dai et al. 2012; Dai and Huang 2016; He et al. 2017). Since GFs often behave like density currents (Charba 1974; Sasaki and Baxter 1986; Friedrich et al. 2005), differences in propagation speed between GFs pushed up to and atop the Mogollon Rim in AZ ($\overline{pspd}$ = 5.2 m s^{-1}) and those that propagate downhill into and along the Rio Grande Valley in NM ($\overline{pspd}$ = 8.6 m s^{-1}) provides observational evidence supporting the results of previous laboratory experiments investigating the influence of upslope and downslope surfaces on density current speed.

3.6 Conclusions

This study quantifies the variability in propagation speed and atmospheric characteristics across 122 GFs that occur in the complex terrain of NM and AZ during the 2010 to 2018 monsoonal seasons (June- August). Using radar and ASOS station data, GFs that were pushed

uphill and propagated atop the crest of the Mogollon Rim in AZ were compared to those that propagated down into or along the Rio Grande Valley in NM to assess how variability in terrain may influence GF characteristics. The main findings from this analysis are:

- GFs that propagated downhill into and along the Rio Grande Valley in NM were generally associated with faster propagation speeds ($\overline{pspd}$ = 8.6 m s^{-1}), slightly larger decreases in temperature ($\Delta\bar{T}$ = -2.2°C), larger increases in horizontal wind speeds ($\Delta\overline{wsp}$ = 7.5 m s^{-1}) and changes in wind direction ($\Delta\overline{wdir}$ = 76.5°) compared to GFs that reached the crest of the Mogollon Rim in AZ ($\overline{pspd}$ = 5.2 m s^{-1}; $\Delta\bar{T}$ = -1.5°C; $\Delta\overline{wsp}$ = 3.5 m s^{-1}; $\Delta\overline{wdir}$ = 53.1°).
- The pre-frontal ambient wind was not a strong determining factor for GF propagation speed (r = 0.26; R^2 = 0.07) for those that propagated downhill into and along the Rio Grande Valley in NM. However, faster (slower) AZ GFs often did have stronger tailwinds (headwinds) (r = 0.57; R^2 = 0.32), and thus the pre-frontal ambient wind did moderately influence propagation speed for the cases studied atop the Mogollon Rim in AZ.
- GFs that propagated downhill into the Rio Grande Valley in NM behaved more in accordance with traditional density current theory than those that were pushed uphill and propagated atop the Mogollon Rim in AZ. In the theory, the stronger the difference in temperature between the boundary and the ambient air, the stronger the wind speeds behind the two air masses. Here, the relationship between the magnitude decrease in temperature and magnitude increase in wind speed was stronger for GFs that propagated down into and along the Rio Grande Valley in NM (r = 0.57; R^2 = 0.33) compared to those atop the Mogollon Rim in AZ (r = 0.28, R^2 = 0.08).

- For GFs that propagated downhill and within the Rio Grande Valley in NM, larger magnitude decreases in temperature were weakly associated with those that encountered less negative mean terrain slopes ($r = 0.24$; $R^2 = 0.06$). Similarly, larger magnitude changes in wind speed were also associated with less negative mean terrain slopes ($r = 0.36$; $R^2 = 0.13$). For GFs that propagated uphill and atop the Mogollon Rim in AZ, no discernable relationships between upslope or downslope adiabatic processes and GF wind speed and temperature drop was found.

Results from this study provide an initial step in understanding the influence of common terrain features on propagating thunderstorm GFs. A future study should compare the results here to other terrain regions where GFs either propagate down into valleys or get pushed up and over ridgelines, or to those that interact with other terrain features such as plateaus or depressions. Additional observations could benefit numerical models which must be able to accurately incorporate the influence of terrain features on the strength and modification of thunderstorm GFs. This is particularly true for operational turbulence-resolving fire models, where their accuracy is highly dependent on the model's ability to simulate realistic turbulent boundaries in the vicinity of wildfires in areas of complex terrain.

One potential limitation here, however, is that we are trying to link GF characteristics observed at a fixed location in time and space to the mean slope across the entire terrain profile. While the mean slope may suggest a primarily downhill path, for example, the actual profile likely includes alternating uphill and downhill sections (e.g., West Central Highlands in Fig. 3.5). Therefore, a future study could utilize a Lagrangian modeling approach to quantify the changes in GF characteristics at every uphill and downhill stretch of the profile. This type of

approach would likely yield a better understanding of whether or not downslope or upslope adiabatic processes influence GF characteristics.

3.7 Acknowledgement

This research is supported through an award L17AC00227 ("JFSP Project 17-1-05-2 Evaluating thunderstorm outflow boundaries in WRF-Fire") from the Bureau of Land Management (BLM) as part of the Joint Fire Science Program under the subject opportunity FA-FON0017-0002. The authors would like to thank Craig Schwartz of NCAR and the anonymous reviewer of this manuscript for their comments and suggestions which strengthened the fundamentals of this article.

4 Quantifying Microburst Wind and Turbulence Enhancement in Canyons

This chapter is a preliminary version of a manuscript to be submitted to *Monthly Weather Review*:

Luchetti, N. T., K. Friedrich, B. Kosovic, 2020: Quantifying Microburst Wind and Turbulence Enhancement in Canyons. *Mon. Wea. Rev.* Submitted January, 2021.

4.1 Abstract

Thunderstorms in arid and semi-arid regions like the U.S. intermountain west are often associated with dry microbursts. These microbursts are caused by evaporating precipitation in dry environments causing strong and difficult-to-observe cold outflow boundaries associated with rapid changes in wind and turbulence. A particularly dangerous situation can occur when microburst outflow winds are terrain-channeled into and within canyons during ongoing wildfire events, creating complex tactical challenges for firefighters and emergency managers. Given the dangers to firefighters by unpredictable microbursts and outflow boundaries within canyons, this paper quantifies the canyon-enhancement of wind and turbulence from microburst outflow boundaries for both short- and long-distance canyons for a range of canyon slopes and distances to the downdraft. These canyon simulations are compared to microburst outflow boundary characteristics in flat terrain. For microburst flow over both short- and long-distance canyons, the maximum increase in horizontal winds, upward vertical velocity, and turbulence kinetic energy (*TKE)* is stronger within and along the walls of canyons located closer to the microburst compared to those farther away from the microburst. For canyons located closer to the microburst, the increase in horizontal winds, upward vertical velocity, and TKE is stronger within and along the steeper sloped canyons compared to the gradually sloped canyons. Lastly, the topographic multiplier for horizontal winds is higher within the long-distance canyons compared to the short-distance canyons.

4.2 Introduction

Thunderstorms are often associated with dangerous downdrafts also referred to as microbursts. Dry microbursts, often found in arid and semi-arid regions like the United States intermountain west, develop by evaporation, melting, and sublimation of precipitation causing strong and turbulent ground-level winds that propagate as outflow boundaries radially away from the microburst (Fujita and Wakimoto 1983; Wilson et al. 1984; Fujita 1985). Dry microbursts are often short-lived (< 10 min) with typical diameters of < 4 km and occur with very little rain reaching the surface. As such, they are almost impossible to detect with operational observing networks (Haines 1988; Wakimoto et al. 1994), particularly in mountainous terrain where observational density is sparse and measurements are obscured by the mountains. Microbursts and outflow boundaries in mountain terrain pose a major threat to firefighters' safety as microbursts and outflow boundaries can spread the fire rapidly towards locations that were previously considered safe. Furthermore, terrain itself can enhance and modify microburst and outflow boundary winds adding complexity and tactical challenges faced by emergency management teams during wildfire events (Goens and Andrews 1998; Sharples et al. 2017). Given the potential threat and the lack of observations, this study quantifies changes in wind speed and turbulence from microbursts and outflow boundaries interacting with canyons and ridges through idealized simulations using the community numerical Weather Research and Forecasting (WRF) model.

Outflow boundaries associated with intense dry microbursts are difficult to predict and observe, given that they are typically associated with high cloud bases and precipitation that evaporates before reaching the ground (Monastersky 1987; Haines 1988; Wakimoto et al. 1994; Potter and Hernandez 2017). Observations of dry microbursts across the intermountain west

reveal that many of these events are associated with low radar reflectivity signatures (Wakimoto et al. 1994), making them difficult to observe by radar meteorologists or trained severe weather spotters in the field (Haines 1988). A deadly example of a dry microburst interaction with a wildfire occurred on 26 June 1990, as hundreds of firefighters fought the Arizona Dude Fire in the hills of the Tonto National Forest northeast of Phoenix, AZ. Surface winds, associated with several dry microbursts developing in the vicinity of the fire, caused the fire to spread in all directions. On the southern side of the fire, these surface winds were enhanced by the local terrain and channeled into a canyon, where six firefighters were killed (Goens and Andrews 1998). Strong surface microburst gusts in combination with complex terrain and wildfires have caused fatalities in other wildfires such as the 1949 Mann Gulch Fire (Rothermel 1993), the 1976 Battlement Fire (USDI 1976), the 1994 South Canyon Fire (USDI/USDA 1994), the 2012 Waldo Canyon Fire (Johnson et al. 2014), the 2013 Arizona Yarnell Hill Fire (Karels and Dudley 2013), and the 2015 California Frog Fire (Draeger 2016). Considering the potential safety hazards associated with outflow boundary-induced fire spread in mountainous areas and the lack of observations, the use of high-resolution numerical weather models to accurately simulate thunderstorm outflow boundaries in complex terrain is a research priority for the fire weather community (Joint Fire Science Program 2017).

Most numerical studies of microburst outflow interactions with terrain have focused on bell-shaped 2-D hills or mountains, and escarpment-like features (Letchford and Illidge 1999; Wood et al. 2001; Mason et al. 2007, 2010). While wildfires can surely be influenced by these types of terrain features (e.g., Hawley 1926; Sullivan 2009; Sullivan et al. 2014), a dangerous situation can also develop when wildfires are terrain-channeled into and within canyons (Goens and Andrews 1998; Brown 2002; Esperanza Investigation Team 2006; Coen and Riggan 2010;

Sharples et al. 2010). For example, during the 2006 Esperanza Fire in California, Santa Ana winds aligned with channeled creek drainage flow in a nearby canyon, producing enhanced surface winds and fire behavior which led to the loss of five firefighters (Esperanza Investigation Team 2006; Coen and Riggan 2010). A key finding from the investigation report (Esperanza Investigation Team 2006) was that none of the fire shelters for the deceased firefighters were deployed, suggesting that the head fire must have accelerated as it came through the canyon and caught the firefighters off guard. Another canyon-induced fatality event occurred during the 2001 Thirtymile Fire in Washington where fire-induced winds were channeled up the canyon sidewall killing four firefighters who deployed at a site located 30 m upslope from the valley floor (Brown 2002). An analysis of tree needle heatset observations made at the incident site indicates that fire-induced winds were in the up-canyon and upslope direction, suggesting that the fire's convective column was channeled up the canyon, rather than rising vertically from the surface (Brown 2002). Further analysis suggests that the increased fire spread rate which caught the firefighters off guard likely resulted from a combination of up-canyon winds and downward mixing of stronger upper-level winds which were oriented along the canyon's axis. Explosive fire blow-up and acceleration such as in the events outlined above (1990 Dude Fire; 2006 Esperanza Fire; 2001 Thirtymile Fire) are not rare, especially for wildfires that occur within canyons (Veigas 2005; Viegas and Simeoni 2010). Thus, the combination of hard-to-predict surging microbursts, along with terrain channeling, presents an especially challenging situation for firefighters and emergency managers when responding to wildfires in canyons.

Given the dangers to firefighters by un-predictable microbursts and outflow boundaries in areas of complex terrain, along with a lack of focus on microburst interactions with canyons in the literature, the aim of this paper is to quantify the canyon-enhancement of wind and

turbulence from microburst outflow boundaries. Results are presented describing the influence of short- (1.5 - 4.5 km) and long- (3 - 6 km) distance canyons for a range of upwind and downwind slopes. The influence of microburst location (with respect to the topography) is also discussed. This study is organized as follows: Section 4.2 discusses the atmospheric model configuration and experimental design. Microburst simulation results and comparisons are presented and discussed in Section 4.3. Conclusions and suggestions for future work are discussed in Section 4.4.

4.3 Methods

4.3.1 WRF-LES Configuration

Simulations presented in this study are configured in WRF-large eddy simulation (LES) mode (WRF v3.6), where the most energetically significant turbulent eddies are explicitly resolved (Moeng et al. 2007; Mirocha et al. 2010). This fine-scale (grid spacings of $\Delta \sim 10 - 100$ m) representation of boundary layer turbulence is necessary to resolve the energy-containing turbulent motions that are responsible for most of the turbulent transport. The model is run with one outer domain (d01) and one inner domain (d02) (Table 4.1). The outer domain (d01) has a horizontal resolution of 90 m and uniform terrain-following (eta) coordinates. In the vertical, 73 levels are used with the finest resolution of 10 m in the lowest ⅔ of the domain. The inner domain (d02) has a horizontal resolution of 30 m, uniform terrain-following (eta) coordinates, and the same 73 vertical levels as in the outer domain (d01). A stable background atmosphere is used with an initial potential temperature of 295 K that increases at 0.005 K m^{-1} up to a planetary boundary layer (PBL) height of z_{pbl} = 750 m, and at 0.001 K m^{-1} through the remainder of the domain up to a z_{top} = 2 km. The Brunt-Vaisala frequency also highlights this stable profile with a

frequency of ~0.02 s^{-1} up to the top of the PBL (z_{pbl} = 750 m), followed by a gradual decrease in frequency to 0.01 s^{-1} through the remainder of the vertical profile. In order to maintain numerical stability and eliminate gravity waves that reflect off the upper boundary, a Rayleigh damper with a damping coefficient of 0.003 s^{-1} is applied near the top of the domains. A constant surface heat flux of 50 W m^2 is applied to both domains in order to spin up and maintain a realistic turbulent boundary layer throughout the duration of the simulations. The Thompson scheme is used to represent microphysical processes. Additionally, for simplicity, short grass is used and applied homogeneously across the domains to represent the land-surface type with a surface roughness length of 0.03 m. Radiative transfer processes are not considered in either domain.

Table 4.1: Domain configurations with horizontal resolution (Δ x, y), time step (Δ t), number of vertical model levels (Nz), and domain dimensions in the x, y, and z directions.

Domain	Δ x, y	Δ t	Nz	Dimensions [x,y,z]
d01	90 m	0.25 s	73	27 km x 27 km x 2 km
d02	30 m	0.13 s	73	13.5 km x 13.5 km x 2 km

To simulate realistic turbulent inflow into the inner domain (d02), unaffected by terrain features, one-way nesting is used. Both domains resolve turbulence explicitly using a 1.5 order Turbulence Kinetic Energy (*TKE*) closure model, but the outer domain (d01) uses a "flat-plate" lower surface boundary and periodic conditions (Mirocha et al. 2013; Nunalee et al. 2014). The outer domain (d01) provides turbulent inflow boundary conditions for the inner domain (d02), which includes terrain features in the lower surface boundary. To eliminate terrain-induced wake effects being recycled into the inflow turbulence from the outer domain (d01), feedback

between the inner domain (d02) and the outer domain (d01) is turned off. This technique allows for the inner domain (d02) to be fed realistic turbulent inflow without terrain-induced wake features. See Mirocha et al. (2013) and Nunalee et al. (2014) for more details on this technique.

Simulations are run for a total of seven hours, with the first six hours are used to "spin up" realistic turbulence across the domains. After turbulence is spun up, analysis is done over the final hour of the simulations (from 6 to 7 h). The six hour spin-up time is determined by assessing the temporal evolution of horizontally averaged *TKE* near the surface (e.g. Fig. 4.1). As the outer domain's (d01) flow travels downstream within the inner domain (d02), the streamwise *TKE* field eventually reaches a developed state characterized by low turbulent fluctuations (Fig. 4.2). At z = 250 m, this developed state occurs at x = ~10 km (Fig. 4.2a). At z = 750 m, the developed state occurs further downstream at x = ~12 km (Fig. 4.2b). Post- spin-up vertical profiles of potential temperature and the Brunt-Vaisala frequency highlight the fully-developed stable atmosphere described earlier (Fig. 4.3a -b). The vertical profile of horizontal wind speed, U_{horiz}, displays a low-level jet characterized by a maxima just above the surface, which gradually weakens with height (Fig. 4.3c). Modest low-level shear within the boundary layer, coupled with surface heat flux forcing produces a classically stable vertical *TKE* profile characterized by modest turbulence near the surface that rapidly drops off with height up to the top of the PBL (Fig. 4.3d).

At the end of the sixth hour, a cold bubble perturbation is introduced into the potential temperature field of the inner domain (d02) to initiate a downdraft (Grant and Heever 2016). The maximum cold air perturbation of -15 K is centered at z = 15 m; horizontal center points of the perturbation vary depending on the simulation and will be discussed in section 4.2.2. The perturbation stretches 1 km in the horizontal and 1.5 km in the vertical. In this post- spin-up

stable environment, the cold air perturbation descends, reaches the surface, and then produces a cold outflow boundary that propagates radially away from the center of the downdraft. The resulting downburst is short lived (< 10 min) and covers a small spatial scale (downdraft diameter < 4 km), which is consistent with microburst definitions from previous observational studies (Fujita and Wakimoto 1983; Wilson et al. 1984; Fujita 1985).

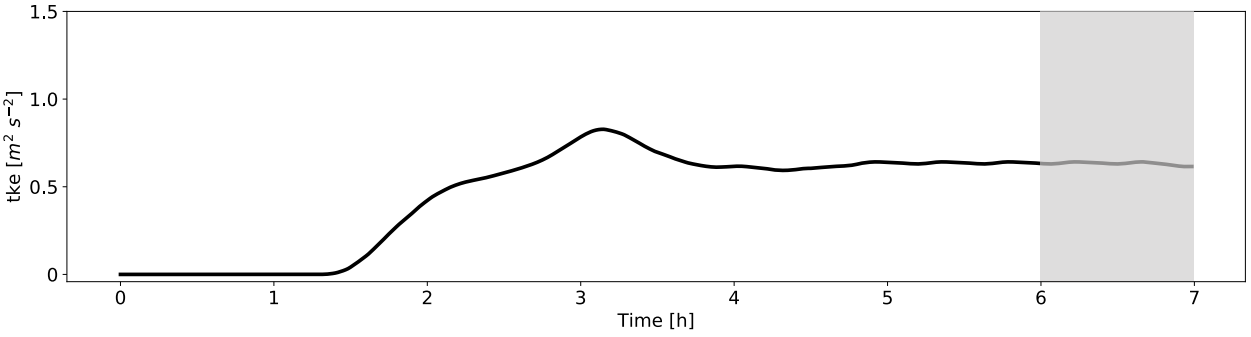

Fig. 4.1: Time-evolution of horizontally x-averaged resolved *TKE* at z = 250 m within the inner domain (d02). The gray area represents the time interval used to analyze all simulations [6 - 7 h].

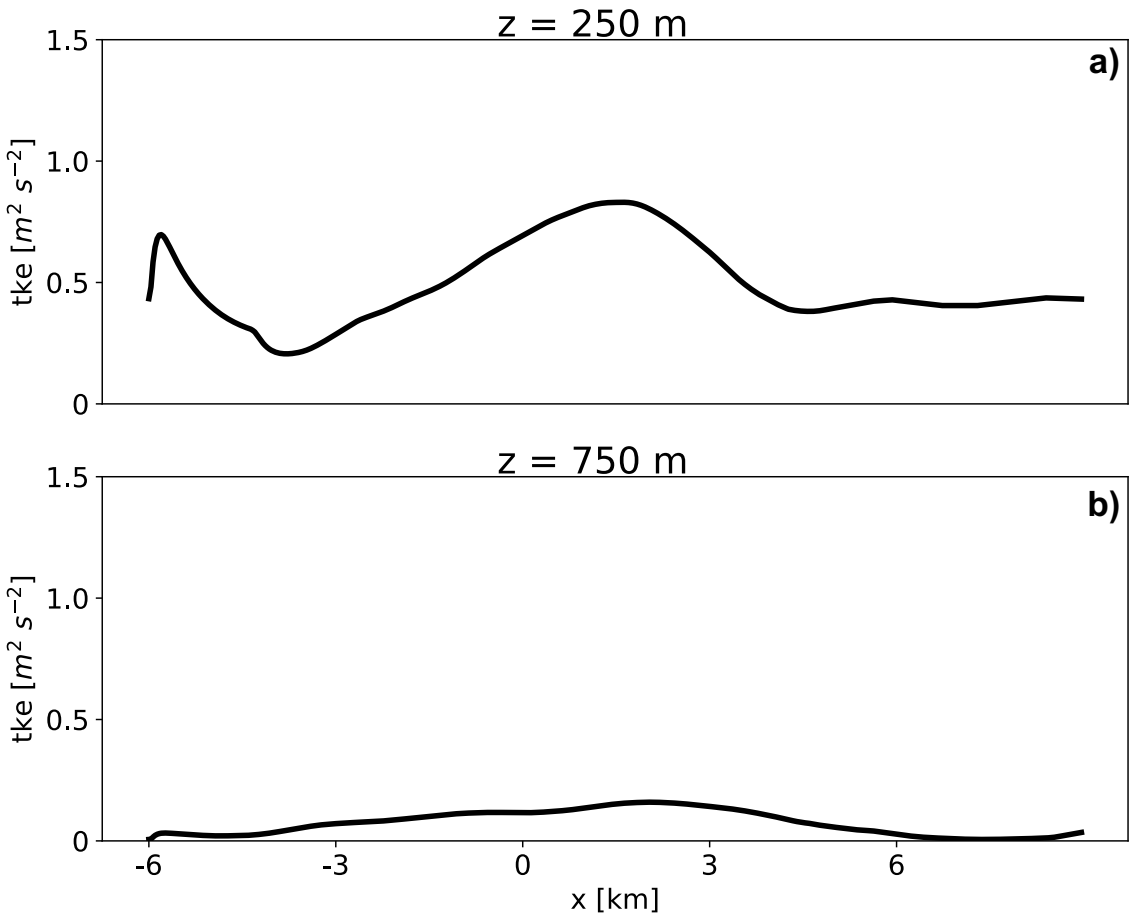

Fig. 4.2: Time and y-averaged, resolved *TKE* for the inner domain (d02) as a function of distance downstream of the inflow boundary at a) z = 250 m and b) z = 750 m from the post-spin-up time interval [6 - 7 h].

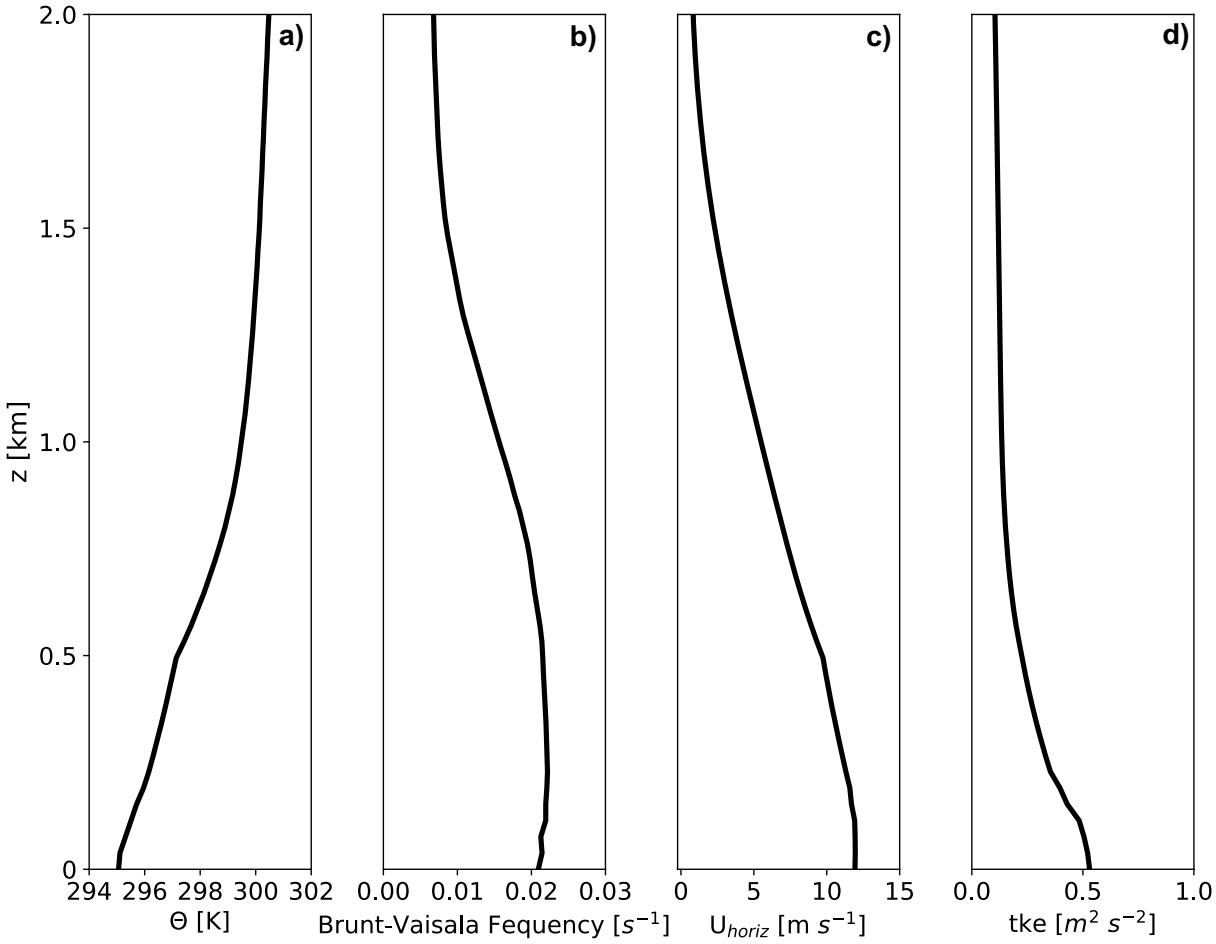

Fig. 4.3: Time and y-averaged vertical profiles of a) potential temperature (θ) (K), b) Brunt-Vaisala Frequency (s^{-1}), c) horizontal velocity (U_{horiz}) (m s^{-1}), and d) resolved *TKE* (m^2 s^{-2}) for the inner domain (d02) from the post- spin-up time interval [6 - 7 h].

4.3.2 Experimental Design

Microburst outflow boundaries generated by the WRF-LES simulations described above propagate horizontally and interact with canyons placed downwind of where the downdraft impinges onto the surface. To investigate and contrast changes in wind and turbulence by differing canyon types, simulations are run for both short- (~1.5 to 4.5 km) and long-distance canyons (~3 to 6 km) (Table 4.2).

For the short-distance canyons, two sets of simulations are conducted each with two north-south oriented mountains creating a west-east oriented canyon between them (Fig. 4.4). In one short-canyon (SC) simulation, the mountains are 6 km long with 10° slopes on each side creating a 3-km wide and 3-km long canyon (referred to as 10°SC) (Fig. 4.4a-b). In the second set of simulations, mountains are 3 km long and 1.5 km wide with 30° slope angles creating a canyon 1.5 km long and 0.5 km wide (referred to as 30°SC) (Fig. 4.4c-d). Both slope scenarios feature a maximum crest height of 250 m, and a length of ~1.5 km across each flat portion of the ridgeline. The horizontal width of the entire ridgeline in the x-direction is ~4.8 km for 10°SC, and ~1.2 km for 30°SC. The distance from the canyon floor to the top of the ridgeline is ~2.5 km for 10°SC (Fig. 4.4a-b), and ~0.8 km for 30°SC (Fig. 4.4c-d). The chosen terrain slopes of 10° and 30° are consistent with typical practical scenarios that were considered in previous experimental studies on the effects of terrain slope on fire spread rate (Sharples 2008; Dupuy et al. 2011; Liu et al. 2014).

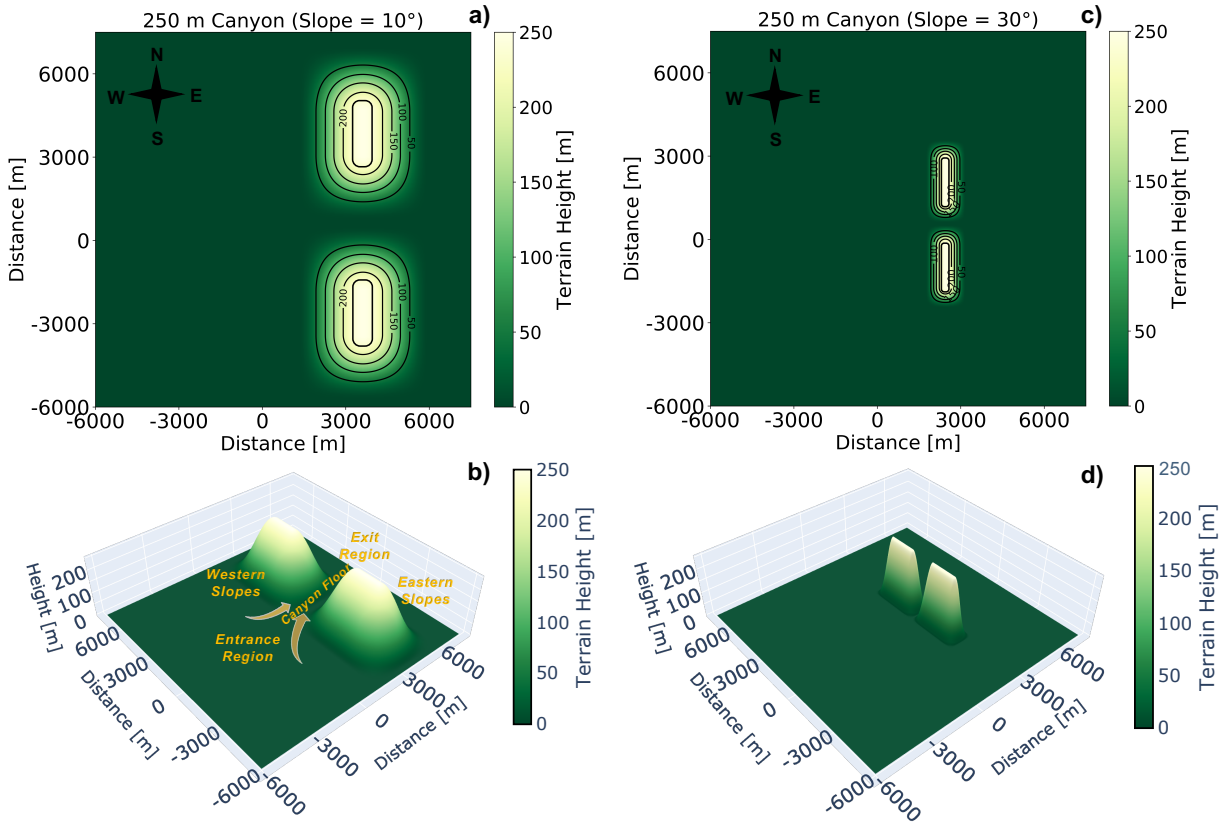

Fig. 4.4: a,c) Planar and b,d) three-dimensional views of the topography used in the short canyon simulations with 10° slope (a-b) and 30° slope (c-d).

For the long-canyon (LC) scenario, we use the same mountains as in the SC simulations, but rotate them by 90° so that the long-side is now oriented in the east-west direction (Fig. 4.5). By rotating the mountains, the canyon is now 6.5 km long and 3 km wide for the mountains with the 10° slope (referred to as 10°LC; Fig. 4.5a-b) and 3 km long and 1.5 km wide for the mountains with a 30° slope (referred to as 30°LC; Fig. 4.5c-d). In each canyon simulation, we refer to the entrance region as the location where the outflow boundary first enters the canyon on the west side, and the exit region where the boundary leaves the canyon on the east side (Fig. 4.5b).

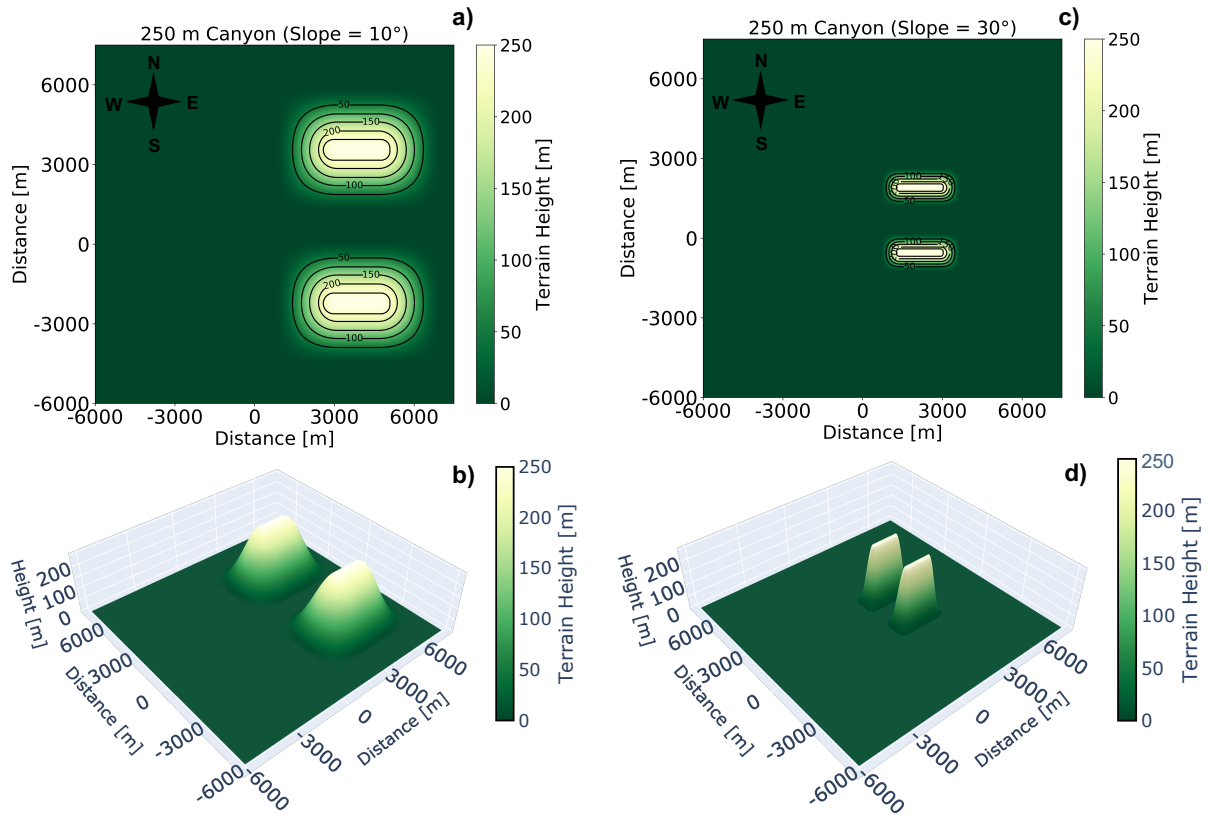

Fig. 4.5: As Fig. 4.4, but for the long canyon simulations.

To study the interactions between microburst wind speed and canyon types, the four canyon simulations (10°SC, 30°SC, 10°LC, 30°LC) are run with a i) microburst placed near or west of the canyon entrance so that the maximum magnitude in near-surface horizontal outflow boundary winds (U_{max}) occurs at the canyon entrances (also short-distance microburst or SDM simulations) and ii) a microburst placed farther west and away from the canyon entrance (or long-distance microburst or LDM simulations). To determine U_{max}, a baseline (BL) simulation of an isolated microburst over flat terrain (0°BL) is run with the microburst placed at x = 6.7 km and y = 6.7 km in the center of the inner domain (d02). U_{max} occurs 1.3 km from the center of the downdraft. Therefore, in the SD simulations with the four canyon types (SDM10°SC, SDM30°SC, SDM10°LC, SDM30°LC) the canyon entrance is placed 1.3 km from the center of

the microburst or at x = 8 km. For the LD simulations with the four canyon types (LDM10°SC, LDM30°SC, LDM10°LC, LDM30°LC) the microburst is placed 3.3 km (at x = 4.7 km) from the canyon entrance at x = 8 km. To summarize, a total of eight canyon simulations and two baseline simulations (SDM0°BL ; LDM0°BL) were conducted (Table 4.2).

Table 4.2: Simulation terrain setup including canyon type, canyon slope (°), and microburst location with respect to the terrain.

Simulation	*Canyon Type*	*Canyon Slope*	*Microburst Location*
SDM10°SC	Short	10°	Short-Distance
SDM30°SC	Short	30°	Short-Distance
LDM10°SC	Short	10°	Long-Distance
LDM30°SC	Short	30°	Long-Distance
SDM10°LC	Long	10°	Short-Distance
SDM30°LC	Long	30°	Short-Distance
LDM10°LC	Long	10°	Long-Distance
LDM30°LC	Long	30°	Long-Distance
SDM0°BL	Flat Terrain	0°	Short-Distance
LDM0°BL	Flat Terrain	0°	Long-Distance

To visualize the role of the terrain on wind speed changes, we calculate the spatial differences in horizontal wind speed at 10 m AGL, vertical velocity at 50 m, and *TKE* at 10 m between the respective baseline (SDM0°BL, LDM0°BL) simulation and the eight canyon simulations. Additionally, we calculate the overall maximum differences in horizontal wind speed, upward vertical velocity, and *TKE* between the baseline and canyon simulations over all time steps observed along the canyon floor (0 m) and canyon walls across the 50, 150, and 250 m contour isolines in the west-east direction. For example, in the 10°SC (Fig. 4.4a-b), the maxima are derived along the center of the canyon floor (0 m) at y = 6.7 km between 8 km < x < 11.5 km, along the northern (southern) mountain 50 m contour isoline at y = 7.3 km (5.8 km) between 8.7

km < x < 10.7 km, along the northern (southern) mountain 150 m contour isoline at y = 8 km (5.1 km) between 9.2 km < x < 10.2 km, and along the northern (southern) mountain 250 m contour isoline at y = 8.7 km (4.4 km) between 9.4 km < x < 9.9 km (Fig. 4.6). This method is applied to all canyon simulations, by taking west-east cross-sections of maximum differences along each isoline elevation (0, 50, 150, and 250 m) during the entire duration of the simulations.

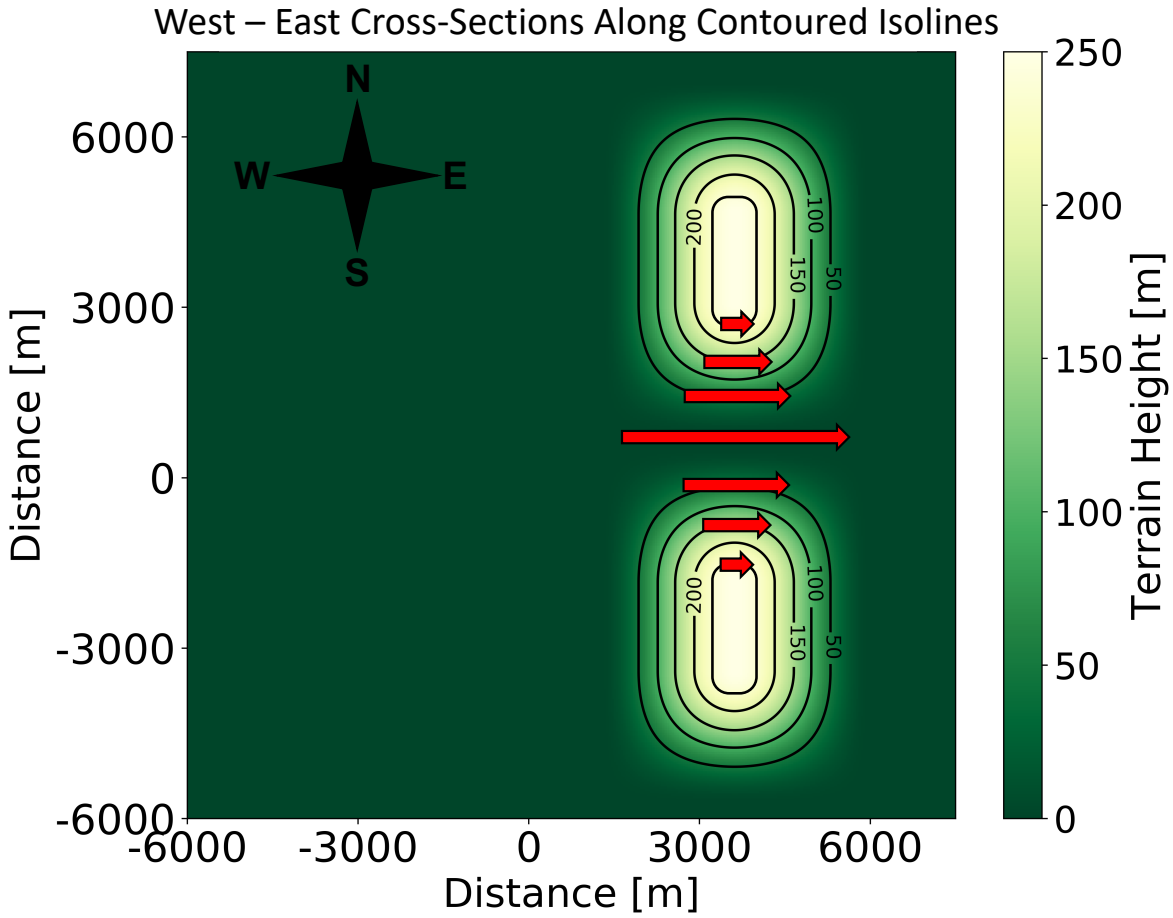

Fig. 4.6: Example of west-east cross-sections along each isoline elevation (0, 50, 150, and 250 m) in the 10°SC simulation (red arrows). Maximum differences of horizontal wind speed (m s^{-1}), upward vertical velocity (m s^{-1}), and *TKE* (m^2 s^{-2}) between the baseline and canyon simulations are calculated along each west-each cross-section during the duration of the outflow boundary's interaction with the canyon.

In addition to the west-east horizontal cross-sections, we calculate a topographic multiplier (M_t) to quantify wind enhancement due to topography (Mason et al. 2007, 2010). M_t profiles are the ratio of the horizontal wind speed at a specific height, z, above the canyon, to the wind speed at the same height in the baseline simulation, i.e., simulation without topography. The purpose of M_t is to quantify the increase or decrease in the horizontal wind speed for flow over canyons, by normalizing it against the horizontal wind speed for flow in the 0°BL simulations. For all eight canyon simulations, we calculate the maximum M_t across the west-east cross-sections at 0, 50, 150, and 250 m isolines across all time steps using:

$$M_t(z) = \frac{U(z)_{canyon}}{U(z)_{0°BL}} \qquad (4.1)$$

where $U(z)_{canyon}$ is the horizontal wind speed ($(u^2 + v^2)^{1/2}$) at a height, z, above the canyon, u and v are the horizontal wind components, and $U(z)_{0°BL}$ is the horizontal wind speed at the same height above a flat surface (0°BL) at the same location. Since microburst outflow winds are generally strongest near the surface, here we calculate M_t values at the lowest model level which is nominally at z = 10 m AGL.

4.4 Results

4.4.1 Baseline Simulation

The baseline simulation entails an isolated microburst and associated outflow boundary over flat terrain placed in the center of the inner domain (d02). After the cold bubble perturbation is introduced, the resulting downdraft has a diameter of ~1 km and a maximum downdraft speed, w_{max}, of -31 m s^{-1}, consistent with observations of microbursts in dry regions which are typically

< 4 km in diameter and feature downdrafts speeds as high as 30 m s^{-1} (Fujita and Wakimoto 1983; Wilson et al. 1984; Fujita 1985). When the descending column of cold air reaches the surface, the flow diverges horizontally away from where the downdraft impinges on the surface (Fig. 4.7a-c). The westward moving part of the outflow boundary encounters an ambient 15 m s^{-1} headwind from the west which induces a ring-like vortex feature that extends vertically to ~750 m AGL (Fig. 4.7b). The ambient headwind decelerates the westward movement of the outflow boundary, confining it close to the downdraft throughout the duration of the simulation. In contrast, the eastward moving horizontal outflow boundary encounters a tailwind, which helps to accelerate it away from the downdraft. However, the eastward moving outflow boundary does not feature a ring-like vortex along the leading edge, likely due to less convergence with the ambient wind field. This is reflected in the vertical velocity field depicted in Fig. 4.7a, where the upward vertical motion is weaker (~1 m s^{-1}) along the leading edge of the eastward moving outflow boundary, compared to the westward moving outflow boundary where convergence with the westerly ambient wind field enhances upward vertical motion along the boundary to > 5 m s^{-1}. Note that the circular outward fanning of outflow boundary winds from the center of the microburst shown in Fig. 4.7a is typical of microbursts observed in flat terrain regions (Fujita 1985). The near-surface horizontal winds accelerate to a maximum magnitude of U_{max} = 37 m s^{-1} at an elevation of z = 10 m within the eastward moving outflow boundary (Fig. 4.7c). Moving from the center of the downdraft towards the east, U_{max} occurs at ~1.3 km from the downdraft at x = 8 km, beyond which, the horizontal wind velocities behind the boundary drop-off rapidly as the cold air outflow entrains warmer ambient air ahead of the boundary.

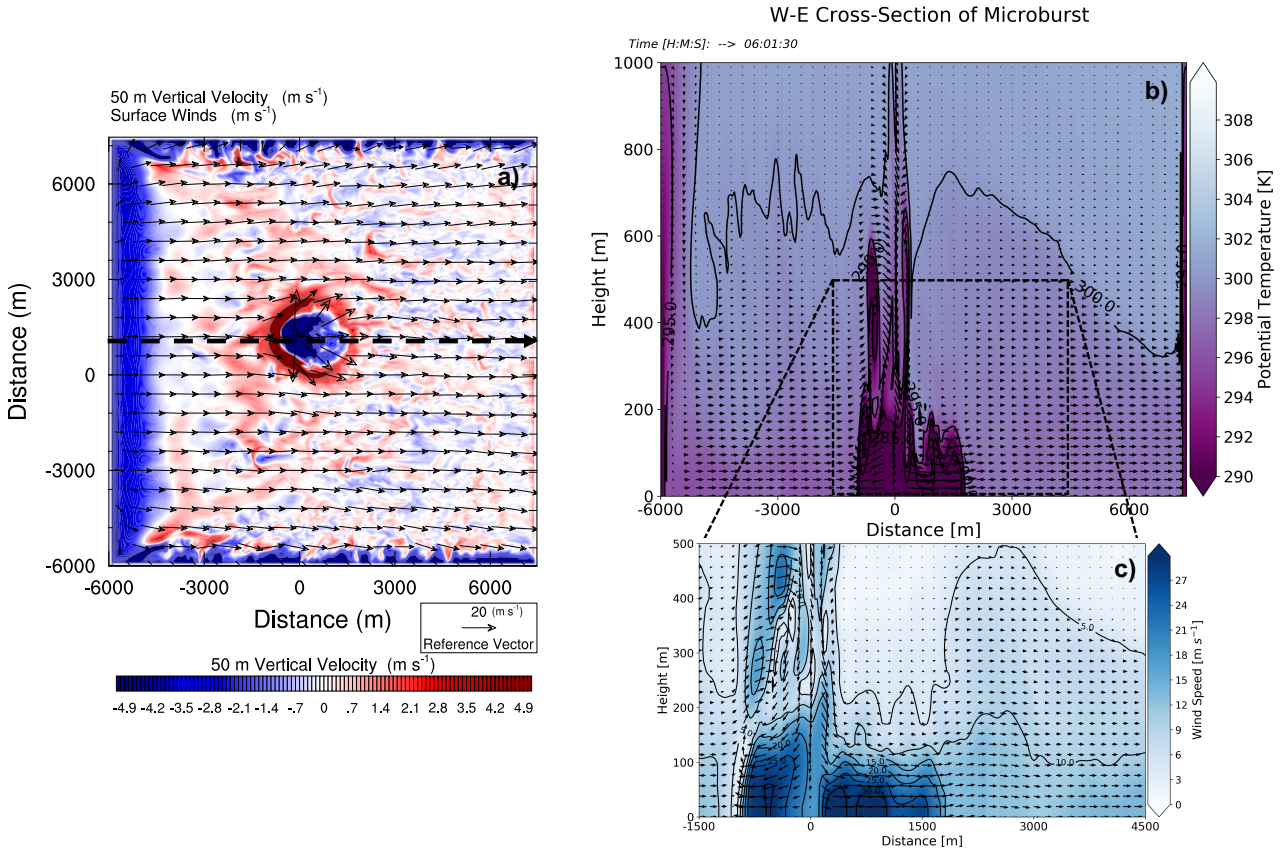

Fig. 4.7: Baseline simulation microburst structure at time of maximum horizontal winds (*Umax*) (t = 361 min and 30 s). a) Vertical velocity (m s^{-1}; color-coded) at 50 m AGL (filled colors) and horizontal wind (m s^{-1}; arrows) at the surface. A west-east cross section at y = 6.7 km (black dashed arrow in a) is shown in b-c) with potential temperature (K; color-coded) in b) and magnitude of horizontal wind speed (m s^{-1}; color-coded and contours) in c). Vectors show winds in the x-z plane .

4.4.2 Short Canyon Simulations

4.4.2.1 Short-Distance Microburst

According to density current theory, the larger the temperature difference between the cold air of the density current and the warmer environmental air, the stronger the difference in wind speeds across the different air masses (Benjamin 1968; Simpson and Britter 1980; Jorgensen et al. 2003). Since outflow boundaries often behave like density currents (Charba 1974; Sasaki and

Baxter 1986; Friedrich et al. 2005), horizontal winds across the leading edge of the boundary are typically strongest when the boundary is closer to the cold downdraft. In this section, we investigate short-distance microburst wind and turbulence in short canyons with slopes of the 10° and 30° (SDM10°SC and SDM30°SC). Here we describe and compare each simulation while comparisons to the long-distance microburst can be found in section 4.3.4.

The outflow boundary in SDM30°SC propagates faster through the canyon and over the mountains and shows stronger increases in wind, upward vertical velocity, and turbulence (*TKE*) compared to SDM10°SC. Three minutes after the microburst is initialized in SDM10°SC, the leading edge of the outflow boundary begins to propagate through the canyon and ride up the west-facing slopes and the north- and south-facing canyon walls (Fig. 4.8a, c, e). In contrast, at this same time step, the outflow boundary in SDM30°SC has already exited the canyon and reached the crest of both mountains (Fig. 4.8b, d, f). Compared to SDM0°BL, horizontal wind speed is stronger at the exit region on the east side of the canyon (by ~6 m s^{-1}) and atop the crest of the northern mountain (by ~7 m s^{-1}) in SDM30°SC (Fig. 4.8b). Along the southern mountain's west-facing slope, however, the increase in horizontal winds is weaker (by ~2-3 m s^{-1}) compared to the SDM0°BL. In the SDM10°SC, only slightly stronger horizontal winds (~2 m s^{-1}) are observed compared to SDM0°BL (Fig. 4.8a). Upward vertical velocity is stronger along the west-facing slopes and the north- and south-facing canyon walls in both SDM10°SC and SDM30°SC compared to SDM0°BL. However, the increase in upward vertical velocity is considerably higher in SDM30°SC (~8 m s^{-1}) compared to SDM10°SC (~2 to 3 m s^{-1}) (Fig. 4.8c-d). Note that the stronger upward vertical velocity is confined to the west-facing slopes and canyon walls with little to no enhancement within and along the canyon floors of both simulations. Similarly, *TKE* is stronger along the SDM30°SC walls, crest, and eastern slope of

the northern mountain (differences in *TKE* ~6 to 7 m^2 s^{-2}) compared to the *TKE* observed along the SDM10°SC canyon walls and west-facing slopes (~0.5 to 1 m^2 s^{-2}). Furthermore, little to no increase in *TKE* is observed along the canyon floors in either SDM10°SC and SDM30°SC simulations compared to SDM0°BL (Fig. 4.8e-f).

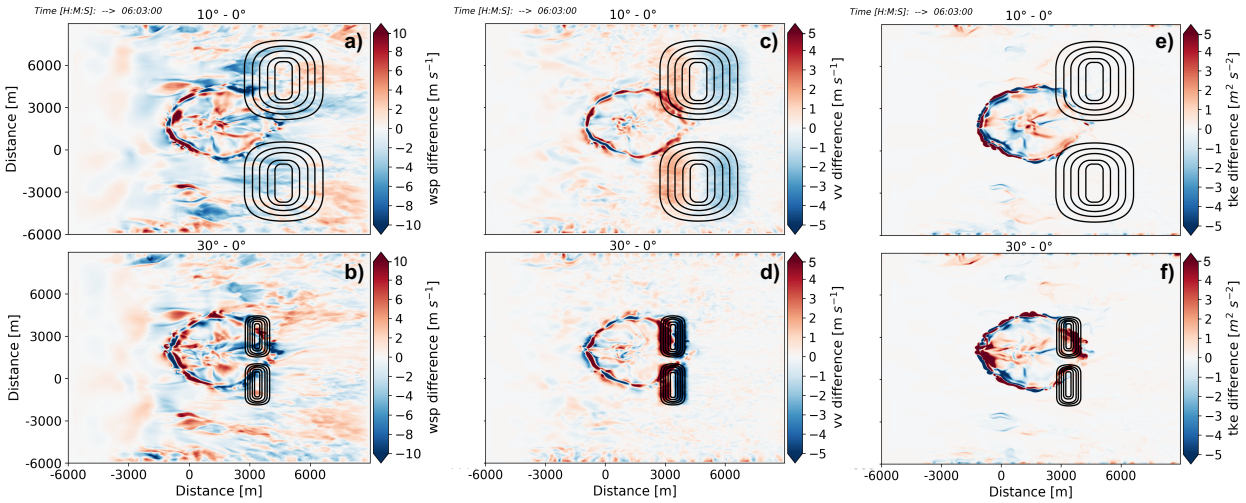

Fig. 4.8: Differences in wind speed between the 10° slope and the baseline simulation (top panels) and 30° slope and the baseline simulation (0°) (bottom panels) for the short canyon simulations with the microburst at close distance with a-b) horizontal wind speed differences (wsp; m s^{-1}) at z = 10m c-d), vertical velocity differences (vv; m s^{-1}) at z = 50 m, and e-f) turbulent kinetic energy difference (*TKE*; m^2 s^{-2}) at z = 10 m after 363 min into the simulation. Terrain is indicated by black lines with 50 m terrain contours.

Two minutes later (i.e., 5 minutes after the microburst is initialized), the outflow boundary in SDM10°SC reaches the crest of both mountains and the leading edge has passed through the canyon floor (Fig. 4.9a, c, e). In contrast, the outflow boundary in SDM30°SC has passed the canyon and mountains (Fig. 4.9b, d, e). As such, the horizontal wind, vertical velocity, and *TKE* along the leading edge of the outflow boundary are no longer influenced by the terrain. However, strong upward and downward vertical velocity is still observed along the western and eastern slopes in SDM30°SC (Fig. 4.9d), highlighting the impact of slopes on vertical motion for

even after the outflow boundary passed. In SDM10°SC, the horizontal winds at the canyon floor's exit region and along the north- and south-facing canyon walls are up to ~5 m s^{-1} higher compared to SDM0°BL (Fig. 4.9a). Little to no increase in upward vertical velocity (< 0.5 m s^{-1}) is observed along the SDM10°SC canyon floor (Fig. 4.9c). However, along the west-facing slopes, canyon walls, and crests of both the northern and southern mountains, upward vertical motion increases by up to ~4 m s^{-1} along the outflow boundary. Similarly, stronger *TKE* is observed up to ~5 m^2 s^{-2} along both north- and south-facing SDM10°SC walls and west-facing slopes, with little to no increase observed along the canyon's floor.

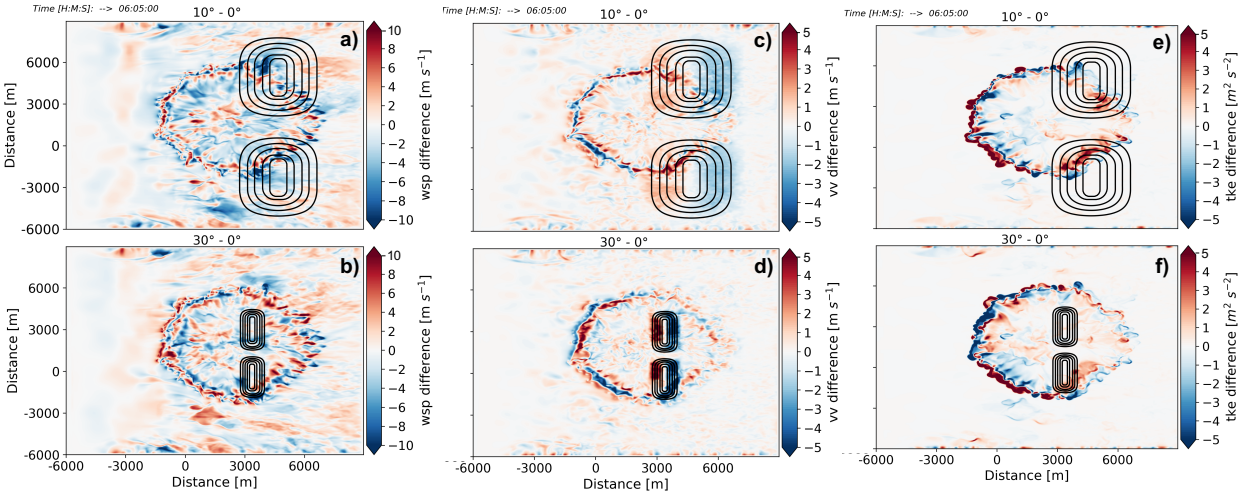

Fig. 4.9: As Fig. 4.8, but at t = 365 min from the start of the simulations.

4.4.2.2 Long-Distance Microburst

As outflow boundaries displace farther from their source of cold air, the winds along the boundary typically diminish according to density current theory. In this section, we investigate wind and turbulence at ridges and canyons if the microburst occurs at farther distances from the terrain (LDM10°SC, LDM30°SC). Here, the center of the microburst downdraft is moved to 3.3 km from that canyon entrance at x = 4.7 km.

Contrary to the short-distance microburst simulations, the outflow boundary in LDM30°SC propagates only slightly faster through the canyon and over the mountains and with similar magnitude increases in horizontal winds compared to LDM10°SC. Four minutes and 30 seconds after the microburst is initialized, the outflow boundary reaches the west-facing slopes of the LDM10°SC and propagates almost halfway through the canyon (Fig. 4.10a, c, e). At the same time step, the outflow boundary in LDM30°SC reaches the crest of both mountains, and has almost passed through the canyon (Fig. 4.10b, d, f). Weak increases in horizontal winds are observed along the LDM10°SC (~3 to 4 m s^{-1}) and LDM30°SC canyon floors (~3 to 4 m s^{-1}) compared to LDM0°BL (Fig. 4.10a-b). Additionally, horizontal winds increase (~3-4 m s^{-1}) atop the crest and east-facing slopes of the northern LDM30°SC mountain. However, the increase in horizontal winds is slightly weaker (~2-3 m s^{-1}) along the west-facing slopes of the southern mountain at this time. In LDM10°SC , little increase in horizontal wind is observed along the canyon walls and west-facing slopes (< 2 m s^{-1}) compared to LDM0°BL. Stronger upward vertical velocity is observed along the west-facing slopes and canyon walls in both LDM10°SC (1~2 m s^{-1}) and LDM30°SC (~5 m s^{-1}) compared to LDM0°BL, but with little to no enhancement (< 0.5 m s^{-1}) along either canyons' floor (Fig. 4.10c-d). Similarly, *TKE* is solely enhanced atop the western slope and crest of the LDM30°SC northern mountain (~4 m^2 s^{-2}), yet negligible enhancement (< 0.5 m^2 s^{-2}) is observed along the canyon walls, floor, and southern mountain (Fig. 4.10f). For LDM10°SC, *TKE* negligibly increases (~0.5 to 1 m^2 s^{-2}) near the lower north-facing wall of the southern mountain, with little enhancement elsewhere (< 0.5 m^2 s^{-2}) (Fig. 4.10e).

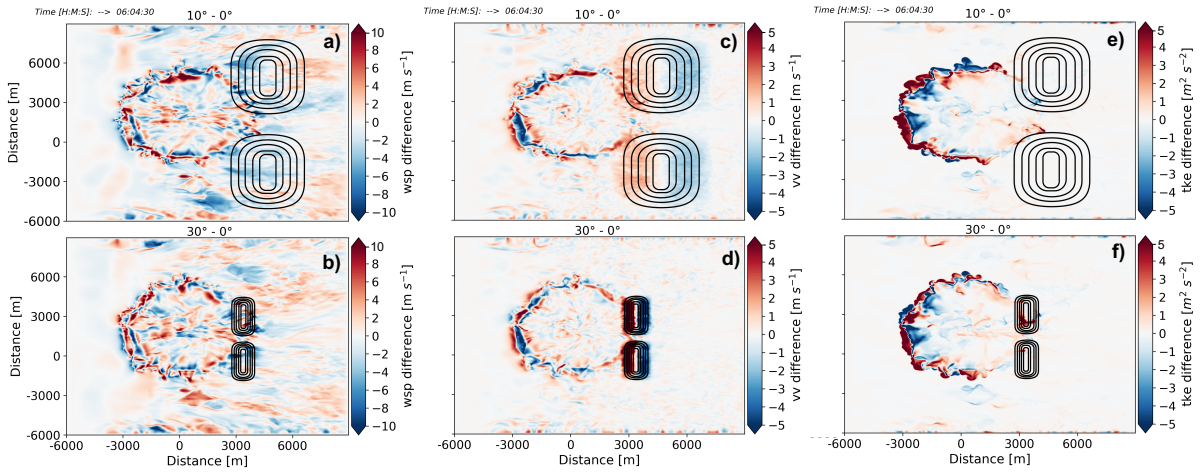

Fig. 4.10: As Fig. 4.8, but at t = 364 min and 30 s with the canyons centered farther away from the microburst (long distance simulations).

A few minutes later (*t* = 6 min and 30 s), the outflow boundary has reached the crests of both mountains and the canyon exit region in LDM10°SC (Fig. 4.11a, c, e). In contrast, the LDM30°SC outflow boundary has passed the mountains and canyon at this time step (Fig. 4.11b, d, e). Similar to the short-distance microburst simulation, strong upward and downward vertical winds (> 5 m s^{-1}) are still observed along both western and eastern slopes in LDM30°SC after the outflow boundary passed the terrain. Horizontal winds are slightly stronger (by ~3 to 4 m s^{-1}) at the exit region of the LDM10°SC, as well as along portions of the canyon walls compared to LDM0°BL (Fig. 4.11a). Similarly, upward vertical motion is stronger by ~2 to 3 m s^{-1} along the west-facing slopes and walls of both the northern and southern LDM10°SC mountains, but less so along the canyon floor (<1 m s^{-1}) (Fig. 4.11c compared to LDM0°BL). Lastly, the increase in *TKE* between the LDM0°BL and LDM10°SC simulations is ~0.5 to 1 m^2 s^{-2} within and along the floor and walls at this time step (Fig. 4.11e).

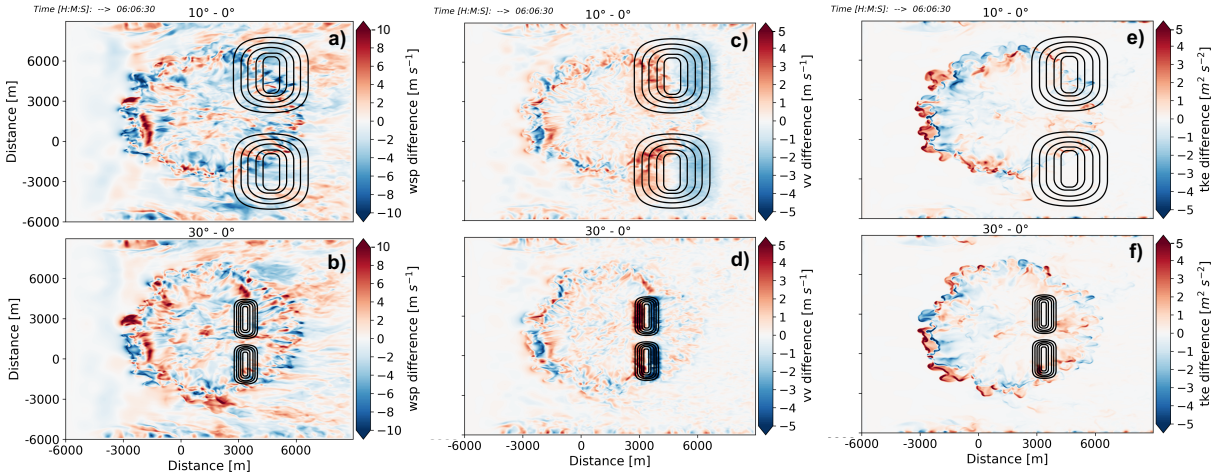

Fig. 4.11: As Fig. 4.8, but at t = 366 min and 30 s with the canyons centered farther away from the microburst (long distance simulations).

4.4.3 Long Canyon Simulations

4.4.3.1 Short-Distance Microburst

Here, we investigate an outflow boundary that passes through horizontally longer canyons (~3 to 6 km) from a microburst that developed at a close distance (1.3 km from the west-facing slopes of the canyons) (SDM10°LC and SDM30°LC).

The outflow boundary in SDM30°LC propagates faster through the canyon and over the ridges compared to SDM10°LC and shows slightly stronger increases in winds (5 to 7 m s^{-1}), upward vertical velocity (4 to 6 m s^{-1}), and *TKE* (4 to 6 m^2 s^{-2}*)* compared to SDM10°SC (5 to 6 m s^{-1}; 3 to 5 m s^{-1}; 3 to 5 m^2 s^{-2}). Three minutes after the microburst is initialized, the leading edge of the outflow boundary has reached the lowest levels of the west-facing slopes and entrance region of SDM10°LC (Fig. 4.12a, c, e). In contrast, the outflow boundary in

SDM30°LC has crested both northern and southern mountains and has nearly reached the middle of the canyon (Fig. 4.12b, d, f). Strong increases in horizontal wind speed (by ~6 m s^{-1}) are observed at the entrance region and lower walls of the south-facing slope in SDM10°LC (Fig. 4.12a). In contrast, increases in horizontal wind speed (~4 m s^{-1}) are weaker in the entrance region and within the SDM30°LC compared to SDM10°LC (Fig. 4.12b). Increased upward vertical velocity is observed along the west-facing slopes with the magnitude increase considerably higher in SDM30°LC (~6 m s^{-1}) compared to SDM10°LC (~2 to 3 m s^{-1}) (Fig. 4.12c-d). Note that similar to the short canyon simulations, the strongest upward vertical velocity enhancement is confined to the canyon walls with little to no enhancement (< 1 m s^{-1}) within the canyon floors in both SDM30°LC and SDM10°LC. Similarly, increases in *TKE* are considerably stronger along the SDM30°LC walls and crests (~6 m^2 s^{-2}) compared to along the west-facing slopes and entrance region in SDM10°LC (~1 to 2 m^2 s^{-2}). In SDM30°LC, no increase in *TKE* is observed along the canyon floor. However, little increase in *TKE* (~1 to 2 m^2 s^{-2}) is observed at the entrance region of the canyon floor in SDM10°LC (Fig. 4.12e-f).

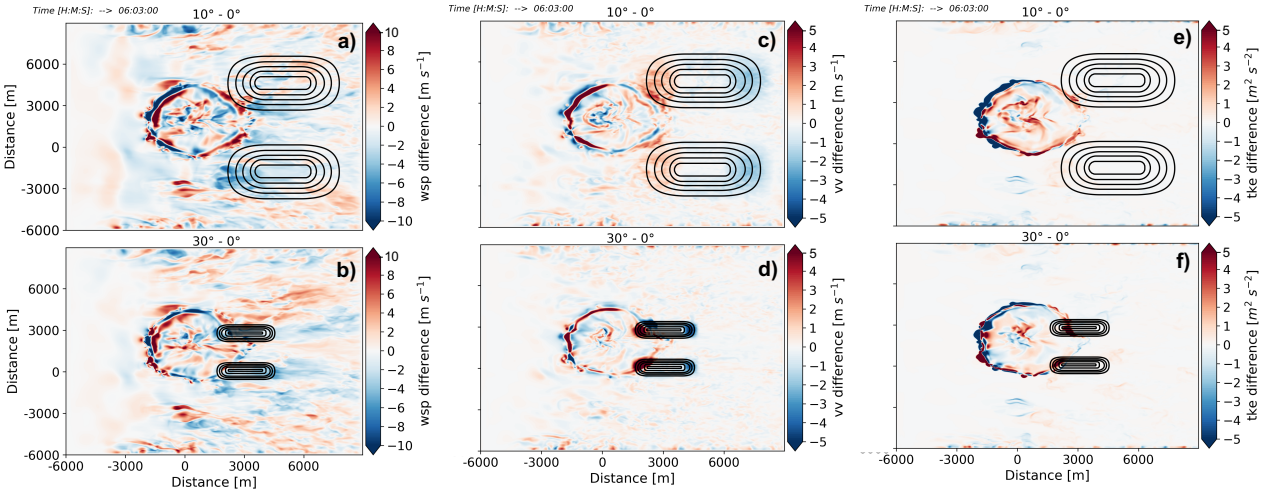

Fig. 4.12: Differences in wind speed between the 10° slope and the baseline simulation (top panels) and 30° slope and the baseline simulation (0°) (bottom panels) for the long canyon simulations with the microburst at close distance with a-b) horizontal wind speed differences (m s^{-1}) at z = 10 m c-d), vertical velocity differences (m s^{-1}) at z = 50 m, and e-f) turbulent kinetic energy difference (*TKE*; m^2 s^{-2}) at z = 10 m after 363 min into the simulation. Terrain is indicated by black lines with 50 m terrain contours.

Two minutes later (i.e. 5 minutes after the microburst is initialized), the outflow boundary in SDM10°LC reaches the crest of both mountains and the middle of the canyon (Fig. 4.13a, c, e). In contrast, the outflow boundary in SDM30°LC reaches the exit region at this time (Fig. 4.13b, d, e). In SDM10°LC, the horizontal winds increase by up to ~5 to 6 m s^{-1} in the middle of the canyon floor, along the crest of the northern mountain, and near the upper west-facing slopes of the southern mountain (Fig. 4.13a). Similarly in SDM30°LC, strong increases in horizontal winds (~5 to 7 m s^{-1}) are observed in the exit region. However, no increases in horizontal winds occur along the crests and canyon walls (Fig. 4.13b). In SDM10°LC, strong increases in upward vertical velocity of ~5 m s^{-1} are observed along the west-facing slopes and upper walls of the south-facing canyon walls (Fig. 4.13c). In the SDM30°LC, however, minimal increase in upward vertical velocity (< 1 m s^{-1} at the canyon floor's exit region) is observed along the

leading edge of the outflow boundary (Fig. 4.13). Note that similar to the short-canyon simulations, residual post-boundary strong upward and downward vertical velocities are still possible along the western and eastern slopes as shown in SDM30°LC. In SDM10°LC, an increase in *TKE* (~5 m^2 s^{-2}) is observed along both the north- and south-facing canyon walls, as well as along the middle of the canyon (~3 m^2 s^{-2}) (Fig. 4.13e). In SDM30°LC, little increase in *TKE* (~1 - 2 m^2 s^{-2}) is observed in the exit region (Fig. 4.13f). Additionally, along the crest and eastern slopes of the SDM30°LC southern and northern mountains, *TKE* also increases by up to ~5 to 6 m^2 s^{-2} behind the exiting outflow boundary.

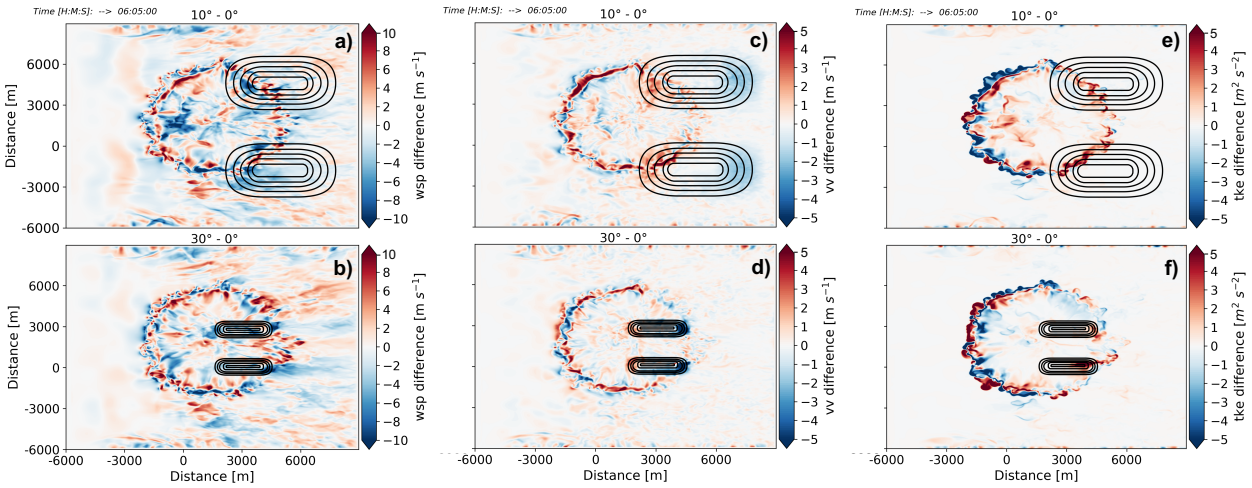

Fig. 4.13: As Fig. 4.12, but at t = 365 min from the start of the simulations.

4.4.3.2 Long-Distance Microburst

Here, we investigate long-canyon influence on a microburst outflow boundary that is generated 3.3 km from the canyon entrance (LDM10°LC and LDM30°LC).

Although the outflow boundary in LDM30°LC propagates faster through the canyon and over the mountains compared to LDM10°SC, the increase in horizontal winds is actually weaker in

LDM30°LC compared to LDM10°LC. Four minutes and 30 seconds after the microburst is initialized, in LDM10°LC the outflow boundary reaches the entrance region (Fig. 4.14a, c, e). Conversely, the outflow boundary in LDM30°LC reaches the west-facing slopes and crests of both southern and northern mountains and nears the middle of the canyon floor at this time (Fig. 4.14b, d, f). Weak increases in horizontal winds are observed along the canyon floor in both LDM10°LC (~3 to 4 m s^{-1}) and LDM30°LC (~2 to 3 m s^{-1}), with little to no (< 0.5 m s^{-1}) increase in horizontal winds elsewhere in either simulation (Fig. 4.14a-b). Upward vertical velocity is stronger along the west-facing slopes and canyon walls in LDM30°LC (~5 m s^{-1}) compared to the western slopes and entrance region in LDM10°LC (~1 to 3 m s^{-1}) (Fig. 4.14c-d). Similarly, in LDM30°LC, weak increases in *TKE* occur on the crest of the northern mountain (~2 to 3 m^2 s^{-2}) with no increase in *TKE* along the outflow boundary elsewhere along the walls and canyon (Fig. 4.14f). Conversely, in LDM10°LC, *TKE* negligibly increases (~0.5 to 1 m^2 s^{-2}) within the entrance region of the canyon (Fig. 4.14e).

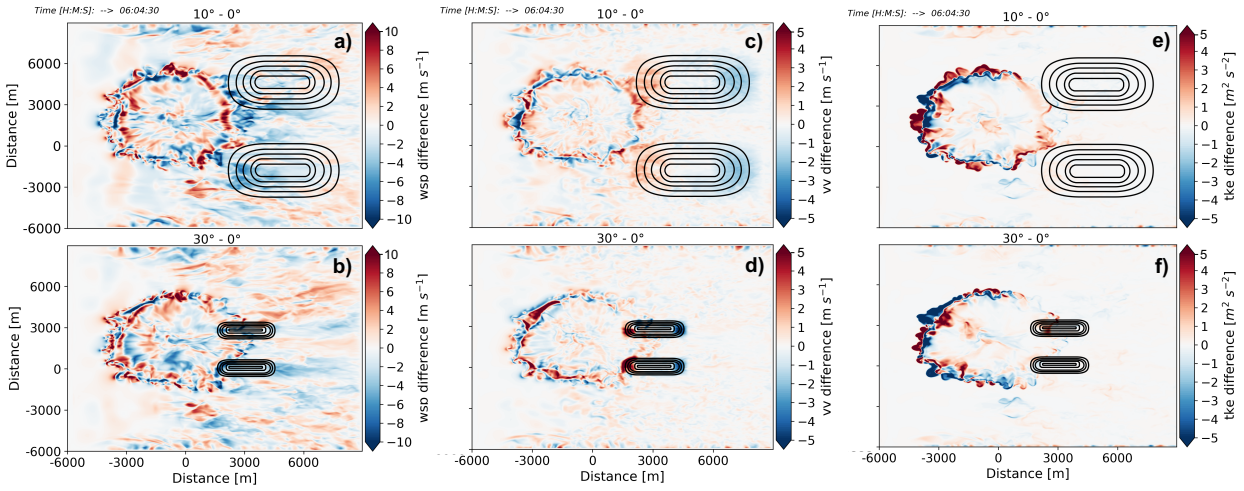

Fig. 4.14: As Fig. 4.12, but at t = 364 min and 30 s with the canyons centered farther away from the microburst (long distance simulations).

A few minutes later (t = 6 min and 30 seconds after the microburst is initialized), the outflow boundary in LDM10°LC has reached the upper part of the south- and north-facing canyon walls, and has neared the middle of the canyon (Fig. 4.15a, c, e). Conversely, in LDM30°LC the outflow boundary has mostly cleared past the mountains and canyon at this time (Fig. 4.15b, d, e). Other than some weak residual increase in horizontal winds (~3 to 4 m s^{-1}) within the exit region in LDM30°LC, and some post-boundary upward and downward vertical velocities along the western and eastern slopes, the terrain in LDM30°LC no longer affects the leading edge of the outflow boundary (Fig. 4.15b, d, e). In contrast, in LDM10°LC, horizontal winds increase (by ~4 to 5 m s^{-1}) along the canyon floor, as well as along portions of the canyon walls (Fig. 4.15a). Similarly, in LDM10°LC, upward vertical velocity increases by up to ~3 to 4 m s^{-1} along the upper part of the west-facing slopes, but less so along the canyon floor (< 0.5 m s^{-1}) (Fig.

4.15c). Lastly, in LDM10°LC *TKE* negligibly increases by ~0.5 to 1 m^2 s^{-2} within and along the canyon floor and walls (Fig. 4.15e).

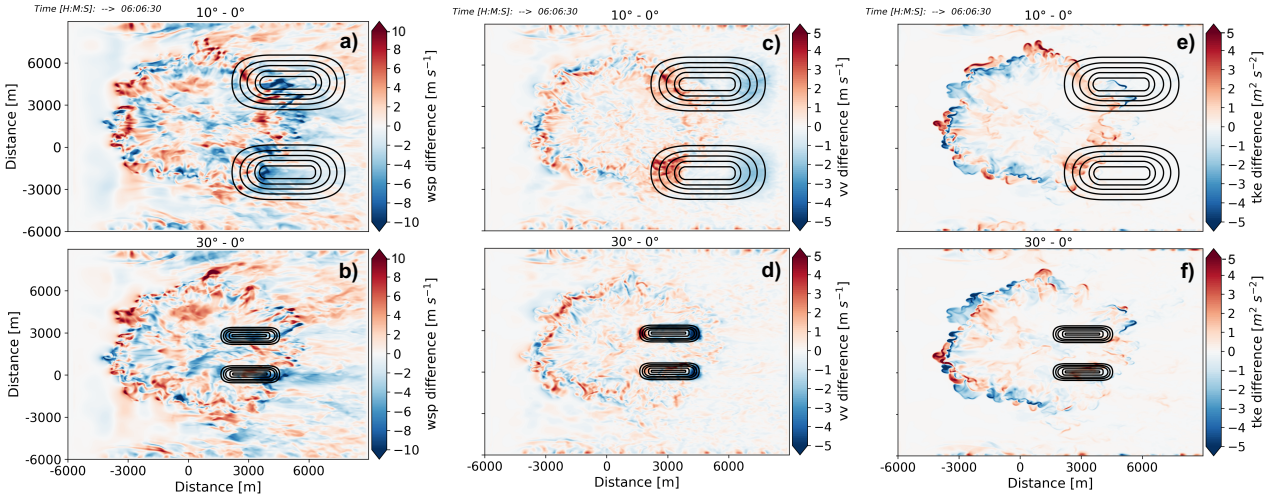

Fig. 4.15: As Fig. 4.12., but calculated at t = 366 min and 30 s with the canyons centered farther away from the microburst (long distance simulations).

4.4.4 Quantifying Wind and Turbulence Changes for All Microburst and Slope Scenarios

In both short- and long-distance canyon simulations, horizontal wind, upward vertical velocities, and *TKE* within the canyons as well as along the canyon walls are stronger when the microburst is closer to the canyons compared to when the microburst is farther from the canyons. To further illustrate these results, the maximum increase of each atmospheric variable during the microburst interaction with the canyons is calculated along west-east cross-sections following the contoured isolines at 0, 50, 150, and 250 m AGL (Table 4.3; Table 4.4). The values in Tables 2 and 3 represent the maximum increase in horizontal wind, upward vertical velocity, and *TKE* observed across each west-east cross-section for the duration of each canyon simulation when compared to 0°BL simulations.

Microbursts at short distance to the canyon are more impactful on short and long canyons compared to microbursts even just 2 km farther away from the canyons. The maximum increase in horizontal winds at 10 m AGL is stronger in the short-distance (1.3 km) microburst simulations (3.1 to 6.6 m s^{-1} in SDM10°SC and SDM30°SC; 3.4 to 6.9 m s^{-1} in SDM10°LC, SDM30°LC) compared to the long-distance (3.3 km) simulations (3.3 to 4.7 m s^{-1} in LDM10°SC and LDM30°SC; 2.4 to 5.7 m s^{-1} in LDM10°LC and LDM30°LC) (Tables 4.2-4.3). Similarly, the maximum increase in upward vertical velocity is stronger in the short-distance simulations (1.9 to 8.4 m s^{-1} in SDM10°SC and SDM30°SC; 3.8 to 6.4 m s^{-1} in SDM10°LC, SDM30°LC) compared to the long-distance simulations (1.7 to 5.3 m s^{-1} in LDM10°SC and LDM30°SC; 2.0 to 5.2 m s^{-1} in LDM10°LC and LDM30°LC). Lastly, the maximum increase in *TKE* is stronger in the short-distance simulations (1.2 to 6.6 m^2 s^{-2} in SDM10°SC and SDM30°SC; 1.4 to 6.8 m^2 s^{-2} in SDM10°LC, SDM30°LC) compared to the long-distance simulations (0.5 to 4.3 m^2 s^{-2} in LDM10°SC and LDM30°SC; 0.5 to 2.1 m^2 s^{-2} in LDM10°LC and LDM30°LC) (Tables 4.3-4.4). Since the difference between the location of the short- and long-distance microbursts is 2 km, a reduction in the increase in horizontal winds of 0.3 to 3.3 m s^{-1}, upward vertical velocity of 0.1 to 3.1 m s^{-1}, and *TKE* of 0.4 to 5.1 m^2 s^{-2} can be expected for every 2 km that the microburst is farther away from the canyons.

Table 4.3: Maximum differences between baseline (0°) and short distance canyon simulations (10° and 30° slopes) for short and far distance microbursts: horizontal wind speed (wsp) (m s^{-1}) at z = 10 m, vertical velocity (w) (m s^{-1}) at z = 50 m, and turbulence kinetic energy (TKE) (m^2 s^{-2}) at z = 10 m. Values are calculated along west-east horizontal cross-sections following the contoured isolines at 0, 50, 150, and 250 m AGL.

Short Canyon 1.3 km from microburst				Short Canyon 3.3 km from microburst			
	wsp ($m\ s^{-1}$)	*vv* ($m\ s^{-1}$)	*tke* ($m^2\ s^{-2}$)		*wsp* ($m\ s^{-1}$)	*vv* ($m\ s^{-1}$)	*tke* ($m^2\ s^{-2}$)
10° - 0 m	5.2	2.1	1.4	10° - 0 m	3.7	1.8	0.9
10° - 50 m	5.6	2.8	1.2	10° - 50 m	3.5	2.7	0.7
10° - 150 m	4.1	4.0	3.7	10° - 150 m	3.3	2.8	0.8
10° - 250 m	3.1	3.7	5.1	10° - 250 m	4.7	3.1	0.5
30° - 0 m	6.6	1.9	1.4	30° - 0 m	4.0	1.7	0.9
30° - 50 m	5.7	3.4	1.4	30° - 50 m	4.0	3.1	0.7
30° - 150 m	4.5	5.1	5.6	30° - 150 m	3.0	4.9	0.8
30° - 250 m	6.5	8.4	6.6	30° - 250 m	4.2	5.3	4.3

Table 4.4: As Table 4.3, but for the long-distance canyon simulations.

Long Canyon 1.3 km from microburst				Long Canyon 3.3 km from microburst			
	wsp ($m\ s^{-1}$)	*vv* ($m\ s^{-1}$)	*tke* ($m^2\ s^{-2}$)		*wsp* ($m\ s^{-1}$)	*vv* ($m\ s^{-1}$)	*tke* ($m^2\ s^{-2}$)
10° - 0 m	6.4	4.2	3.5	10° - 0 m	5.3	2.1	0.9
10° - 50 m	5.5	3.8	2.6	10° - 50 m	5.2	3.5	1.0
10° - 150 m	5.6	3.9	4.6	10° - 150 m	4.9	2.9	1.1
10° - 250 m	5.3	4.9	5.6	10° - 250 m	5.7	2.0	0.5
30° - 0 m	6.6	5.0	1.4	30° - 0 m	4.1	2.2	0.8
30° - 50 m	6.7	6.0	3.7	30° - 50 m	3.4	5.0	1.0
30° - 150 m	6.9	6.4	5.1	30° - 150 m	4.4	5.2	1.2
30° - 250 m	3.4	6.4	6.8	30° - 250 m	2.4	5.1	2.1

For the long-distance (3.3 km) simulations (LDM10°SC, LDM30°SC; LDM10°LC, LDM30°LC) the steepness of the canyon walls has less influence on horizontal wind and turbulence associated with the outflow boundary, compared to the short-distance (1.3 km) simulations (SDM10°SC, SDM30°SC; SDM10°LC, SDM30°LC) where horizontal wind, upward vertical velocity, and *TKE* generally increase more within the 30° sloped canyons compared to the 10° sloped canyons. In the short-distance microburst simulations, the maximum increase in horizontal wind, upward vertical velocity, and *TKE* is generally stronger within the 30°-sloped canyons (3.4 to 6.9 m s^{-1}; 1.9 to 8.4 m s^{-1}; 1.4 to 6.8 $m^2\ s^{-2}$ in SDM30°SC and SDM30°LC) compared to the 10°-sloped canyons (3.1 to 5.6 m s^{-1}; 2.1 to 4.9 m s^{-1}; 1.4 to 5.6

m^2 s^{-2} in SDM10°SC and SDM10°LC) (Tables 4.2-4.3). These results agree with other microburst studies that observed increasing topographic enhancement of microburst flow over hills and escarpments with increasing upslope steepness (Letchford and Illidge 1999; Wood et al. 2001; Mason et al. 2007, 2010). Since the difference in slope is 20°, a reduction in the increase in horizontal winds of 0.2 to 3.4 m s^{-1}, upward vertical velocity of 0.8 to 4.6 m s^{-1}, and *TKE* of 0.1 to 1.5 m^2 s^{-2} can be expected for every 20° decrease in canyon slope when the microburst is close to the canyons.

In the long-distance microburst simulations (microburst 3.3 km from canyons), however, differences in canyon slope steepness is not a strong determining factor on the increase in horizontal winds along the leading edge of outflow boundaries. Specifically, the maximum increase in horizontal winds are actually weaker within the 30°-sloped canyons (2.4 to 4.1 m s^{-1} in LDM30°SC and LDM30°LC) compared to the 10°-sloped canyons (3.3 to 5.7 m s^{-1} in LDM10°SC and LDM10°LC) (Tables 4.3-4.4). Conversely, the maximum increase in upward vertical velocity and *TKE* are slightly stronger within the 30°-sloped canyons (1.7 to 5.3 m s^{-1}; 0.7 to 4.3 m^2 s^{-2} in LDM30°SC and LDM30°LC) compared to the 10°-sloped canyons (1.8 to 3.5 m s^{-1}; 0.5 to 1.1 m^2 s^{-2} in LDM10°SC and LDM10°LC). Note, however, there is a strong outlier along the 250 m isoline in the LDM30°SC of 4.3 m^2 s^{-2}, without which, the differences in *TKE* between the 10°- and 30°-sloped canyons are more similar. Regardless, differences in canyon slope steepness have no influence on the increase in horizontal winds, but steeper slopes may lead to slightly stronger increases in upward vertical velocity and *TKE* along outflow boundaries from microbursts that initiate farther from the canyons.

Across all eight short- and long-canyon simulations, the location of the maximum increase in atmospheric parameters varies spatially depending on slope orientation and elevation. For

example, the increase in horizontal wind speed is generally strongest (> 3 to 5 m s^{-1}) at the lower levels of the canyon (0 – 50 m) (Tables 4.3-4.4), and is typically maximized towards the exit region of the canyon floors in both short- and long-distance simulations. This may be related to the narrow topography channeling the winds through the center and out the end of the canyons near the surface which is often observed in other studies of canyon effects on local winds (Goens and Andrews 1998; Brown 2002; Esperanza Investigation Team 2006; Coen and Riggan 2010; Sharples et al. 2010). Alternatively, the increase in upward vertical velocity is strongest along the upper part of the canyon walls and crests (Tables 4.3-4.4), and the peak upward vertical velocity was typically observed along the west-facing slopes. Similarly, the maximum increase in *TKE* was predominately stronger along the upper canyon walls and crests in both short- and long-distance simulations (note the only exception is in LDM10°SC) (Tables 4.3-4.4). These observations agree with other studies of turbulence and upward motion within narrow valleys where strong gradients in the mean flow results in significant shear production of *TKE* up the slope and at the crest of ridgelines (Mason et al. 2007 2010; Schmidli 2013).

4.4.5 Comparisons of Topographic Multiplier for Short and Long Canyons

For both short- and long-distance microburst simulations, the maximum M_t is also higher when the microburst is close to the canyons compared to when the microburst initiates farther from the canyons. Specifically, the maximum M_t is generally higher in the short- distance microburst simulations (wind speed increases of 18 to 53 % in SDM10°SC and SDM30°SC; 10 to 57 % in SDM10°LC and SDM30°LC) compared to the long-distance microburst simulations (12 to 30% in LDM10°SC and LDM30°SC; 6 to 31% in LDM10°LC and LDM30°LC) (Table

4.5). A reduction in maximum M_t of 4 to 32 % can therefore be expected for every 2 km that the microburst is farther away from the canyons.

Table 4.5: Maximum topographic multiplier (at z = 10 m) for simulated microburst flow over short and long canyons calculated along west-east horizontal cross-sections following the contoured isolines at 0, 50, 150, and 250 m AGL. The 2nd columns corresponds with simulations where the canyons were placed close to the downdraft (x = 1.3 km). The 3rd columns corresponds with simulations where the canyons were placed further from the downdraft (x = 3.3 km).

Short Canyons			**Long Canyons**		
Max Topographic Multiplier Across Entire Cross Section			Max Topographic Multiplier Across Entire Cross Section		
	x = 1.3 km	*x = 3.3 km*		*x = 1.3 km*	*x = 3.3 km*
10° - 0 m	1.26	1.14	10° - 0 m	1.48	1.23
10° - 50 m	1.36	1.16	10° - 50 m	1.36	1.26
10° - 150 m	1.32	1.24	10° - 150 m	1.37	1.31
10° - 250 m	1.18	1.30	10° - 250 m	1.42	1.27
30° - 0 m	1.42	1.16	30° - 0 m	1.46	1.25
30° - 50 m	1.36	1.18	30° - 50 m	1.46	1.20
30° - 150 m	1.38	1.12	30° - 150 m	1.57	1.25
30° - 250 m	1.53	1.26	30° - 250 m	1.10	1.06

In the short-distance microburst simulations (SDM10°SC, SDM30°SC; SDM10°LC, SDM30°LC), the steeper slopes along the canyon walls have a stronger influence on the maximum M_t compared to the long-distance microburst simulations (LDM10°SC, LDM30°SC; LDM10°LC, LDM30°LC) where steeper slopes do not result in higher maximum M_t. For the short-distance simulations, the maximum M_t is generally higher within the 30° canyons compared to the 10° canyons for both short (36 to 53 % SDM30°SC; 18 to 32% in SDM10°SC) and long distance (10 to 57% in SDM30°LC; 36 to 48% in SDM10°LC) canyons. The only exception is along the 250 m cross-section of the long canyons where the maximum M_t is higher in the SDM10°LC (42 % increase in wind speed) compared to the SDM30°LC (10 % increase in

wind speed). Elsewhere, a reduction in maximum M_t of 6 to 35 % can be expected for every 20° decrease in canyon slope when the microburst is close to the canyons.

In the long-distance simulations (3.3 km), however, the range of maximum M_t is comparable between 10° (14 to 30 % in LDM10°SC; 23 to 31% in LDM10°LC) and 30° (12 to 26 % in LDM30°SC; 6 to 25% in LDM30°LC) canyons (Table 4.5). These results re-iterate that when the microburst develops farther from the canyons, slope steepness is not a strong factor in determining the enhancement of horizontal outflow winds.

The maximum M_t across each west-east cross-section is almost always higher in the long-canyon simulations, compared to the short-canyon simulations (Table 4.5). These differences in maximum M_t may be related to differences in the orientation and length between the short- and long-distance canyons, which may determine their overall terrain-channeling potential. Since the maximum increase in horizontal winds is typically observed towards the canyon exit region in all simulations, terrain-channeling must be present and most effective as the outflow boundary reaches the exit region. In the short-canyon simulations, the average propagation speed of the leading edge of the outflow boundaries at the time they reach the canyon floor's exit region ranges between 17.7 and 23.3 m s^{-1}. Conversely, in the long-canyon simulations, the average propagation speed along the outflow boundaries at the canyon floor's exit region is slower between 14.2 and 17.5 m s^{-1}, likely due to an increase in drag along the horizontally longer mountains. Therefore, the long-canyons tend to slow down the advancing outflow boundaries, allowing for longer durations of canyon-channeling of horizontal winds compared to the short-canyons, where the boundaries propagate through the canyons quickly leaving little time for terrain-channeling.

4.5 Conclusions

This study quantifies the enhancement of microburst outflow boundary winds and turbulence within canyons using the WRF-LES simulation capability. Simulated microburst outflow boundaries propagate through short- (~1.5 to 4.5 km) and long-distance canyons (~3 to 6 km) where canyon walls have slopes of 10° and 30°. These canyon simulations are compared to microburst outflow boundary characteristics in flat terrain. Microbursts were placed close to the canyon, so that the maximum in outflow boundary wind speed occurs at the canyon entrance, and farther away to study the influence of topography on outflow boundaries with weaker wind speeds. The main findings from this analysis are:

- Short-distance microbursts produce stronger canyon-induced enhancements in horizontal wind, upward vertical velocity, *TKE*, and M_t in the canyons and along the canyon walls compared to long-distance microbursts, which are located ~2 km farther away. A reduction in the increase in horizontal winds of 0.3 to 3.3 m s^{-1}, upward vertical velocity of 0.1 to 3.1 m s^{-1}, *TKE* of 0.4 to 5.1 m^2 s^{-2}, and M_t of 4 to 32 % can be expected for every 2 km that the microburst is farther away from the canyons.
- For canyons located closer to the microburst, the increase in horizontal winds, vertical velocity, *TKE*, and M_t is generally stronger in the canyon and along the walls of the steeper 30° sloped canyons compared to the 10° sloped canyons. A reduction in the increase in horizontal winds of 0.2 to 3.4 m s^{-1}, upward vertical velocity of 0.8 to 4.6 m s^{-1}, *TKE* of 0.1 to 1.5 m^2 s^{-2}, and M_t of 6 to 35% can be expected for every 20° decrease in canyon slope when the microburst is close to the canyons. When the canyons are farther from the microburst, steeper slopes do not enhance the winds and turbulence in the canyon in either short- or long-distance canyons.

- For both short- and long-distance canyons, the maximum increase in horizontal wind is mostly observed near the canyon floors and towards the exit region of the canyons regardless of the proximity to the microburst. Conversely, the maximum increase in upward vertical velocity and *TKE* is mostly observed at higher elevations on the walls and along the canyon crests in both short- and long-distance canyons.

Results from this study provide an initial quantification of canyon-enhancement of microburst outflow winds and turbulence using idealized numerical simulations. A future study could expand upon these experiments and investigate the influence of other important parameters such as the magnitude and horizontal extent of the cold bubble perturbation, altering the background atmospheric stability and shear profile, changing the surface roughness length, or altering the height of the mountains. Additional analysis of these parameters could benefit fire weather forecasters and emergency responders who assess the potential dangers of outflow boundaries in and around ongoing canyon wildfires.

Acknowledgement: This research is supported through an award L17AC00227 ("JFSP Project 17-1-05-2 Evaluating thunderstorm outflow boundaries in WRF-Fire") from the Bureau of Land Management (BLM) as part of the Joint Fire Science Program under the subject opportunity FA-FON0017-0002. This work utilized the RMACC Summit supercomputer, which is supported by the National Science Foundation (awards ACI-1532235 and ACI-1532236), the University of Colorado Boulder, and Colorado State University. The Summit supercomputer is a joint effort of the University of Colorado Boulder and Colorado State University.

5 Conclusions

5.1 Summary of Key Findings

Our traditional understanding of GF characteristics have focused on well-organized thunderstorms that occur in orographically flat regions such as the U.S. Great Plains. This dissertation broadens the investigation of thunderstorm outflow boundaries by exploring the behavior and evolution of GFs that occur in areas of complex terrain. Thunderstorm GFs develop through the evaporation, melting, and sublimation of hydrometers within a thunderstorm downdraft. When the cold pool of air reaches the surface, it spreads horizontally away from the thunderstorm producing strong surface winds and turbulence. As such, GFs that develop near wildfires pose a significant threat to firefighters and emergency responders, especially in areas of complex terrain. Despite increased interest in understanding GF characteristics, few observations exist of GF effects on atmospheric properties (wind, temperature, humidity, and turbulence) in mountainous areas due to the sparsity of weather observations in these regions. Thus, the main objective of this dissertation was to increase our understanding of GFs in areas of complex terrain through a mix of observational and numerical analysis. The work in this dissertation adds to the understanding of terrain influence on propagating GFs in the following ways.

In Chapter 2, *in-situ* and remote sensing observations were combined to quantify the magnitude and rate change of atmospheric variables from 24 GF events in and near the complex terrain of the Colorado Front Range. Horizontal wind, turbulence (*TI and TKE)*, vertical velocity, temperature, and humidity were analyzed in the lowest 300 m AGL using a remote-sensing microwave radiometer, wind-profiling lidars, and *in situ* data from three meteorological towers. It was found that GFs that encountered higher variability in terrain slope were on

average slower (6.6 ± 3.3 m s^{-1}), compared to those that encountered less variability in terrain (10.1 ± 3.8 m s^{-1}) at the time they passed over the instruments. Additionally, it was found that the influence of the pre-frontal cross-front ambient wind component on propagation speed was negligible for these 24 cases. The magnitude change in temperature (0.2 to 3 °C), maximum vertical velocities (2 – 3.6 m s^{-1}), and maximum wind gusts (mean = 7.9 m s^{-1}) were generally weaker compared to studies of GFs initiating from organized, severe thunderstorms in flatter terrain. The average cold air depth was about 360 m, shallower compared to other studies, which may explain the weaker magnitude changes observed in this study. Vertical profiles reveal that these GF-induced atmospheric changes vary little with height in the lowest 300 m. Lastly, this was one of the first studies to evaluate the 3 D *TKE* associated with passing GFs. Short duration spikes in *TKE (* > 4 m^2 s^2) occur in 14 (58 %) of the 24 GF events, exceeding *TKE* values often associated with unstable boundary layer conditions.

In Chapter 3, the variability in propagation speed and atmospheric characteristics are quantified across 122 GFs that occurred in the complex terrain of NM and AZ during the 2010 to 2018 monsoonal seasons. Using *in-situ* ASOS station and radar observations, GFs that were pushed uphill and propagated atop the crest of the Mogollon Rim in AZ were compared to those that propagated down into or along the Rio Grande Valley in NM to assess how variability in terrain may influence GF characteristics. GFs that propagated downhill into and along the Rio Grande Valley in NM were associated with faster propagation speeds ($\overline{pspd}$ = 8.6 m s^{-1}), slightly larger decreases in temperature ($\Delta\bar{T}$ = -2.2°C), larger increases in horizontal wind speeds ($\Delta\overline{wsp}$ = 7.5 m s^{-1}) and changes in wind direction ($\Delta\overline{wdir}$ = 76.5°) compared to GFs that reached the crest of the Mogollon Rim in AZ ($\overline{pspd}$ = 5.2 m s^{-1}; $\Delta\bar{T}$ = -1.5°C; $\Delta\overline{wsp}$ = 3.5 m s^{-1}; $\Delta\overline{wdir}$ = 53.1°). These results are consistent with observational findings from previous work

which suggest that GFs that travel downslope (upslope) can accelerate (decelerate) and induce larger (smaller) increases in wind speed (Kishcha et al. 2016; Luchetti et al. 2020). GFs that propagated downhill into the Rio Grande Valley in NM behaved more in accordance with traditional density current theory compared to those that were pushed uphill and propagated atop the Mogollon Rim in AZ. Traditional density current theory suggests that the stronger the difference in the temperature between the boundary and the ambient air, the stronger the wind speeds behind the two air masses. In this study, the relationship between the magnitude decrease in temperature and magnitude increase in wind speed was stronger for GFs that propagated down into and along the Rio Grande Valley in NM (r = 0.57; R^2 = 0.33) compared to those atop the Mogollon Rim in AZ (r = 0.28, R^2 = 0.08). These findings provide observational evidence supporting the results of previous laboratory experiments which investigate the influence of upslope and downslope surfaces on density current characteristics.

In Chapter 4, canyon-enhancement of microburst outflow winds and turbulence was quantified using the WRF-LES numerical weather model. Simulated microburst outflow boundaries that propagated through short- (~1.5 to 4.5 km) and long-distance (~3 to 6 km) canyons with slopes of 10° and 30° were compared to microburst outflow boundaries over flat terrain (0°). The influence of microburst location (with respect to the topography) was also discussed. Short-distance microbursts produce stronger canyon-induced enhancements in horizontal wind, upward vertical velocity, *TKE*, and maximum topographic multipliers (M_t) in the canyons and along the canyon walls compared to long-distance microbursts, which are located ~2 km farther away. A reduction in the increase in horizontal winds of 0.3 to 3.3 m s^{-1}, upward vertical velocity of 0.1 to 3.1 m s^{-1}, *TKE* of 0.4 to 5.1 m^2 s^{-2}, and M_t of 4 to 32 % can be expected for every 2 km that the microburst is farther away from the canyons. For canyons

located closer to the microburst, the increase in horizontal winds, vertical velocity, *TKE*, and M_t is generally stronger in the canyon and along the walls of the steeper 30° sloped canyons compared to the 10° sloped canyons. A reduction in the increase in horizontal winds of 0.2 to 3.4 m s^{-1}, upward vertical velocity of 0.8 to 4.6 m s^{-1}, *TKE* of 0.1 to 1.5 m^2 s^{-2}, and M_t of 6 to 35% can be expected for every 20° decrease in canyon slope when the microburst is close to the canyons. Lastly, for both short- and long-distance canyons, the maximum increase in horizontal wind is mostly observed near the canyon floors and towards the exit region of the canyons regardless of the proximity to the microburst. Conversely, the maximum increase in upward vertical velocity and *TKE* is mostly observed at higher elevations on the walls and along the canyon crests in both short- and long-distance canyons.

The main objective of this work was to advance our understanding of thunderstorm GFs that occur in areas of complex terrain to help decision-makers to better understand how terrain can influence wind and turbulence generated by GFs. Advancements were made in understanding how GFs from less-organized mountain thunderstorms characteristically compare to those that develop from well-organized thunderstorms in flatter regions. While GF-induced atmospheric changes were weaker for GFs along the Colorado Front Range compared to GFs in flatter terrain regions, the changes in wind and turbulence were still strong enough to significantly alter fire behavior. Additionally, measurements of *TKE* in the Colorado Front Range GFs provide a quantitative analysis of the horizontal and vertical turbulence associated with mountain GFs. This is particularly useful for assessing the damage potential to wind energy structures, as well as useful knowledge for landing and take-off operations at airports located in mountain regions. Comparisons of GFs that propagate down into a major river valley in NM to those that are pushed uphill to a major ridgeline in AZ provides observational evidence of density current

behavior on sloped surfaces. This can aid short-term forecasting of GFs in and around wildfires that are either occurring along a ridgeline or within a valley, and provides the fire weather community with extensive statistical guidance of GF behavior in mountainous areas. Additionally, observations of GFs in these mountain regions (Colorado, Arizona, and New Mexico) can also benefit numerical models to help better incorporate the influence that terrain features can have on the strength and modification of GFs. The first analysis of simulated microburst outflow boundary interactions with canyons to the authors' knowledge were presented. This analysis demonstrated that the impact of canyons on winds and turbulence generated by microburst outflow boundaries is contingent on the proximity of the microburst to the terrain, the horizontal length of the canyon, as well as the degree of slope steepness along the canyon walls. Additionally, the strongest impact on microburst outflow winds and turbulence varied spatially within and along the canyon walls. This information can benefit forecasters and emergency responders when assessing the potential dangers of microburst outflow boundaries in and around ongoing canyon wildfires. Considering these general conclusions and overall contributions to the literature, there are a few recommendations for future work that could benefit and complement the work presented in this dissertation.

5.2 Recommendations for Future Work

Results from Chapter 2 indicated that GFs from less-organized thunderstorms over mountain terrain have weaker changes in atmospheric characteristics compared to studies of GFs from organized thunderstorms in flatter terrain. However, a future study that compares GFs from weak mountain thunderstorms to GFs from weak flat terrain thunderstorms may provide a better and more consistent comparison. Additionally, the change in atmospheric characteristics during GF passage results in Chapter 2 were confined to the lowest 300 m AGL. It is recommended

that a similar vertical profile analysis of mountain GF characteristics be extended to above 300 m AGL using dual-Doppler radar analysis or synchronized *in-situ* radiosonde launches before and after GF passage. This extended vertical resolution could provide better details of GF structure aloft in areas of mountainous terrain.

Chapter 3 results showed that GFs that propagate downhill into a major valley were generally faster, colder, and induced stronger increases in horizontal winds compared to GFs that were pushed uphill up to a major ridgeline. It is recommended that this analysis be expanded to other terrain regions where GFs propagate down into valleys or up and over ridgelines in order to corroborate these findings. It would also be interesting to assess and compare GFs that interact with other common terrain features such as plateaus or depressions. Furthermore, the terrain profile analysis in Chapter 3 utilized a somewhat limited, fixed location, Eulerian approach to link GF characteristics to the mean slope of the underlying terrain. A future study should utilize a Lagrangian modeling approach to follow and quantify changes in atmospheric characteristics along the leading edge of a GF at every uphill and downhill stretch over a terrain profile. This GF-following approach would likely provide a better understanding of whether or not upslope and downslope adiabatic processes influence propagating GFs.

In Chapter 4, idealized simulations of microburst flow over both short- and long-distance canyons showed that wind and turbulence from outflow boundaries are maximized when the canyons are close to the downdraft, and along steeper canyon walls. However, a future study should expand upon these experiments and investigate the influence of other parameters that may influence the strength of winds and turbulence from outflow boundaries within canyons. This may include testing the sensitivity of the magnitude and horizontal extent of the cold bubble perturbation that initializes the microburst, altering the background atmospheric stability and

shear profile, changing the surface roughness length and vegetation cover, or altering the height of the ridgelines. Additionally, incorporating a fire line at the entrance region of the canyons and assessing the fire response to microburst outflow boundaries for the same range of canyon slopes and proximity to the downdrafts is also a recommended future study.

References

Adams, D. K. and A. C. Comrie, 1997: The North American Monsoon. *Bull. Amer. Meteor. Soc.*, **78**, 2197–2214, https://doi.org/10.1175/1520-0477(1997)078<2197:TNAM>2.0.CO;2.

Aitken, M.L., R.M. Banta, Y.L. Pichugina, and J.K. Lundquist, 2014: Quantifying Wind Turbine Wake Characteristics from Scanning Remote Sensor Data. *J. Atmos. Oceanic Technol.*, **31**, 765–787, https://doi.org/10.1175/JTECH-D-13-00104.1.

Arritt, R. W., 1993: Effects of the large-scale flow on characteristic features of the sea breeze. *J. Appl. Meteor.*, **32**, 116–125, https://doi.org/10.1175/1520-0450(1993)032<0116:EOTLSF>2.0.CO;2.

Ashley, W.S., A.M. Haberlie, and J. Strohm, 2019: A Climatology of Quasi-Linear Convective Systems and Their Hazards in the United States. *Wea. Forecasting*, **34**, 1605–1631, https://doi.org/10.1175/WAF-D-19-0014.1

American Wind Energy Association Annual Wind Industry Report (AWEA), 2008: American Wind Energy Association, 2008. Annual Wind Industry Report – Year Ending 2008.

Benjamin, T. B., 1968: Gravity currents and related phenomena. *Journal of Fluid Mechanics*, **31**, 209-248. doi:https://doi.org/10.1017/S0022112068000133.

Bianco, L., K. Friedrich, J. Wilczak, D. Hazen, D. Wolfe, R. Delgado, S. Oncley, and J. K. Lundquist, 2017: Assessing the accuracy of microwave radiometers and radio acoustic sounding systems for wind energy applications. *Atmos. Meas. Tech.*, **10**, 1707-1721, doi:10.5194/amt-10-1707-2017.

Bidokhti, A. A., & Bani-Hashem, T. (2001). Structure of thunderstorm gust fronts with topographic effects. *Advances in Atmospheric Sciences*, **18**, 1161-1174.

Bingöl, F., J. Mann, and D. Foussekis, 2009: Conically scanning lidar error in complex terrain. *Meteor. Z.*, **18**, 189–195, doi:https://doi.org/10.1127/0941-2948/2009/0368.

Bodini, N., J. K. Lundquist, and R. K. Newsom, 2018: Estimation of turbulence dissipation rate and its variability from sonic anemometer and wind Doppler lidar during the XPIA field campaign, *Atmos. Meas. Tech.*, **11**, 4291–4308, https://doi.org/10.5194/amt-11-4291-2018.

Bosart, L.F., A. Seimon, K. D. LaPenta, and M. J. Dickinson, 2006: Supercell tornadogenesis over complex terrain: The Great Barrington, Massachusetts, tornado on 29 May 1995. *Wea. Forecasting*, **21**, 897–922, https://doi.org/10.1175/WAF957.1.

Bowen, B.M., 1996: Example of Reduced Turbulence during Thunderstorm Outflow. *J. Appl. Meteor.*, **35**, 1028–1032, https://doi.org/10.1175/1520-

0450(1996)035<1028:EORTDT>2.0.CO;2

Bryan, G.H., 2005: Spurious Convective Organization in Simulated Squall Lines Owing to Moist Absolutely Unstable Layers. *Mon. Wea. Rev.*, **133**, 1978–1997,https://doi.org/10.1175/MWR2952.1.

Bryan, G. H., and R. Rotunno, 2008: Gravity currents in a deep anelastic atmosphere. *J. Atmos. Sci.*, **65**, 536-556. Doi: https://doi.org/10.1175/2007JAS2443.1.

Bryan, G.H. and M.D. Parker, 2010: Observations of a Squall Line and Its Near Environment Using High-Frequency Rawinsonde Launches during VORTEX2. *Mon. Wea. Rev.*, **138**, 4076–4097, https://doi.org/10.1175/2010MWR3359.1.

Brown, H., 2002: Thirtymile Fire: fire behavior and management response. *Fire Management Today*, **62(3)**, 23–30. [Available at https://www.fs.usda.gov/sites/default/files/fire-management-today/62-3.pdf]

Bunkers, M.J., M.R. Hjelmfelt, and P.L. Smith, 2006: An Observational Examination of Long-Lived Supercells. Part I: Characteristics, Evolution, and Demise. *Wea. Forecasting*, **21**, 673–688, https://doi.org/10.1175/WAF949.1

Charba, J., 1974. Application of gravity current model to analysis of squall-line gust front. *Mon. Wea. Rev.*, **102**, 140-156.

Chay, M. T., F. Albermani, and R. Wilson, 2006: Numerical and analytical simulation of downburst wind loads. *Engineering Structures*, **28**, 240-254. https://doi.org/10.1016/j.engstruct.2005.07.007.

Clifton, A. and J.K. Lundquist, 2012: Data Clustering Reveals Climate Impacts on Local Wind Phenomena. *J. Appl. Meteor. Climatol.*, **51**, 1547–1557,https://doi.org/10.1175/JAMC-D-11-0227.1.

Clifton A., S. Schreck, G. Scott, N. Kelley, J. K. Lundquist, 2013: Turbine Inflow Characterization at the National Wind Technology Center. *ASME. J. Sol. Energy Eng,* **135**, 031017-031017-11. doi:10.1115/1.4024068.

Clifton, A., 2014: 135-m Meteorological Masts at the National Wind Technology Center. [Available at https://wind.nrel.gov/MetData/Publications/NWTC_135m_MetMasts.pdf]

Coen, J.L. and Riggan, P.J. 2011: A landscape-scale wildland fire study using coupled weather-wildland fire model and airborne remote sensing. In Wade, D.D.; Robinson, M.L. (eds) *Proc. of the 3rd Fire Behavior and Fuel Conference, Oct. 25-29,2010*, Spokane, Washington, International Association of Wildland Fire, Birmingham, Alabama, USA. 10 p.

Coen, J.L., M. Cameron, J. Michalakes, E.G. Patton, P.J. Riggan, and K.M. Yedinak, 2013: WRF-Fire: Coupled Weather–Wildland Fire Modeling with the Weather Research and Forecasting Model. *J. Appl. Meteor. Climatol.*, **52**, 16–38, https://doi.org/10.1175/JAMC-D-12-023.1.

Coen, J. L., and W. Schroeder, 2017: Coupled weather-fire modeling: from research to operational forecasting. *Fire Management Today*, **75**, 39-45.

Coen, J. L., E. N. Stavros, and J. A. Fites-Kaufman, 2018: Deconstructing the King megafire. *Ecological applications*, **28**, 1565-1580. https://doi.org/10.1002/eap.1752.

Cotton, W.R., R.L. George, P.J. Wetzel, and R.L. McAnelly, 1983: A Long-Lived Mesoscale Convective Complex. Part I: The Mountain–Generated Component. *Mon. Wea. Rev.*, **111**, 1893–1918, https://doi.org/10.1175/1520-0493(1983)111<1893:ALLMCC>2.0.CO;2

Cotton, W. R., Bryan, G., & Van den Heever, S. C., 2011: *Storm and cloud dynamics (Vol. 99)*. Academic press. 820 pp.

Courtney, M., R. Wagner, and P. Lindelow 2008: Testing and comparison of lidars for profile and turbulence measurements in wind energy. *Proc. 14th Int. Symp. for the Advancement of Boundary Layer Remote Sensing, Vol. 1, Risø DTU,* Denmark, IOP Conference Series: Earth and Environmental Science, 012021.

Dai, A., C. E. Ozdemir, M. I. Cantero, and S. Balachandar, 2012: Gravity currents from instantaneous sources down a slope. *Journal of Hydraulic Engineering*, **138**, 237-246, https://doi.org/10.1061/(ASCE)HY.1943-7900.0000500.

Dai, A., and Y.L. Huang, 2016: High-resolution simulations of non-Boussinesq downslope gravity currents in the acceleration phase. *Physics of Fluids*, **28**, 026602, https://doi.org/10.1063/1.4942239.

De Falco, M. C., L. Ottolenghi, and C. Adduce, 2020: Dynamics of gravity currents flowing up a slope and implications for entrainment. *Journal of Hydraulic Engineering*, **146**, 04020011, https://doi.org/10.1061/(ASCE)HY.1943-7900.0001709.

Draeger, R., 2016: Frog Fire Fatality. USDA Forest Service Learning Review Report. [Available at https://www.wildfirelessons.net/HigherLogic/System/DownloadDocumentFile.ashx?DocumentF ileKey=c197dde6-ced5-01a2-0b0d-2b735e4934ea&forceDialog=0].

Droegemeier, K.K. and R.B. Wilhelmson, 1987: Numerical Simulation of Thunderstorm Outflow Dynamics. Part I: Outflow Sensitivity Experiments and Turbulence Dynamics. *J. Atmos. Sci.*, **44**, 1180–1210, https://doi.org/10.1175/1520-0469(1987)044<1180:NSOTOD>2.0.CO;2.

Dupuy, J. L., J. Maréchal, D. Portier, and J. C. Valette, 2011: The effects of slope and fuel bed width on laboratory fire behaviour. *International Journal of Wildland Fire*, **20(2)**, 272-288. https://doi.org/10.1071/WF09075.

Engerer, N.A., D.J. Stensrud, and M.C. Coniglio, 2008: Surface Characteristics of Observed Cold Pools. *Mon. Wea. Rev.,* **136**, 4839–4849,https://doi.org/10.1175/2008MWR2528.1.

Esperanza Investigation Team, 2006: Esperanza Fire accident investigation factual report, Riverside County, California. [Available at http://www.fire.ca.gov/fire_ protection/downloads/esperanza_00_complete_final_ draft_05_01_2007.pdf]

ESRI, 2011. ArcGIS Desktop: Release 10. Environmental Systems Research Institute.

Federal Aviation Administration, 1988: Pilot windshear guide. AC 00-54, 1-64. Washington (DC): U.S. Department of Transportation. [Available at https://www.faa.gov/documentLibrary/media/Advisory_Circular/AC00-54.pdf]

Federal Aviation Administration, 2008: Thunderstorms- don't flirt…skirt 'em. FAA-P-8740-12, 1–6. Washington (DC): U.S. Department of Transportation. [Available at https://www.faasafety.gov/files/gslac/library/documents/2011/Aug/56397/FAA%20P-8740-12%20Thunderstorms[hi-res]%20branded.pdf]

Federal Aviation Administration, 2013: Thunderstorms. AC 00-24C. Oklahoma City (OK): U.S. Department of Transportation Federal Aviation Administration. [Available at https://www.faa.gov/documentlibrary/media/advisory_circular/ac%2000-24c.pdf]

Friedrich, K., D.E. Kingsmill, and C.R. Young, 2005: Misocyclone Characteristics along Florida Gust Fronts during CaPE. *Mon. Wea. Rev*., **133**, 3345–3367,https://doi.org/10.1175/MWR3040.1.

Friedrich, K., J. K. Lundquist, M. Aitken, E. A. Kalina, and R. F. Marshall, 2012: Stability and turbulence in the atmospheric boundary layer: A comparison of remote sensing and tower observations. *Geophysical Research Letters*, **39**. https://doi.org/10.1029/2011GL050413.

Fujita, T.T., 1981: Tornadoes and Downbursts in the Context of Generalized Planetary Scales. *J. Atmos. Sci.*, **38**, 1511–1534, https://doi.org/10.1175/1520-0469(1981)038<1511:TADITC>2.0.CO;2.

Fujita, T. T., and R. M. Wakimoto, 1983: Microbursts in JAWS depicted by Doppler radars, PAM, and aerial photographs. *Preprints, 21st Conference on Radar Meteorology,* Edmonton, Canada, American Meteorological Society, Boston, 638-645.

Fujita, T. T., 1985: The Downburst - Microburst and Macroburst. Report of Projects NIMROD and JAWS. SMRP, University of Chicago, Chicago, 122 pp.

Gilliam, R. C., S. Raman, and D.D.S. Niyogi, 2004: Observational and numerical study on the influence of large-scale flow direction and coastline shape on sea-breeze evolution. *Boundary-Layer Meteorology*, **11,** 275-300, https://doi.org/10.1023/B:BOUN.0000016494.99539.5a.

Goens, D. W., and P. L. Andrews, 1998: Weather and fire behavior factors related to the 1990 Dude Fire near Payson, AZ. *Second Conf. on Fire and Forest Meteorology,* Phoenix, AZ, Amer. Meteor. Soc., 153–158.

Goff, R., 1976: Vertical Structure of Thunderstorm Outflows. *Mon. Wea. Rev*., **104**, 1429–1440, https://doi.org/10.1175/1520-0493(1976)104<1429:VSOTO>2.0.CO;2.

Grant, L. D., and S. C. van den Heever, 2016: Cold pool dissipation. *J. Geophys. Res. Atmos.*, **121**, 1138–1155, doi:10.1002/2015JD023813.

Hadi, F. A., S. T. Nassir, and R. A. Abdulwahab, 2015: Turbulence Intensity Calculation for Al-Shehabi Site in Iraq. *International Journal of Advanced Research in Electrical, Electronics and Instrumentation Engineering*, **4**, 7619 - 7627.

Haines, D. A., 1988: Downbursts and wildland fires: a dangerous combination. *Fire Management Today*, **49**, 8–10.

Hardy, K. and L. K. Comfort, 2015: Dynamic decision processes in complex, high-risk operations: The Yarnell Hill Fire, June 30, 2013. *Safety science*, **71**, 39-47.

Hanley, D. E., P. Cunningham, and S. L. Goodrick, 2013: Interaction between a Wildfire and the Sea-Breeze Front. Remote Sensing and Modeling Applications to Wildland Fires, 81-98. https://doi.org/10.1007/978-3-642-32530-4_7.

Hawley, L. F., 1926: Theoretical considerations regarding factors which influence forest fires. *Journal of Forestry*, **24(7)**, 756-763. https://doi.org/10.1093/jof/24.7.756.

He, Z., L. Zhao, T. Lin, P. Hu, Y. lv, H. C. Ho, and Y. T. Lin, 2017: Hydrodynamics of gravity currents down a ramp in linearly stratified environments. *Journal of Hydraulic Engineering*, **143**, 04016085, https://doi.org/10.1061/(ASCE)HY.1943-7900.0001242.

Hjelmfelt, M.R., 1988: Structure and Life Cycle of Microburst Outflows Observed in Colorado. *J. Appl. Meteor.*, **27**, 900–927, https://doi.org/10.1175/1520-0450(1988)027<0900:SALCOM>2.0.CO;2

Houze Jr., R. A., 1993: *Cloud Dynamics*. Academic Press, 570

Jager, D., and A. Andreas, 1996: NREL National Wind Technology Center (NWTC): M2 Tower: Boulder, Colorado (Data). NREL Report No. DA-5500-56489. http://dx.doi.org/10.5439/1052222.

Jiménez, P., D. Muñoz-Esparza, and B. Kosović, 2018: A High Resolution Coupled Fire–Atmosphere Forecasting System to Minimize the Impacts of Wildland Fires: Applications to the Chimney Tops II Wildland Event. *Atmosphere*, **9**, 197.

Jorgensen, D.P., Z. Pu, P.O. Persson, and W. Tao, 2003: Variations Associated with Cores and Gaps of a Pacific Narrow Cold Frontal Rainband. *Mon. Wea. Rev*., **131**, 2705–2729, https://doi.org/10.1175/1520-0493(2003)131<2705:VAWCAG>2.0.CO;2

Johnson, W., and N. Kelley, 2000: Design Specifications for the Development of the Initial Validation Software (Version 3.0) for Processing of NWTC 80-Meter Meteorological Tower Data. 92 pp.; NREL Report No. TP-500-27104.

Johnson, R.H., R.S. Schumacher, J.H. Ruppert, D.T. Lindsey, J.E. Ruthford, and L. Kriederman, 2014: The Role of Convective Outflow in the Waldo Canyon Fire. *Mon. Wea. Rev.*, **142**, 3061–3080, https://doi.org/10.1175/MWR-D-13-00361.1.

Joint Fire Science Program, 2017: Validating Mesoscale, Atmospheric Boundary Prediction Models and Tools. [Available online: https://www.firescience.gov/AFPs/17-1-05/17-1-05_FON_Announcement.pdf].

Kaimal, J.C. and J.E. Gaynor, 1983: The Boulder Atmospheric Observatory. *J. Climate Appl. Meteor.*, **22**, 863–880, https://doi.org/10.1175/1520-0450(1983)022<0863:TBAO>2.0.CO;2/

Karels, J., and M. Dudley, 2013: Yarnell Hill Fire Serious Accident Investigation Report. Arizona State Forestry Division Rep., 116 pp., https://docs.google.com/file/d/0B36DIycSgbzWSUtjNkl1Z2ROT0k/edit.

Kern, J., W. Jones, J. Murrian, and J. DiMaggio, 2004: Review of Burnover Incident at St Sebastian River Preserve State Park, Indian River County, Florida, 24 February 2004. [Available at http://www.wildfirelessons.net/HigherLogic/System/DownloadDocumentFile.ashx?DocumentFileKey=83ebf8a1-1d12-001c-32b5-d279c795fa6b&forceDialog=1]

Keighton, S., J. Jackson, J. Guyer, and Peters, J., 2007: A preliminary analysis of severe quasilinear mesoscale convective systems crossing the Appalachians. Paper presented at the 22nd Conf. on Weather Analysis and Forecasting/18th Cof. on Numerical Weather Prediction. Retrieved from http://ams.confex.com/ams/pdfpapers/123614.pdf

Kishcha, P., and Coauthors, 2016: Modelling of a strong dust event in the complex terrain of the Dead Sea valley during the passage of a gust front. *Tellus B: Chemical and Physical Meteorology*, **68**, 29751. https://doi.org/10.3402/tellusb.v68.29751.

Koch, S.E. and C.A. Ray, 1997: Mesoanalysis of Summertime Convergence Zones in Central and Eastern North Carolina. *Wea. Forecasting*, **12**, 56–77,https://doi.org/10.1175/1520-0434(1997)012<0056:MOSCZI>2.0.CO;2.

Kumer, V. M., J. Reuder, M. Dorninger, R. Zauner, and V. Grubišić, 2016: Turbulent kinetic energy estimates from profiling wind LiDAR measurements and their potential for wind energy applications. *Renewable energy*, **99**, 898-910. https://doi.org/10.1016/j.renene.2016.07.014.

Kwon, D. K., and A. Kareem, 2009: Gust-front factor: New framework for wind load effects on structures. *Journal of structural engineering*, **135**, 717-732. https://doi.org/10.1061/(ASCE)0733-9445(2009)135:6(717).

Kwon, D. K., A. Kareem, and K. Butler, 2012: Gust-front loading effects on wind turbine tower systems. *Journal of Wind Engineering and Industrial Aerodynamics*, **104**, 109-115. https://doi.org/10.1016/j.jweia.2012.03.030.

Kwon, D. K., and A. Kareem, 2013: Generalized gust-front factor: A computational framework for wind load effects. *Engineering Structures*, **48**, 635-644. https://doi.org/10.1016/j.engstruct.2012.12.024.

LaPenta, K.D., L.F. Bosart, T.J. Galarneau, and M.J. Dickinson, 2005: A Multiscale examination of the 31 May 1998 Mechanicville, New York, tornado. *Wea. Forecasting*, **20**, 494–516, https://doi.org/10.1175/WAF875.1.

Letchford, C., and Illidge, 1999: Turbulence and topographic effects in simulated thunderstorm downdrafts by wind tunnel jet. *Proc,. 10th ICWE*, Copenhagen, 1999.

Letchford, C. W., C. Mans, and M. T. Chay, 2002: Thunderstorms-their importance in Wind Engineering (A case for the next generation wind tunnel). *Journal of Wind Engineering and Industrial Aerodynamics,* **90***,* 1415-1433. https://doi.org/10.1016/S0167-6105(02)00262-3.

Liu, N., H. Chen, X. Xie, L. Zhang, B. Yao, J. Zhu, and Y. Shan, 2014: Effect of slope on spread of a linear flame front over a pine needle fuel bed: experiments and modelling. *International Journal of Wildland Fire***, 23(8)**, 1087-1096. https://doi.org/10.1071/WF12189.

Lombardi, V., C. Adduce, G. Sciortino, and M. La Rocca, 2015: Gravity currents flowing upslope: Laboratory experiments and shallow-water simulations. *Physics of Fluids*, **27**, 016602. https://doi.org/10.1063/1.4905305.

Lombardo, F. T., D. A. Smith, J. L. Schroeder, and K. C. Mehta, 2014: Thunderstorm characteristics of importance to wind engineering. *Journal of Wind Engineering and Industrial Aerodynamics*, **125**, 121-132. https://doi.org/10.1016/j.jweia.2013.12.004.

Lombardo, F. T., M.S. Mason, and A. Z. de Alba, 2018: Investigation of a downburst loading event on a full-scale low-rise building. *Journal of Wind Engineering and Industrial Aerodynamics*, **182**, 272-285. https://doi.org/10.1016/j.jweia.2018.09.020.

Lompar, M., M. Ćurić, and D. Romanic, 2018: Implementation of a gust front head collapse scheme in the WRF numerical model. *Atmospheric Research*, **203**, 231-245. doi: 10.1016/j.atmosres.2017.12.018.

Lu, N. Y., P. Hawbecker, S. Basu, and L. Manuel, 2019: On Wind Turbine Loads During Thunderstorm Downbursts in Contrasting Atmospheric Stability Regimes. *Energies*, **12**, 2773. https://doi.org/10.3390/en12142773.

Luchetti, N.T., K. Friedrich, C.E. Rodell, and J.K. Lundquist, 2020: Characterizing thunderstorm gust fronts near complex terrain. *Mon. Wea. Rev.*, **0**, https://doi.org/10.1175/MWR-D-19-0316.1.

Luchetti, N. T., K. Friedrich, and C. E. Rodell, Evaluating Thunderstorm Gust Fronts in New Mexico and Arizona. *Mon. Wea. Rev.*, doi: https://doi.org/10.1175/MWR-D-20-0204.1.

Lundquist, J. K., M. J. Churchfield, S. Lee, and A. Clifton, 2015: Quantifying error of lidar and sodar Doppler beam swinging measurements of wind turbine wakes using computational fluid dynamics. *Atmos. Meas. Tech.*, **8**, 907–920, doi:https://doi.org/10.5194/amt-8-907-2015.

Lundquist, J.K., and Coauthors, 2017: Assessing State-of-the-Art Capabilities for Probing the Atmospheric Boundary Layer: The XPIA Field Campaign. *Bull. Amer. Meteor. Soc.*, **98**, 289–314, https://doi.org/10.1175/BAMS-D-15-00151.1.

Mahoney, W.P., 1988: Gust Front Characteristics and the Kinematics Associated with Interacting Thunderstorm Outflows. *Mon. Wea. Rev*., **116**, 1474–1492,https://doi.org/10.1175/1520-0493(1988)116<1474:GFCATK>2.0.CO;2.

Mason, M. S., G. S. Wood, and D. F. Fletcher, 2007: Impinging jet simulation of stationary downburst flow over topography. *Wind and Structures*, **10(5)**, 437-462. https://doi.org/10.12989/was.2007.10.5.437

Mason, M. S., G. S. Wood, and D. F. Fletcher, 2010: Numerical investigation of the influence of topography on simulated downburst wind fields. *J. Wind Eng. Ind. Aerodyn.*, **98**, 21–33, https://doi.org/10.1016/j.jweia.2009.08.011.

Manwell, J. F., J. G. McGowan, and A. L. Rogers, 2002: Wind Energy Explained. *Aerodynamics of Wind Turbines*. West-Sussex, England, John Wiley and Sons, Ltd.

Marleau, L. J., M. R. Flynn, and B. R. Sutherland, 2014: Gravity currents propagating up a slope. *Physics of Fluids*, **26**, 046605, https://doi.org/10.1063/1.4872222.

Martner, B.E., 1997: Vertical Velocities in a Thunderstorm Gust Front and Outflow. *J. Appl. Meteor.*, **36**, 615–622, https://doi.org/10.1175/1520-0450(1997)036<0615:VVIATG>2.0.CO;2.

McAnelly, R.L. and W.R. Cotton, 1986: Meso-β-scale Characteristics of an Episode of Meso-α-scale Convective Complexes. *Mon. Wea. Rev.*, **114**, 1740–1770, https://doi.org/10.1175/1520-0493(1986)114<1740:MSCOAE>2.0.CO;2

McCaffrey, K., P. T. Quelet, A. Choukulkar, J. M. Wilczak, D. E. Wolfe, S. P. Oncley, W. A., Brewer, M. Debnath, R. Ashton, G. V. Inugo, and Lundquist, J. K., 2017: Identification of tower-wake distortions using sonic anemometer and lidar measurements. *Atmos. Meas. Tech.*, **10**, 393-407, 10.5194/amt-10-393-2017.

Mirocha, J. D., J. K. Lundquist, and B. Kosović, 2010: Implementation of a Nonlinear Subfilter Turbulence Stress Model for Large-Eddy Simulation in the Advanced Research WRF Model. *Mon. Wea. Rev.*, **138**, 4212–4228, https://doi.org/10.1175/2010MWR3286.1.

Mirocha, J., G. Kirkil, E. Bou-Zeid, F. K. Chow, and B. Kosović, 2013: Transition and Equilibration of Neutral Atmospheric Boundary Layer Flow in One-Way Nested Large-Eddy Simulations Using the Weather Research and Forecasting Model. *Mon. Wea. Rev.*, **141**, 918–940, https://doi.org/10.1175/MWR-D-11-00263.1.

Moeng, C., J. Dudhia, J. Klemp, and P. Sullivan, 2007: Examining Two-Way Grid Nesting for Large Eddy Simulation of the PBL Using the WRF Model. *Mon. Wea. Rev.*, **135**, 2295–2311, https://doi.org/10.1175/MWR3406.1.

Moller, A.R., C.A. Doswell, M.P. Foster, and G.R. Woodall, 1994: The Operational Recognition of Supercell Thunderstorm Environments and Storm Structures. *Wea. Forecasting*, **9**, 327–347, https://doi.org/10.1175/1520-0434(1994)009<0327:TOROST>2.0.CO;2.

Monastersky, R., 1987: Mastering the microburst. *Science News*, 185-187.

Muñoz-Esparza, D., B. Kosović, P. A. Jiménez, and J. L. Coen, 2018: An Accurate Fire-Spread Algorithm in the Weather Research and Forecasting Model Using the Level-Set Method. Journal of Advances in Modeling Earth Systems, **10**, 908-926. https://doi.org/10.1002/2017MS001108.

Nadolski, V. 1998: Automated Surface Observing System (ASOS) user's guide. National Oceanic and Atmospheric Administration, Department of Defense, Federal Aviation Administration, United States Navy. [Available at https://www.weather.gov/media/asos/aum-toc.pdf]

Nguyen, H. H., L. Manuel, and P.S. Veers, 2011: Wind turbine loads during simulated thunderstorm microbursts. *Journal of Renewable and Sustainable Energy*, **3**, 053104. https://doi.org/10.1063/1.3646764.

Nunalee, C. G., B. Kosović, and P. E. Bieringer, 2014: Eulerian dispersion modeling with WRF-LES of plume impingement in neutrally and stably stratified turbulent boundary layers. *Atmospheric Environment*, **99**, 571-581. https://doi.org/10.1016/j.atmosenv.2014.09.070.

NWS, 2008: Cup & vane wind data processing within ASOS, 2 pp., [Available online at https://www.weather.gov/media/asos/ASOS%20Implementation/IFWS_BelfordWS_comparison.pdf]

O' Connor, A., and D. Kearney, 2019): Low Level Turbulence Detection For Airports. *International Journal of Aviation, Aeronautics, and Aerospace*, **6**, https://doi.org/10.15394/ijaaa.2019.1302.

Paez, G., M. Strojnik, and M. K. Scholl, 2015: Analysis of propagation of complex fire: case of the Yarnell Hill Fire 1. *Proc. Volume 9608, Infrared Remote Sensing and Instrumentation XXIII; 96081L*, San Diego, CA, https://doi.org/10.1117/12.2191725.

Parker, M.D. and R.H. Johnson, 2000: Organizational Modes of Midlatitude Mesoscale Convective Systems. *Mon. Wea. Rev.*, **128**, 3413–3436, https://doi.org/10.1175/1520-0493(2001)129<3413:OMOMMC>2.0.CO;2

Parker, M.D. and D.A. Ahijevych, 2007: Convective Episodes in the East-Central United States. *Mon. Wea. Rev.*, **135**, 3707–3727, https://doi.org/10.1175/2007MWR2098.1

Paez, G., M. Strojnik, and M. K. Scholl, 2015: Analysis of propagation of complex fire: case of the Yarnell Hill Fire 1. *Proc. Volume 9608, Infrared Remote Sensing and Instrumentation XXIII; 96081L*, San Diego, CA, https://doi.org/10.1117/12.2191725.

Provod, M., J.H. Marsham, D.J. Parker, and C.E. Birch, 2016: A Characterization of Cold Pools in the West African Sahel. *Mon. Wea. Rev.*, **144**, 1923–1934,https://doi.org/10.1175/MWR-D-15-0023.1.

Potter, B. E., and J. R. Hernandez, J. R., 2017: Downdraft outflows: climatological potential to influence fire behaviour. *International Journal of Wildland Fire*, **26(8)**, 685-692. https://doi.org/10.1071/WF17035.

Rauber, R. M., and S. L. Nesbitt, 2018: *Radar Meteorology: A First Course*. John Wiley & Sons. pp. 488.

Rhodes, M. E., and J. K. Lundquist, 2013: The effect of wind-turbine wakes on summertime US Midwest atmospheric wind profiles as observed with ground-based Doppler lidar. *Bound.-Layer Meteor.*, **149**, 85–103, doi:https://doi.org/10.1007/s10546-013-9834-x.

Rosenkranz, P. W., 1998: Water vapor microwave continuum absorption: A comparison of measurements and models, *Radio Science*, **33**, 919-928. https://doi.org/10.1029/98RS01182.

Rothermel, R. C., 1993: Mann Gulch fire: A race that couldn't be won. Gen. Tech. Rep. INT-299. Ogden, UT: US Department of Agriculture, Forest Service, Intermountain Research Station. 10 pp., 299.

Rotunno, R., J.B. Klemp, and M.L. Weisman, 1988: A Theory for Strong, Long-Lived Squall Lines. *J. Atmos. Sci*., **45**, 463–485, https://doi.org/10.1175/1520-0469(1988)045<0463:ATFSLL>2.0.CO;2

Roux, F., 1988: The West African Squall Line Observed on 23 June 1981 during COPT 81: Kinematics and Thermodynamics of the Convective Region. *J. Atmos. Sci.*, **45**, 406–426, https://doi.org/10.1175/1520-0469(1988)045<0406:TWASLO>2.0.CO;2

Sasaki, Y.K. and T. L. Baxter, 1986: The gust front. *Thunderstorm Morphology and Dynamics*, pp.187- 196.

Sathe, A., J. Mann, J. Gottschall, and M. S. Courtney 2011: Can wind lidars measure turbulence? *J. Atmos. Oceanic Technol.*, **28**, 853–868. doi: 10.1175/JTECH-D-10-05004.1.

Schmidli, J., 2013: Daytime Heat Transfer Processes over Mountainous Terrain. *J. Atmos. Sci.*, **70**, 4041–4066, https://doi.org/10.1175/JAS-D-13-083.1.

Schneider, D. G. 2009: The impact of terrain on three cases of tornadogenesis in the Great Tennessee Valley. *Electronic Journal of Operational Meteorology*, EJ11.

Schumacher, R.S. and R.H. Johnson, 2006: Characteristics of U.S. Extreme Rain Events during 1999–2003. *Wea. Forecasting*, **21**, 69–85, https://doi.org/10.1175/WAF900.1.

Sharples, J. J., 2008: Review of formal methodologies for wind–slope correction of wildfire rate of spread. *International Journal of Wildland Fire*, **17(2)**, 179-193. https://doi.org/10.1071/WF06156.

Sharples, J., A. M. Gill, J. W. Dold, 2010: The trench effect and eruptive wildfires: lessons from the King's Cross Underground disaster. *Proceedings of Australian Fire and Emergency Service Authorities Council 2010 Conference*, Darwin, Australia. [Available at http://www.maths. manchester.ac.uk/~jwd/articles/10-TEaEW.pdf.]

Sharples J. J., R. H. D. McRae, C. Simpson, P. Fox-Hughes, and C. Clements, 2017: Terrain-controlled airflows. *Fire Management Today*, **75**, 20-24.

Shipley, S.T., A. Peterlin, and S. Cantrell, 2009: Radar visualization and occultation in 4-dimensions using Google Earth. *AMS 25th IIPS*, Phoenix, AZ, 15 Jan 09. [Data Accessed at http://wxanalyst.com/radar/]

Simpson, J. E. (1969). A comparison between laboratory and atmospheric density currents. *Quarterly Journal of the Royal Meteorological Society*, **95**, 758-765. https://doi.org/10.1002/qj.49709540609.

Simpson, J.E. and Britter, R.E. (1980), A laboratory model of an atmospheric mesofront. *Quarterly Journal of the Royal Meteorological Society*, **106**, 485-500. doi:10.1002/qj.49710644907

Smith, B.T., R.L. Thompson, J.S. Grams, C. Broyles, and H.E. Brooks, 2012: Convective Modes for Significant Severe Thunderstorms in the Contiguous United States. Part I: Storm Classification and Climatology. *Wea. Forecasting,* **27**, 1114–1135, https://doi.org/10.1175/WAF-D-11-00115.1

Solari, G., 2014: Emerging issues and new frameworks for wind loading on structures in mixed climates. *Wind and Structures*, **19**, 295-320. https://doi.org/10.12989/was.2014.19.3.295.

Solari, G., M. Burlando, P. De Gaetano, and M. P. Repetto, 2015: Characteristics of thunderstorms relevant to the wind loading of structures. *Wind and Structures*, **20**, 763-791. https://doi.org/10.12989/was.2015.20.6.763.

Solheim, F., J. Godwin, and R. Ware, 1998a: Passive ground-based remote sensing of atmospheric temperature, water vapor, and cloud liquid water profiles by a frequency synthesized microwave radiometer, *Meteorologische Zeitschrift*, **7**, 370-376. 10.1127/metz/7/1998/370.

Solheim, F., J. Godwin, E.R. Westwater, Y. Han, S. J. Keihm, K. Marsh, R. Ware, 1998b: Radiometric profiling of temperature, water vapor and cloud liquid water using various inversion methods. *Radio Science*, **33**, 393-404. https://doi.org/10.1029/97RS03656.

Sullivan, A. L., 2009: Wildland surface fire spread modelling, 1990–2007. 3: Simulation and mathematical analogue models. *International Journal of Wildland Fire*, **18(4)**, 387-403. https://doi.org/10.1071/WF06144.

Sullivan, A. L., J. J. Sharples, S. Matthews, and M. P. Plucinski, 2014: A downslope fire spread correction factor based on landscape-scale fire behaviour. *Environmental Modelling & software,* **62**, 153-163. https://doi.org/10.1016/j.envsoft.2014.08.024.

Sull, R. B. 1988: *An Introduction to Boundary Layer Meteorology*. Kluwer Academic Publishers, Dordrecht.

Surveys and Investigation Staff, 1981: A report to the committee on appropriations US House of Representatives on wildfire on Merritt Island. December 1981. [Available at https://www.wildfirelessons.net/HigherLogic/System/DownloadDocumentFile.ashx?DocumentFileKey=de70dc82-1760-487f-b1d4-05a8d11293cc& forceDialog=0].

TC88-MT, I. E. C. 2005: Iec 61400-3: Wind turbines–part 1: Design requirements. International Electrotechnical Commission, Geneva, 64.

Tucker, D.F. and N.A. Crook, 1999: The Generation of a Mesoscale Convective System from Mountain Convection. *Mon. Wea. Rev.*, **127**, 1259–1273, https://doi.org/10.1175/1520-0493(1999)127<1259:TGOAMC>2.0.CO;2.

USDI, 1976: Accident Report - Battlement Creek fire fatalities and injury, July 17, 1976. United States Department of Interior, Unpublished Report on file at National Interagency Fire Center, Boise, ID, 125 p.

USDI/USDA, 1994: South Canyon Fire Investigation Report, Report of the South Canyon fire accident investigation team. Report 573-183, US Government Printing Office, Region 8, Washington DC. 234 p.

Viegas, D.X. 2005. A mathematical model for forest fire blow-up. *Combustion Science and Technology,* **177**, 1–25. https://doi.org/10.1080/00102200590883624.

Viegas, D.X., and A. Simeoni, 2010: Eruptive behaviour of forest fires. *Fire Technology*. **47(24)**, 303. https://doi.org/10.1007/s10694-010-0193-6.

Wakimoto, R. M. (1982). The life cycle of thunderstorm gust fronts as viewed with Doppler radar and rawinsonde data. *Mon. Wea. Rev.*, **110**, 1060-1082. https://doi.org/10.1175/1520-0493(1982)110<1060:TLCOTG>2.0.CO;2.

Wakimoto, R.M., C.J. Kessinger, and D.E. Kingsmill, 1994: Kinematic, thermodynamic, and visual structure of low-reflectivity microbursts. *Mon. Wea. Rev.*, **122**, 72–92, https://doi.org/10.1175/1520-0493(1994)122<0072:KTAVSO>2.0.CO;2.

Wilbanks, M.C., S.E. Yuter, S.P. de Szoeke, W.A. Brewer, M.A. Miller, A.M. Hall, and C.D. Burleyson, 2015: Near-Surface Density Currents Observed in the Southeast Pacific Stratocumulus-Topped Marine Boundary Layer. *Mon. Wea. Rev*., **143**, 3532–3555, https://doi.org/10.1175/MWR-D-14-00359.1.

Wilson, J. W., R. D. Roberts, C. Kessinger, and J. McCarthy, 1984: Microburst Wind Structure and Evaluation of Doppler Radar for Airport Wind Shear Detection. *J. Climate Appl. Meteor.*, **23**, 898–915, https://doi.org/10.1175/1520-0450(1984)023<0898:MWSAEO>2.0.CO;2.

Wilson, J.W. and W.E. Schreiber, 1986: Initiation of Convective Storms at Radar-Observed Boundary-Layer Convergence Lines. *Mon. Wea. Rev.,* **114**, 2516–2536,https://doi.org/10.1175/1520-0493(1986)114<2516:IOCSAR>2.0.CO;2.

Weisman, M. L., and J. B. Klemp, 1986: Characteristics of isolated convective storms. *Mesoscale meteorology and forecasting* (pp. 331-358). American Meteorological Society, Boston, MA.

Wolfe, D.E. and R.J. Lataitis, 2018: Boulder Atmospheric Observatory: 1977–2016: The End of an Era and Lessons Learned. *Bull. Amer. Meteor. Soc.*, **99**, 1345–1358,https://doi.org/10.1175/BAMS-D-17-0054.1.

Wood, G. S., K. C. Kwok, N. A. Motteram, and D. F. Fletcher, 2001: Physical and numerical modelling of thunderstorm downbursts. *Journal of Wind Engineering and Industrial Aerodynamics*, **89(6)**, 535-552. https://doi.org/10.1016/S0167-6105(00)00090-8.

Zhang, S., G. Solari, P. De Gaetano, M. Burlando, and M. P. Repetto, 2018: A refined analysis of thunderstorm outflow characteristics relevant to the wind loading of structures. *Probabilistic Engineering Mechanics*, **54**, 9-24. https://doi.org/10.1016/j.probengmech.2017.06.003